A NEAR-FIELD STUDY OF A SHALLOW MIXING LAYER BETWEEN COFLOWING STREAMS USING 3D-PTV

Claudio S. M. Consuegra Martínez

Department of Civil Engineering and Applied Mechanics

McGill University

Montreal, Quebec, Canada

November 2017

A thesis submitted to McGill University in partial fulfillment of the requirements for the degree of Master of Engineering

To my family

ABSTRACT

Shallow mixing layers have been the subject of many experimental studies, yet further understanding of the hydrodynamics of shallow flows is important to better predict their effect on the dispersion of pollutants/nutrients, sediment transport, and erosion processes. Understanding the hydrodynamics and the characteristics of shallow flows requires a fully three-dimensional (3D) observation of the flow and its turbulent structures. This thesis is a first attempt to study shallow mixing layers in the near-field of coflowing streams using a Lagrangian reference frame by applying 3D Particle Tracking Velocimetry (3D-PTV).

The present study investigates a simplified laboratory model of a river confluence modelled by parallel coflowing streams with different velocities (U_1 = 0.45 m/s, U_2 = 0.31 m/s) between which a shallow mixing layer develops. A new shallow recirculating glass flume, with dimensions of 9 m x 1.5 m x 0.25 m, (glass walls and bed) was set up for experiments for one turbulent hydraulic condition (mean Re = 24,700), having a water depth of 6.5 cm and a bed slope of zero. 3D-PTV measurements were made from the end of a splitter plate to a distance of 30 cm in the downstream direction using three high speed (600 Hz) and high-resolution (2016x2016 pixels) CCD cameras positioned to record images from below the glass flume bed. Information on the flow field was extracted from the image sequences using OpenPTV. The flow was seeded with rice bran wax microspheres (Florabeads RBW) with a specific gravity ~ 1 at 25°C and natural color, illuminated with halogen lamps. The 3D-PTV system was calibrated using a solid 3D calibration object. The data from 3D-PTV was post-processed to obtain the velocity flow field, which was in turn analyzed to obtain velocity time-series and shallow mixing layer transverse profiles for mean streamwise velocity and turbulent intensity, as well as instantaneous velocity information at different downstream positions.

A shallow mixing layer formed from coflowing streams can be divided into two regions in the downstream direction, a near-field zone in which the flow defined by the initial geometry evolves into a mixing layer and a self-similar region in which the mixing layer has developed its characteristic properties. In this first stage of investigation, the first 30 cm of the near-field were studied. In this region, the following flow characteristics were observed. Boundary layers, developing along the splitter plate dividing the parallel channels, result in a wake or velocity deficit at the streams confluence (at the end of the splitter plate). This velocity deficit decreases in

magnitude in the downstream distance but has not fully decayed by x=30 cm. The wake has a high turbulent intensity, as it is a shear layer forming due to the velocity gradient between the free streams and the velocity deficit, which decreases as the velocity deficit decreases in magnitude with downstream distance. The wake formed by the splitter plate is reducing, which limits establishment and growth of the mixing layer, causing the width of the shear layer to remain constant over the measurement distance and shifts towards the slower moving stream due to transverse momentum transfer. Lastly, the development of a secondary circulation is possibly appearing by the end of the measurement distance, as in instantaneous flow sections, transverse flow towards the slow stream appears at the surface and towards the fast stream at the bed.

RÉSUMÉ

Une compréhension approfondie du mélange turbulent en eaux peu profondes est pertinente pour mieux prédire la dispersion des contaminants/nutriments, le transport des sédiments et les processus d'érosion, même si le sujet a été étudié dans différentes recherches. Comprendre le comportement hydrodynamique ainsi que les caractéristiques des écoulements des eaux peu profondes demande un regard tridimensionnel (3D) de l'écoulement ainsi que de ses structures turbulentes. Cette recherche est une première étape pour étudier des couches de mélange des eaux peu profondes dans une région proche du point de convergence des courants parallèles en utilisant un cadre d'étude entièrement Lagrangien via l'utilisation de 3D Particle Tracking Velocimetry (3D-PTV).

Cette recherche étudie un modèle simplifié de la confluence d'une rivière à travers l'écoulement des courants parallèles avec des différentes vitesses (U_1 = 0.45 m/s, U_2 = 0.31 m/s), entre lesquelles une couche de mélange en eaux peu profondes se développe. Un nouveau canal de laboratoire, 9 m x 1.5 m x 0.25 m, avec des paroirs et un fond en verre a été construit. Les expériences de laboratoire ont été conduites pour une condition turbulente (Re moyen = 24,700), avec une profondeur d'eau de 6.5 cm et une pente nulle. Les mesures avec 3D-PTV ont été réalisées à partir de l'extrémité d'une planche de séparation jusqu'à une distance de 30 cm en aval. Pour faire les mesures, trois caméras à haute vitesse (600 Hz) et à haute résolution (2016x2016) CCD cameras localisées en-dessous du canal ont été utilisées. Les images enregistrées par les caméras ont été analysées en utilisant OpenPTV pour extraire l'information du champ d'écoulement. Des microsphères faites à partir de la cire de son de riz (Florabeads RBW) avec une densité relative à l'eau de ~ 1 à 25°C et une couleur naturelle, ont été semées pour tracer l'écoulement, illuminé par des lampes d'halogène. La calibration de 3D-PTV a été effectuée en utilisant un objet solide de calibration. Les données obtenues à partir de l'application de 3D-PTV ont permis l'acquisition du champ de vitesse de l'écoulement. Les données de vitesse, ensuite, ont été analysées pour obtenir des séries temporelles de vitesse ainsi que des profils transversaux de vitesse moyenne longitudinale et d'intensité turbulente de la couche de mélange en eau peu profonde. En outre, des graphiques de contour instantanées ont été générés pour comprendre le processus de mélange à l'intérieur de l'écoulement à différentes positions en aval.

Une couche de mélange d'eau en milieu peu profond formée à partir de la confluence des courants parallèles peut être divisées en deux régions en aval, une zone proche de la confluence où l'écoulement défini par la géométrie initiale évolue vers une couche de mélange, et une zone autosimilaire postérieure ou la couche de mélange d'eau en milieu peu profond a développé ces propriétés caractéristiques. Dans cette première étape de recherche le première 30 cm après la confluence des courants ont été étudiés. Dans cette région les caractéristiques suivantes ont étés observées. Des couches limites se développent à côté la planche de séparation des courants, ce qui se transforme dans un déficit de vitesse caractéristique d'un sillage (à la fin de la planche de séparation). Ce déficit de vitesse diminue en magnitude en aval mais il n'est pas complétement disparu après x = 30 cm. Le sillage a une zone de haute turbulence, grâce au gradient de vitesse entre les vitesses libres et le déficit de vitesse, zone de haute turbulence que diminue ainsi que le déficit de vitesse diminue dans la direction de l'écoulement. Le sillage formé à la fin de la planche de séparation empêche la formation et élargissement de la couche de mélange d'eau en milieu peu profond, ce qui occasionne que la largeur de la couche de mélange soit constante tout au long de la distance des mesures et qu'elle fasse un virage vers le courant lent causé par le transfert latéral du moment. En fin, le développement d'une circulation secondaire peut commencer à se former à la fin de la distance de mesure. Ce comportement se met en évidence vue que des sections d'écoulement instantanées montrent qu'il y a un flux transversal vers le courant lent en surface et vers le courant rapide au fond du canal.

ACKNOWLEDGEMENTS

I want to express my gratitude to Professor Susan J. Gaskin for giving me the opportunity to work with her, for her supervision and support. This allowed me to benefit from studying at McGill University and, in addition, she promoted me to have an international experience by presenting part of my work at the 4th International Symposium on Shallow Flows (4th ISSF).

I want to also express my gratitude to my family, who have always been my great support and to whom I want to dedicate this work.

To Professor Alex Liberzon and the OpenPTV community, as well as to Silvia Cordero, who supported me in the use of 3D-PTV, I want to express special gratitude.

To Professor Scott A. Socolofsky for acting as the examiner of this thesis document and for his valuable suggestions, thank you very much.

Likewise, I want to express my great gratitude to John Bartzack for being my guide and mentor in the laboratory; thank you for sharing your technical knowledge in the workshop and laboratory.

Also, I would like to thank Aaron Manzali, Alejandro Perez, Max Milanovic, Jennifer MDC, Sandra Mejía, Anthony Andreoli and Mohammad Alobaidi, some of my McGill friends who welcomed me and helped me throughout my studies. I want to express equal gratitude to Yury Dobronravov and Andrea Mellado, for helping me during the summer. Special thanks to A-H for taking the time to review my French translation.

Finally, I want to thank to all the people who in one way or another have helped me during the past years, your support allowed me to accomplish this new goal.

TABLE OF CONTENTS

LIST OF FIGURES

LIST OF TABLES

1. INTRODUCTION

1.1. Rationale

A shallow flow and hence a shallow mixing layer can be simply defined as a flow, found in nature, with streamwise and spanwise dimensions that exceed the vertical dimension (Jirka and Uijttewaal 2004), with a width ten to a hundred times larger than the depth, or with vertical length scales much smaller than the horizontal scales (typical aspect ratio 5% or less). A shallow mixing layer can be formed in a flow in which two streams with different velocities run side by side. This flow type can be found in several hydro-environments, for instance at river confluences, at groyne fields and at the interface of harbor entrances and a main channel.

Shallow mixing layers have been extensively studied using different techniques, i.e., laboratory experiments (presented later in detail – see section 2.1.2), analytical stability methods, numerical simulations, and field studies. The latter allows the study of shallow mixing layers and their mixing processes as they exist in nature, for example shallow mixing layers at river confluences, which is the scope of this research. Moody (1995) studied the mixing processes downstream from the confluence of the Mississippi and St. Croix rivers, using time series of vertical and horizontal profiles of temperature and specific conductance. In the near-field of the confluence the mixing was found to consist of two processes, the fluid is stirred by the advective shear instabilities and further mixed by molecular diffusion and turbulent diffusion (Moody 1995). Gaudet and Roy (1995) also studied river confluences using electrical conductivity measurements in three rivers of moderate size characterized by a bed discordance. When bed discordances are present, mixing is more efficient due to the geometry of the discordance and the resulting large-scale flow paths dominate the mixing processes, with greater discordance resulting in greater mixing under shallow flow conditions (Gaudet and Roy 1995).

Shallow mixing layers are present in different hydro-environments and understanding their dynamics is important for mixing processes. Mixing mechanisms in shallow mixing layers have been described to depend, to different degrees, on the large-scale quasi 2D horizontal turbulent motions and the 3D turbulence from the bottom friction (Babarutsi and Chu 1998, Booij and Tukker 2001, van Prooijen and Uijttewaal 2002), however, the processes remain unclear. Some

authors claim 3D turbulence to be important (Booij and Tukker 2001), and others that is negligible (van Prooijen and Uijttewaal 2002). This project is a first stage to investigate the 3D mixing processes occurring in the shallow mixing layer at river confluences thus improving the understanding of the importance of the 3D processes to the mixing. As shallow flows and hence shallow mixing layers are omnipresent in nature, understanding their physical behavior is essential to better predict shallow flows, pollutants/nutrients transport, sediment transport and erosion processes, all phenomena that can take place in nature as well as in man-made water courses.

1.2. Objectives

In this thesis, a better understanding of the topic of shallow mixing layers is sought, particularly regarding shallow mixing layers at river confluences. The following are the research objectives:

- To apply 3D Particle Tracking Velocimetry (3D-PTV) to study shallow mixing layers at a shallow river confluence.
- To study the mixing process downstream of shallow flow confluences (coflowing parallel streams) in the near-field up to 30 cm in the downstream direction, i.e. a zone characterized by strong lateral shear, and where a wake structure begins to evolve into a mixing layer.

1.3. Thesis organization

This document is structured as follows. In chapter 2, Background and Literature Review, an overview of the current knowledge of shallow flows and particularly of shallow mixing layers is reviewed. The definition of shallows flows, their occurrence, the effects of shallowness on the flow, the different turbulent motions in the flow (large-scale and small-scale turbulent motions) and shallow flows encountered in nature are mentioned. Mixing layers are defined, examples of their occurrence are provided, and their characteristic length scales and velocity scales are described. The different experimental investigations of shallow mixing layers are reviewed, and the instabilities present in shallow mixing layers are defined. The main experimental technique used in this project, 3D Particle Tracking Velocimetry (3D-PTV) is reviewed.

In chapter 3, Methodology, a description of the physical model (the flume and its components) is provided in terms of the physical aspects, the water quality characteristics, the flow verification,

and the hydraulic conditions of the experiments. A detailed description of the 3D-PTV hardware (flow tracer, cameras setup, illumination, and calibration process) and the methodology including the pre-processing and post-processing of data are discussed.

Chapter 4 (Results and Discussion) presents the results of applying 3D-PTV and their analysis. Results on the calibration of 3D-PTV and its performance are presented. Furthermore, data on flow validation and the hydrodynamics of the shear layer between parallel coflowing flows is presented. Information on transverse profiles for mean streamwise velocity and turbulence intensity is discussed. A flow deficit of a wake type flow is observed and analyzed. The downstream evolution of the shear layer width is analyzed as is the shift of the mixing layer center line. Lastly, instantaneous velocity contour plots for the y-z plane are generated to identify how mixing occurs in the near-field of the flow.

The final chapter of this document, Chapter 5 – Conclusions and recommendations, contains the outcomes of this work regarding the 3D mixing process in a shallow mixing layer between coflowing streams. Recommendations for further research are also given.

2. BACKGROUND AND LITERATURE REVIEW

In this chapter, shallow flows, and, in particular shallow mixing layers are presented. The occurrence of shallow flows, the dynamics of their flow, particularly that due to their shallowness, and their importance to engineering applications is given. Previous experimental studies of shallow mixing layers are presented. Finally, information pertinent to 3D Particle Tracking Velocimetry (3D-PTV) is reviewed.

2.1. Shallow flows

2.1.1. Shallow flows overview

Shallow flows, defined as having two horizontal dimensions (streamwise and spanwise) greatly exceeding the vertical dimension or equivalently having a large width-to-depth ratio, are commonly found in nature. Wide rivers (low-land rivers), estuaries, coastal waters, shallow lakes, the upper mixed layer of deep stratified lakes or reservoirs, are examples of shallow flows (van Prooijen, Booij et al. 2000, Jirka 2001). Typically, when the width of the flow is ten to a hundred times larger than the depth (Chu, Liu et al. 2004, Uijttewaal 2014), or when the vertical length scales are much smaller that the horizontal scales (typical aspect ratio 5% or less) (Talstra, Uijttewaal et al. 2006), then a shallow flow exists. Another important characteristic of shallow flows is that they are turbulent flows, in which at least one boundary is shear-supporting while the other may be shear-free or shear-supporting (Jirka and Uijttewaal 2004).

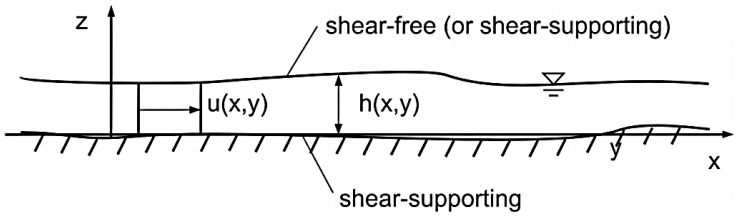

Figure 2-1. Lateral view of a predominantly horizontal flow in a vertically limited flow Figure taken from Jirka and Uijttewaal (2004)

Furthermore, shallow flows can be considered as a combination of free shear flow and open-channel, wall or base flow (van Prooijen and Uijttewaal 2005). In free shear flows, turbulence arises due to the mean-flow velocity gradient developed across a mixing layer when two currents with different velocities meet, for example at a stream confluence, whereas in the case of an open-

channel flow, turbulence arises due to shear at the no-slip bottom boundary which slows the flow and creates a velocity gradient.

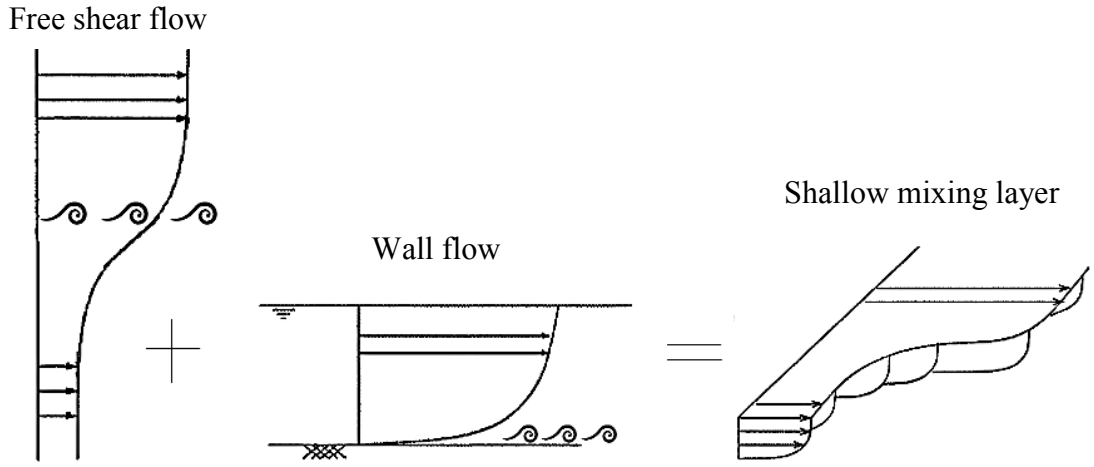

Figure 2-2. Mean streamwise velocity profiles of a shallow mixing layer
Figure adapted from van Prooijen and Uijttewaal (2005)

Shallowness makes shallow flows unique. Different authors have identified its twofold effect as follows (Chu and Babarutsi 1988, Uijttewaal and Booij 1999, Uijttewaal and Booij 2000, Booij and Tukker 2001, Uijttewaal 2009). First, the flow is vertically confined resulting in quasi two-dimensional flow features (large-scale turbulent motions) as eddies cannot develop vertically and hence are forced to grow in the horizontal plane. Second, the bottom friction plays a stabilizing role (drag effect) on the large-scale turbulent motions developing in the flow as well as on the streamwise velocities, and likewise causes the development of the boundary layer with its associated velocity gradient and three-dimensional small-scale turbulent motions.

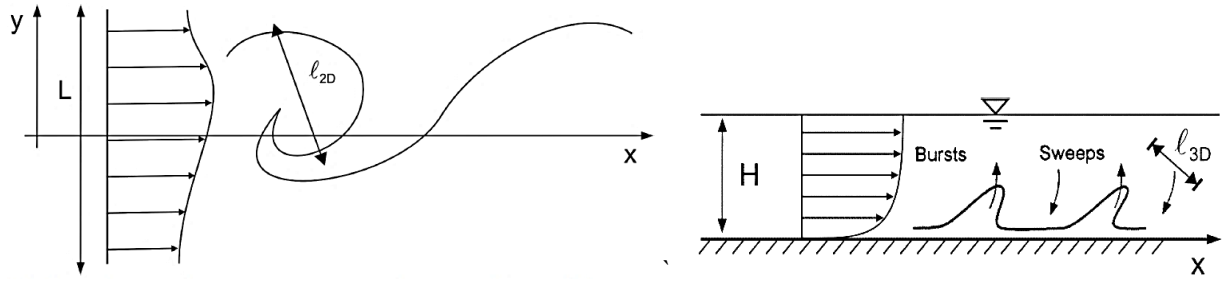

Figure 2-3. Large-scale (left) and small-scale turbulent motions (right) in shallow flows
Figure taken from Jirka and Uijttewaal (2004)

The vertical confinement of the shallow flow forces the large-scale turbulent motions to grow laterally resulting in the appearance of quasi two-dimensional coherent structures. This turbulent motion has been proposed to arise due to one of three generation mechanisms (Jirka 2001). First, the strongest mechanism, referred to as topographical forcing, occurs when topographic features (islands, headlands, jetties, groynes, etcetera) or a physical object cause the flow to separate with the subsequent formation of an intense transverse shear layer on the lee side of the topographic feature or physical object. Second, internal transverse shear instabilities, in which the instabilities grow due to a velocity gradient in the transverse direction, giving rise to the gradual growth of quasi two-dimensional coherent structures. Lastly, secondary instabilities of the base or wall flow, which, as will be explained shortly for the small-scale turbulent motions, appear as a distortion of the 3D turbulence arising from the bottom of the flow that ultimately leads to 2D coherent structures. In addition, three-dimensional small-scale turbulent motions characterized by ejection (burst) and sweep events (van Prooijen and Uijttewaal 2005) appear due to the velocity gradient in the boundary layer which develops due to the no-slip condition at the bottom of the flow.

Shallow flows are ubiquitous in nature and have been extensively studied. Three classes of shallow flows studied are uni-directional shallow jets, wakes and mixing layers (Socolofsky and Jirka 2004). A more detailed review of the mixing layers is provided as it is relevant to further understand shallow mixing layers at river confluences.

2.1.2. Shallow mixing layers

A mixing layer is developed between two parallel streams with different velocities. It is a shallow mixing layer if, in addition, the flow domain is bounded by a rigid bottom, has a free surface and the width of the mixing layer is larger than the water depth but smaller than the flow geometry (Uijttewaal and Tukker 1998, Prooijen 2004).

Shallow mixing layers can be formed in different flow configurations, for example, at the confluence of two rivers, at the interface of a main channel and a flood plain (compound channels), or when transverse variation in the bed friction material in a channel exists causing a difference in velocities (van Prooijen, Booij et al. 2000, Uijttewaal 2009). Similarly, shallow mixing layers will occur at harbor entrances and groyne fields, between the main fast flowing stream and a

recirculation zone where a sudden expansion occurs (Uijttewaal and Tukker 1998, Uijttewaal and Booij 2000).

Important length and velocity scales proposed as characteristics of shallow mixing layers are (Chu and Babarutsi 1988): h, the water depth; h/c_f, the bed-friction length scale (c_f: bed-friction coefficient that can be evaluated as proposed by the A.S.C.E. Task Force on Friction Factor in Open Channel); $\Delta = U_1 - U_2$, the velocity difference across the mixing layer; and $\bar{U} = (U_1 + U_2)/2$, the average velocity across the mixing layer.

Another important characteristic of shallow mixing layers is the stability parameter that quantifies the stabilizing effect of bottom friction on the shallow mixing layer (Chu and Babarutsi 1988). This number is defined as the ratio between the stabilizing effect of the bed friction (dissipation of turbulent kinetic energy) and the destabilizing effect of transverse shear (production of turbulent kinetic energy) (Uijttewaal and Booij 2000). A critical value (S_c) between 0.06 – 0.12 denotes the equilibrium of production to dissipation (van Prooijen and Uijttewaal 2002).

$$S = \frac{c_f \delta \bar{U}}{h\Delta} \qquad [1]$$

where δ is the width of the mixing layer and all other variables are as defined above. δ is defined as the width of the flow between the streams of constant velocity. Once the mixing layer has developed, as shown in **Figure 2-4**, this can be estimated as the ratio of the free streams velocity difference to the maximum slope thickness, ${\partial u}/{\partial y}_{max}$. This allows the mixing layer growth rate to be defined as, ${d\delta}/{d_x}$:

$$\delta = \frac{U_1 - U_2}{\left({\partial u}/{\partial y}\right)_{max}} \qquad [2]$$

$${d\delta}/{d_x} = \alpha 2 \frac{U_1 - U_2}{(U_1 + U_2)} \qquad [3]$$

where the subscript max denotes the maximum value over the velocity profile (see **Figure 2-4**), and α is a constant of proportionality that has an empirical constant value of about 0.09 in most cases (Uijttewaal and Booij 2000).

Moreover, in the self-similar region, mixing layers are characterized by the velocity profile shown below (see **Figure 2-4**), in which U is the local streamwise velocity, $R = (U_2 - U_1)/(U_2 + U_1)$, y is the transverse coordinate and l is the transverse length scale (Daoyi and Jirka 1998).

$$\frac{U}{\overline{U}} = 1 + Rtanh\left(\frac{y}{l}\right) \quad [4]$$

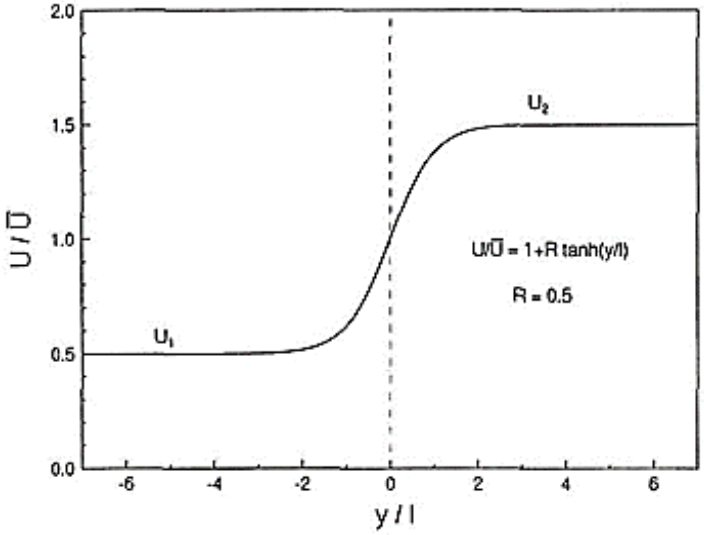

Figure 2-4. Non-dimensional velocity profile for a mixing layer with R=0.5
Figure taken from Daoyi and Jirka (1998)

Shallow mixing layers are important in hydraulic, environmental, and geophysical situations, as they play a key role in the lateral and longitudinal transport of mass (contaminants and sediments) and momentum as well as for having a capacity of mixing these quantities. Their understanding is vital in the prediction of shallow flows, sediment transport and erosion, and pollutant/nutrient transport.

As for shallow flows, mixing layers have two distinct turbulent motions: large-scale turbulent motions associated with the transverse shear and small-scale turbulent motions associated with the bottom friction (Chu and Babarutsi 1988), having a particular characteristic structure, the quasi two-dimensional (2D) and three-dimensional (3D) structure respectively.

Several approaches have been used to study shallow flows and hence shallow mixing layers: laboratory experiments, stability analyses, numerical simulations and field work (Jirka and Uijttewaal 2004). In terms of laboratory experiments, studies have focused on shallow mixing layers using different experimental techniques.

Chu and Babarutsi (1988) studied the development of a shallow mixing layer to investigate confinement and bed-friction effects. In their work, hot-film anemometry was used to acquire point velocity statistics at different cross sections of the flow in a shallow flume. The effect of bed-friction on the growth of the mixing layer and on the velocity gradients in the shallow mixing layer were identified as a stabilizing effect. The authors observed that the initial spreading rate of the shallow mixing layer was double than that of a deep mixing layer (Chu and Babarutsi 1988), a result questioned by later findings claiming that the mixing layer width grows at the same rate as that of a deep mixing layer (Uijttewaal and Tukker 1998, Uijttewaal and Booij 2000). The authors also detected that with a decrease in bed friction length scale, $h/\overline{c_f}$, the growth rate of the mixing layer reduces from a linear growth rate to asymptotically approach a constant value further downstream, demonstrating that at higher levels of confinement the growth of the mixing layer width decreases. This was described in the proposed entrainment hypothesis, in which the transverse spreading rate ($d\delta/dx$) of the mixing layer reduces as the bed-friction influence becomes more important in the far field. The phenomenon is explained by an entrainment coefficient (α) defined as $\alpha = {}^{1}/_{\Delta}\,{}^{dx}/_{dt}\,{}^{d\delta}/_{dx} = {}^{\overline{U}}/_{\Delta}\,{}^{d\delta}/_{dx}$.

Uijttewaal and Tukker (1998) used Laser Doppler Anemometry (LDA) in order to study the large quasi two-dimensional structures in a shallow mixing layer over a 2 m distance downstream from the mixing layer's starting point. The authors showed, by means of one-dimensional power spectra for spanwise and longitudinal velocity fluctuations and space and time correlations, how the large turbulent motions in the mixing layer evolve and behave in streamwise as well as spanwise directions. Estimations of characteristic length and time scales, 'up-cascade' phenomenon and vertical extension of structures were analyzed. Characteristic streamwise sizes of large-scale motions were found to be 180 mm (at x = 0.5 m) and 560 mm (at x = 2 m), for a water depth of 0.07 m in a 3 m wide flume with a Δ= 0.18 m/s, showing how turbulent motions grow in amplitude with downstream distance. Also the authors showed the deviation of the typical velocity profile of a mixing layer at the apex of the splitter plate due to a wake appearing from the boundary layer formed therein (Uijttewaal and Tukker 1998). Following this study, Uijttewaal and Booij (2000) studied the influence of bottom friction on the development of the mixing layer. They used LDA to capture velocities in the horizontal plane (u, v) allowing them to analyze the evolution of the mixing layer for two water depths scenarios, 42 and 67 mm. This lead to the conclusion that

a higher width-to-depth ratio, i.e. a stronger dissipation due to bottom friction, has a strong effect on the behavior of turbulence reducing it for the shallower flow (destroying the coherence in large structures), as energy production from lateral shear is not enough to support the growth of large-scale turbulent motions. This behavior was proved, for example, by the authors findings for the autocorrelation functions of spanwise velocity fluctuations in which for the shallower flow, 42 mm, the strong initial modulation is completely lost, and also through the power spectra analysis of spanwise velocities that the shallower flow does not exhibit the -3 slope indicative of two-dimensional turbulence (Uijttewaal and Booij 2000).

Similarly to Chu and Babarutsi (1988), Uijttewaal and Booij (1999) studied the development of shallow mixing layers. In their experiments, LDA was used to show that bottom friction plays an important role not only in the growth of the mixing layer but also in the strength and dimensions of the large quasi two-dimensional turbulent structures of the flow; a faster decay in the coherence of large-scale turbulence and lower Reynolds stresses were observed in the shallower experimental case (Uijttewaal and Booij 1999).

Prooijen, Booij and Uijttewaal (2000) conducted a study to look at the mixing layer behavior under two conditions: a mixing layer at river confluences and a mixing layer from a compound channel. By means of Particle Tracking Velocimetry (PTV) and Laser-Doppler Velocimetry (LDV), the detection and characterization of large scale horizontal structures and the determination of their influence on lateral exchange was achieved. The authors demonstrated how the use of vorticity and enstrophy allows for the characterization of large structures present in the flow, which play an important role in shallow mixing layers. The LDV measurements showed as well how the acceleration of the slow stream and deceleration of the fast stream in a mixing layer leads to a slight deviation of the centerline of the shallow mixing layer (van Prooijen, Booij et al. 2000).

Studies have also been undertaken to investigate changes in the inlet conditions on a shallow mixing layer. Prooijen, de Nijs and Uijttewaal (2004) compared the cases of a shallow mixing layer in parallel streams created by a smooth (glass) and a stone bed (enhanced) inlet condition; the stone bed inlet condition was present in the direction of the flow from the beginning of the inlet to the apex of a splitter plate. In their work, LDA measurments were taken and statistical and spectral analysis used. The study results showed how the stone bed inlet condition significatly

affects the development of the mixing layer in the near and far field, generating stronger coherent structures when the flow conditions are enhanced. For example, a comparison in the transverse profiles for $<u'u'>$, $<u'v'>$ and $<v'v'>$ at a downstream distance of 4 m showed an increase in magnitude by a factor of 1.8, 1.8 and 2.0, respectively, for the enhanced stone bed inlet condition (van Prooijen, De Nijs et al. 2004).

Expanding on previous work, Uijttewaal (2009 & 2014) compiled the findings of shallow mixing layers behaviour under five different conditions of imposed velocity gradients: inflow conditions (confluence), lateral variation in water depths (compound channel), a transverse obstacle, groyne fields and roughness induced shear layers. The different flow configurations showed, by means of PTV, dye visualization, dye visualization and Particle Image Velocimetry (PIV), LDA, Acoustic Doppler Velocimetry (ADV) and PTV, respectively, that although for all cases a shallow layer will be formed with a mean streamwise velocity profile that looks similar, the development of the shear layer and the coherent structures therein will be different as defined by the presence of three types of flow structures: quasi two-dimensional eddies with veritcal vorticity, three-dimensional small-scalle turbulence and secondary circulation with streamwise vorticity (Uijttewaal 2009, Uijttewaal 2014).

2.1.3. Instabilities in shallow mixing layers

Transport phenomena in shallow mixing layers are dependent on the existence of two flow instabilities. The Kelvin-Helmholtz instability rising from the transverse velocity shear and the Tollmien-Schlichting instability appearing due to bottom friction.

Shallow flows can be thought of as a combination of two types of flow archetypes, free shear flow and open-channel flow, each one with their particular turbulent motion (see section 2.1.1). The first is characterized by the existence of large-scale turbulent motions in the transverse profile appearing due to the transverse gradient in streamwise velocity. The large-scale turbulent motions can originate at the inflection point in the transverse velocity profile. When this condition exists, the Kelvin-Helmholtz instability appears and can further develop leading to the birth of horizontal eddies as encountered in shallow mixing layers (van Prooijen and Uijttewaal 2005). As previously observed (Mollo-Christensen, Pesetsky et al. , Brown and Roshko 2006), these instabilities are characterized by being as large as the width of the mixing layer and for having a vertical axis of rotation. The physical mechanism of the Kelvin-Helmholtz instability has been

described by Batchelor (1967), in which an initial disturbance slightly displaces a vortex sheet generating sinusoidal displacements. This movement will be amplified as positive vorticity is accumulated, leading to exponential growth of the disturbance that will continue as long as it is small enough to not significantly affect the basic state (Drazin and Reid 2004). The Kelvin-Helmholtz instability is common not only in liquids such as water, as in the case of this study, but also in the atmosphere, and it occurs when an abrupt interface with a discontinuity in velocities is present (Liggett 1994), or where there is a sharp interface between two fluids of different density at the initiation of flow with a velocity difference between the layers.

On the other hand, the Tollmien-Schlichting instability is a characteristic of open-channel flow. Tollmien-Schlichting waves occur in a viscous boundary layer with the transition from laminar to turbulent flow. Klebanoff et. al (1962) observed three stages by which these waves evolve into turbulence: in a first stage, they have a two-dimensional structure with a horizontal axis of rotation normal to the flow. As they travel downstream, they grow in amplitude reaching a critical point after which they become perturbed three-dimensionally (second stage) giving onset to turbulence spots (third stage) (Klebanoff, Tidstrom et al. 1962). Furthermore, as mentioned by Jirka and Uijttewaal (2004), the structure of the turbulent structures appearing from open-channel flow are produced by ejection and sweep events with hairpin vortices being one type of structures therein with a vertical length scale smaller or equal to the water depth (Jirka and Uijttewaal 2004).

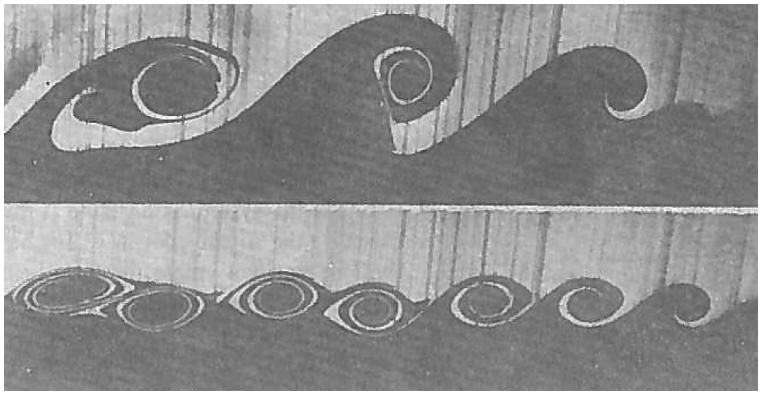

Figure 2-5. The Kelvin-Helmholtz instability
Figure taken from Liggett (1994)

2.2. 3D Particle Tracking Velocimetry (3D-PTV)

3D-PTV is a nonintrusive optical velocimetry technique allowing for the determination of trajectories and velocities in a three-dimensional (3D) observation volume. It is suitable for

Eulerian and Lagrangian measurements in a flow field (whether laminar or turbulent). In this technique, the observation volume, which is seeded with particles, is recorded in image sequences from different viewing angles to allow for stereoscopic determination of the 3D coordinates of particles and hence their trajectories, and velocities as well as velocity gradients along particles trajectories. By means of 3D-PTV, it is possible to obtain a full field of velocity and velocity derivatives in addition to Lagrangian acceleration and its spatial derivatives (Virant and Dracos 1997, Consortium 2014, Akutina 2016, IfU 2016). A brief description of 3D-PTV follows. A full and detailed description of 3D-PTV can be found in the papers by Mass et al. (1993) and Malik et al. (1993) (Maas, Gruen et al. 1993, Malik, Dracos et al. 1993) and in broader scope in Dracos (1996), chapter 3 (Dracos 1996). 3D-PTV evolved from PTV and the largest developments in this technique came from the ETH Zurich, where the Institute of Geodesy and Photogrammetry in collaboration with the Institute of Hydromechanics and Water Resources Management developed the complete system (hardware components and mathematical model) (Maas, Gruen et al. 1993).

To study any flow by means of 3D-PTV some basic hardware components are required, i.e., a light source that is roughly uniform over the whole observation volume, seeding of the flow with small, reflecting and neutrally buoyant particles acting like tracers or flow markers, high speed cameras defining the time resolution of the flow field as $\tau/\Delta t$, where τ is Kolmogorov micro time scale and $\Delta t = 1/f_c$ with f_c being the imaging frequency and, lastly, a proper calibration procedure (Maas, Gruen et al. 1993, Virant and Dracos 1997, Kim 2015, Akutina 2016). The time resolution of the flow field is only possible if the image spatial resolution is such that a particle's displacement can be detected in one time interval, Δt. Once the components indicated above and depicted in **Figure 2-6** are setup, the following process is undertaken to obtain the velocity field in three-dimensions.

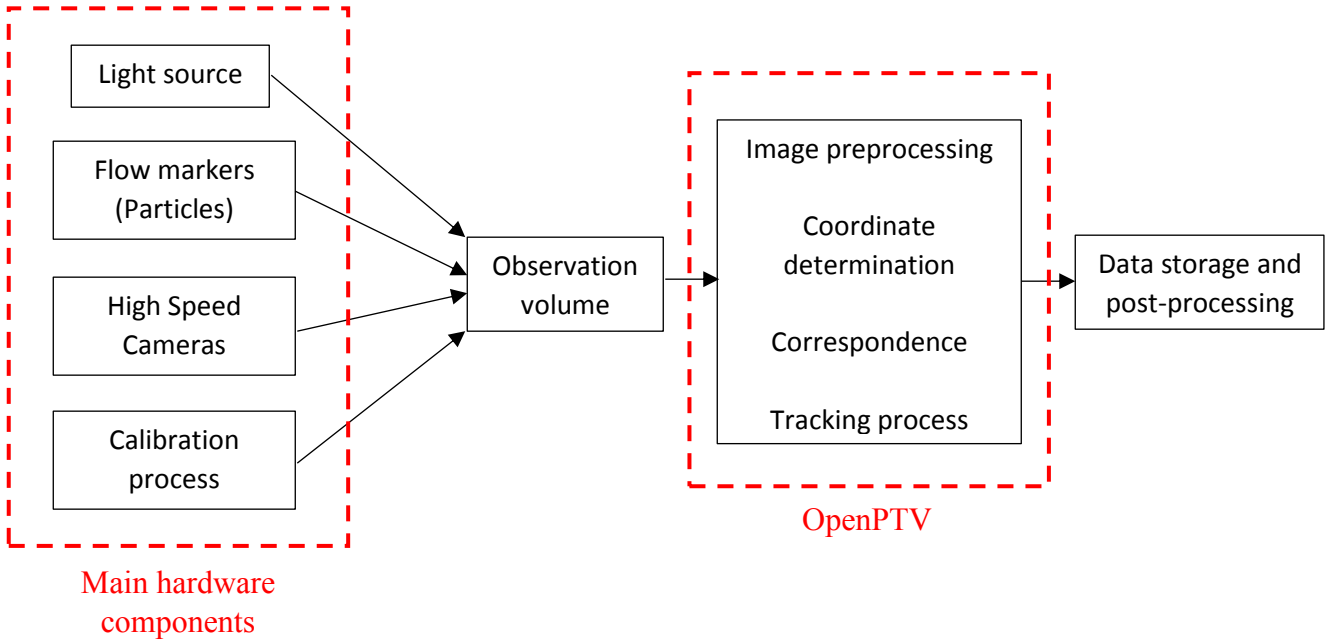

Figure 2-6. 3D-PTV components and analysis

3D-PTV directly obtains Lagrangian data (due to the tracking of particles), and this data can be processed to obtain Eulerian information of the flow. The evolution of coherent structures in the flow can be obtained by mounting the cameras on a platform moving at approximately the mean velocity of the flow (Virant and Dracos 1997). The method described below was developed primarily by the ETH group and is used in the OpenPTV methodology (see section 3.3.5). This method, as presented by Virant and Dracos (1997), Mass et al. (1993), Jin-Tae (2015) and the OpenPTV Consortium (Consortium), treats the images sequence as follows. The captured images are pre-processed (high pass filtering of raw images) to eliminate background noise and grey level variations due to the illumination intensity. The coordinates of the particles are then determined with sub-pixel accuracy in each frame by detecting the center of the seeded particles. Photogrammetric methods are used to i) establish correspondences of the particles images in the different views by using the method of epipolar lines and ii) to determine the coordinates of the particles in three-dimensions in the observation volume. Space coordinates of the particles are computed by optical triangulation making use of the collinearity condition of the projective geometry of imaging, which results in a bundle model. This model includes 6 parameters for the exterior and 3 for the interior camera orientation, 5 parameters for the correction of lens distortions and 2 parameters for the correction of electronic distortions, accounting for a total of sixteen

parameters for each camera used. These parameters are determined by means of calibration before an experiment is performed:

- Exterior camera orientation parameters: Xo, Yo, Zo coordinates of the projective center, and ω, φ, κ orientation angles of the optical axis.
- Interior camera parameters: x_h and y_h being the principle point coordinates and c a camera constant – computational imaging width.
- Lens distortion parameters modeling the radial and tangential distortion: k_1, k_2, k_3, p_1, p_2.
- Correction of electronic distortions: s_x, horizontal scale factor and δ accounting for shearing effect.

Once the coordinates $x_i\ (t) = 1, 2, 3$ of the imaged particles in the object space are known for each time step, a tracking procedure in the images sequence is applied establishing links between particle positions in consecutives time steps based on the nearest neighbor principle. This procedure defines the trajectories from which the velocity components can be calculated as follows,

$$u_i(t) = \frac{x_i(t + \Delta t) - x_i(t)}{\Delta t} \qquad [5]$$

Mass et al. (1993) has pointed out some of the advantages of 3D-PTV. The technique allows for the determination of many 3D trajectories of discrete particles in a fully 3D observation volume, therefore it is a truly Lagrangian technique providing information as displacements vectors over time, that the Eulerian point techniques of hotwire anemometry or Laser Doppler Anemometry (LDA) cannot. This implies that the spatial resolution of 3D-PTV is higher, as the acquired velocity information is not restricted to a single measurement location for a given instant (Maas, Gruen et al. 1993).

3. METHODOLOGY

The following sections describe the experimental methodology used for the study of mixing between coflowing parallel streams to model a shallow flow confluence in the laboratory. Details of the laboratory channel facilities (flume), the hydraulic parameters, as well as the measurement technique used in this work are provided. Likewise, a verification on the flow conditions that can be obtained in the new flume is discussed.

3.1. Experimental setup

3.1.1. Flume

Experiments took place in the Hydraulics Laboratory of the Civil Engineering and Applied Mechanics department at McGill University. To study shallow flows, a new recirculating flume was built, and, as this research was its first use, it was set up to study a shallow flow mixing layer between two parallel streams.

The recirculating flume had a glass sides and bed with channel dimensions of 9 m x 1.5 m x 0.25 m with an inlet and an outlet reservoir, see **Figure 3-1**. Recirculation of the flow was accomplished using an in-line mounted centrifugal pump ($8x8x9^{1/2}$) fed from the outlet reservoir and supplying the inlet reservoir via two diffusers. To create two parallel streams of different velocity, the inlet reservoir was separated into two by a blunt-ended splitter plate of 3.5 mm thickness, located at the midplane of the inlet tank. The total length of the splitter plate (from the back of the reservoir) was 3.65 m, with an effective length of 1.75 m (effective as water travels this distance in a horizontal plane). The flow rate was controlled just upstream of the diffusers with butterfly valves. To distribute the flow uniformly over the width of the reservoir and to decelerate it, the diffusers inside the inlet reservoir were T shaped with circular holes uniformly located over the bottom half of their surface area. A uniform flow into the flume was enabled using a transition curve to connect the channel to the inlet reservoir (see **Figure 3-1**). Appendix B presents the coordinates of the transition curve.

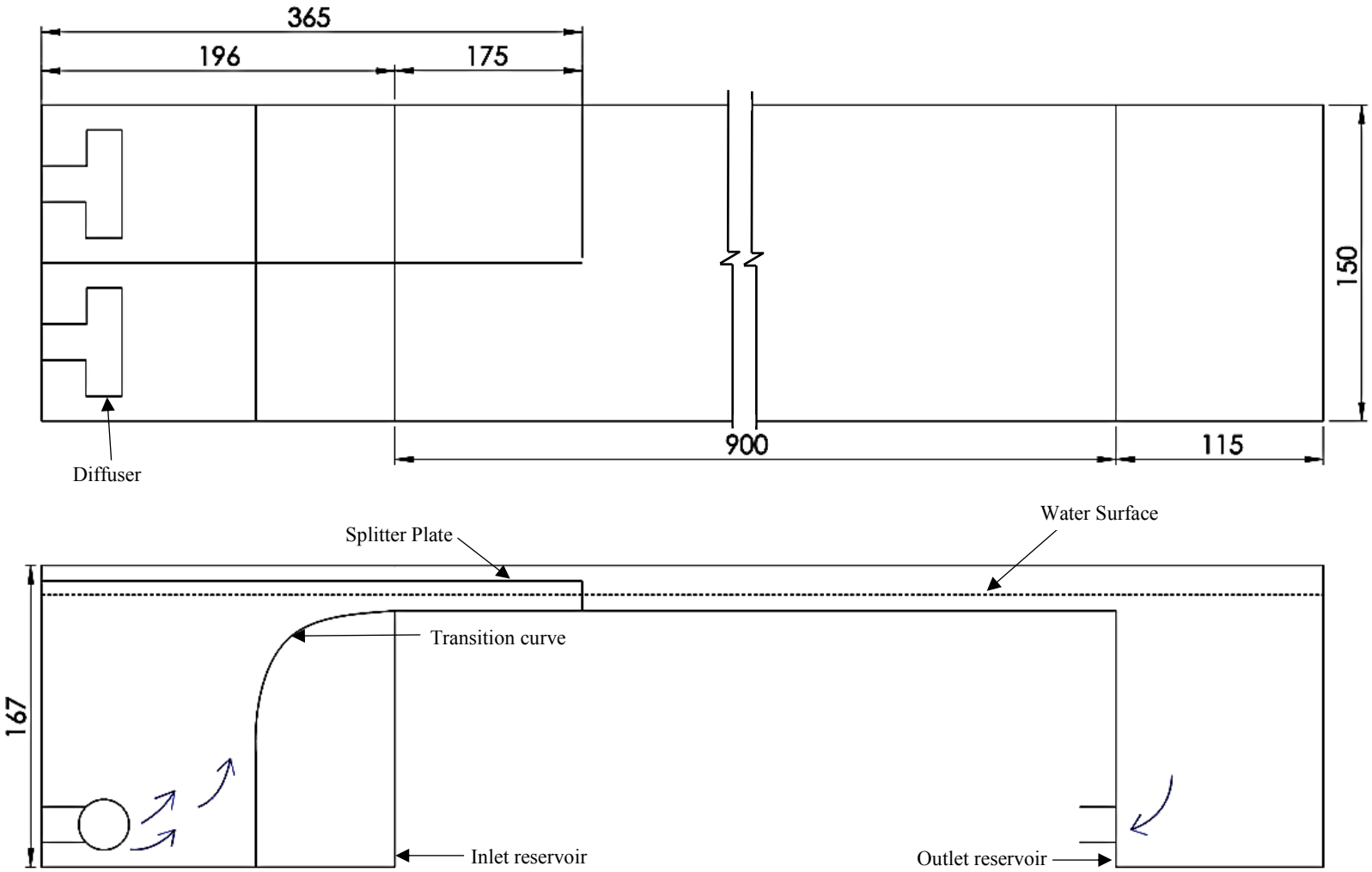

Figure 3-1. Recirculating flume – top view and side view. Dimensions are in cm. Arrows denote the direction of the flow

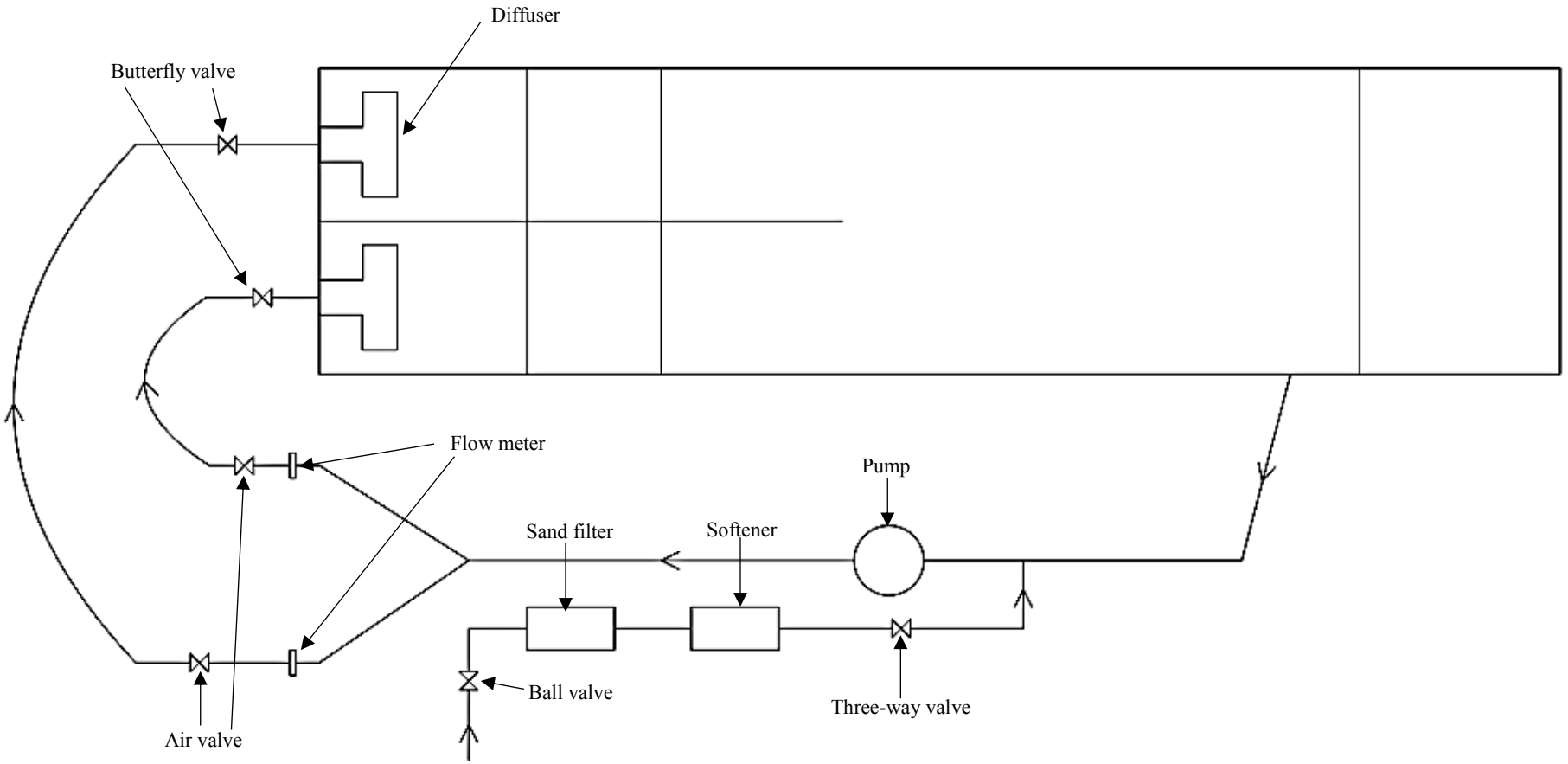

Figure 3-2. Recirculating flume schematic (top view). Arrows denote the direction of the flow

The flowrate was measured at each supply pipe entering the inlet reservoir with a flow meter (SITRANS F M MAG 5100 W). A depth gauge was used to measure the water level during experiments near the end of the splitter plate (see **Figure 3-3**).

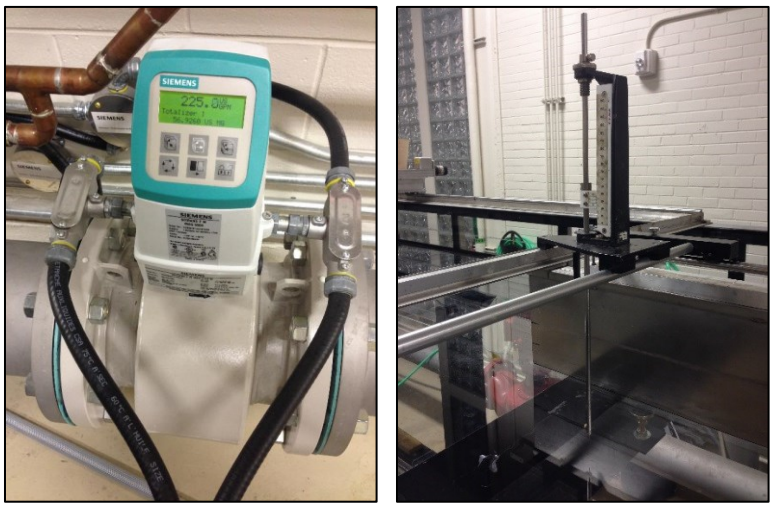

Figure 3-3. Flow meter (left) and depth gauge (right)

3.1.2. Water quality

Water taken directly from the city supply system was deemed not suitable for 3D-PTV due to the hardness and suspended material content. It was observed previous installation of a sand filter and a water softener, that after using the flume salt deposits and solids accumulated on top of the glass. To guarantee a suitable water quality, two filters working in series were installed in the supply line. First a sand filter (Jacuzzi Laser 192) was put in place to remove suspended particles and hence reduce turbidity followed by a water softener (Pentair model 268/764) to reduce water hardness, i.e. carbonates concentration - see **Figure 3-2**. Homogeneous thermal conditions for the tests were established to prevent differential expansion of the flume structure, which could lead to leakages. This was achieved by filling the tank with water, controlled by a thermal valve, at the ambient room temperature.

3.1.3. Flow verification

Since the flume used in this research was newly built and had not yet been used, a flow verification was necessary. In the verification, the flow conditions in the inlet reservoir were analyzed to examine the effect of the inlet diffuser and the transition curve on the uniformity of the flow in the channel. The flow conditions in the inlet reservoir and at the tip of the splitter plate

where the coflowing streams meet were analyzed for this assessment. The flow verification was also useful to investigate the range of velocities possible in the flume to inform the selection of the hydraulic conditions to be investigated, described in section 3.2. To conduct the flow verification two approaches were used, numerical simulations and Acoustic Doppler Velocimetry (ADV) measurements as described below.

Numerical simulations were run using Flow-3D, a Computational Fluid Dynamics software from Flow Sciences, to analyze the flow conditions and to investigate possible flow correction configurations in the inlet reservoir. The simulation scenarios were run modelling half of the inlet reservoir and channel (due to symmetry). A steady flow of water at 20 °C with a constant flowrate of 20.50 L/s entering through the diffuser in the inlet reservoir was modelled, in a physical domain of 1.96 m x 0.75 m x 1.67 m resolved using a linked blocks mesh with a higher number of mesh cells near the inlet entrance and at the diffuser location. The boundary condition between mesh blocks was conservation of mass, and the inlet and outlet boundary conditions were constant flow and constant head (pressure), respectively. The free surface boundary condition was set to atmospheric pressure and all other boundary conditions were walls with a no-slip condition. The Renormalized Group (RNG) k-ε turbulent model in Flow-3D was selected. The simulation times were set to 50 s, with convergence being attained in all cases after 20 s. Results of velocity contours in the x-z plane for the different simulation configuration are presented in **Figure 3-4** to **Figure 3-8**, in which different flow correction methods where analyzed to assess their ability to remove and/or control the existence of undesirable flow features (the appearance of two turbulent jets resulting in surface waves and preferential flow paths).The baseline simulation (**Figure 3-4**) indicates the development of two jets within the flow domain, one flowing along the bottom of the inlet reservoir and persisting to the transition curve. In addition, another smaller jet can be observed that flows up the back wall of the inlet reservoir. These two jets are hypothesized to be the cause of turbulence at the surface of the inlet reservoir and at the end of the transition curve (as observed by looking at the water surface in the inlet reservoir) at high flow rates.

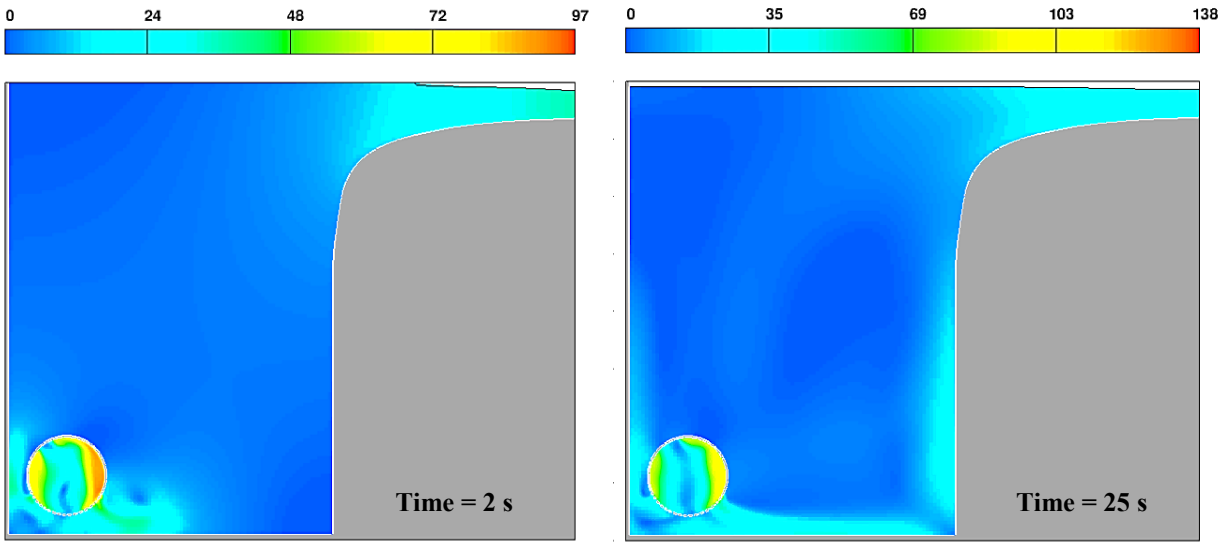

Figure 3-4. Velocity magnitude contours (cm/s) – base line simulation

As both jets in **Figure 3-4** are an undesired flow features, different simulation configurations were tested to evaluate a mechanism by which the jets and their effect, hypothesized to be responsible for the appearance of surface waves and preferential flow paths, could be removed or controlled. From the results presented in **Figure 3-5** to **Figure 3-8** one can see that a physical barrier forcing the jets to go to the back wall of the inlet reservoir appeared to be a good option, as in all cases the jets are forced to break up and bend back to enter the flume bed in a horizontal way. Also from the numerical simulations results in **Figure 3-5** to **Figure 3-8**, it seems that the arrangement of the holes in the diffuser causes the appearance of jets. It is possible that holes uniformly positioned over the entire diffuser surface rather than just at the bottom half would eliminate the formation of these jets.

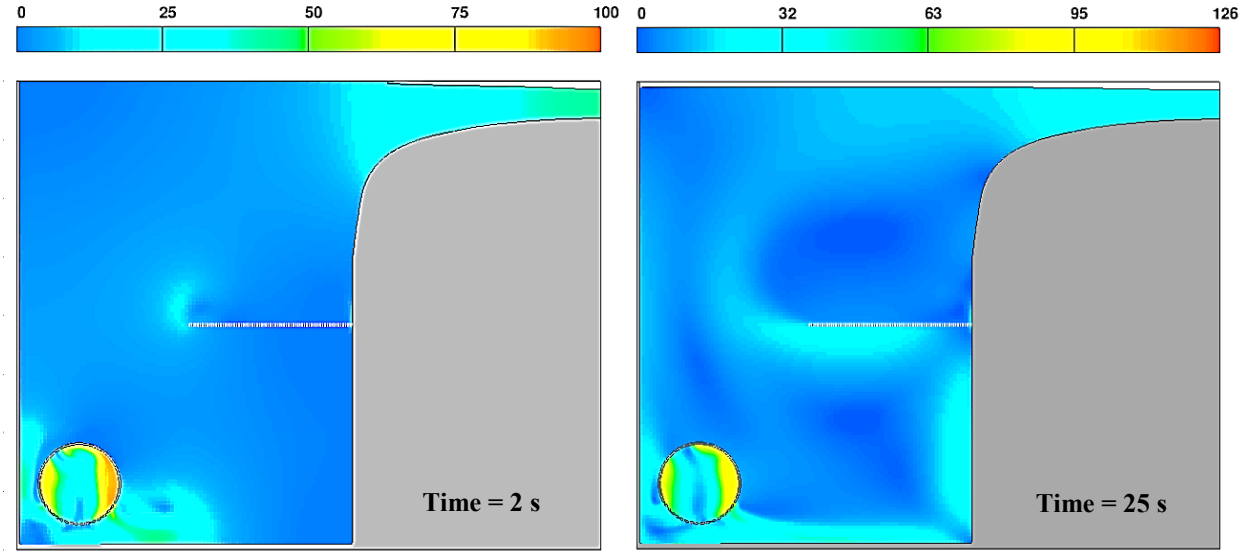

Figure 3-5. Velocity magnitude contours (cm/s) – single baffle simulation

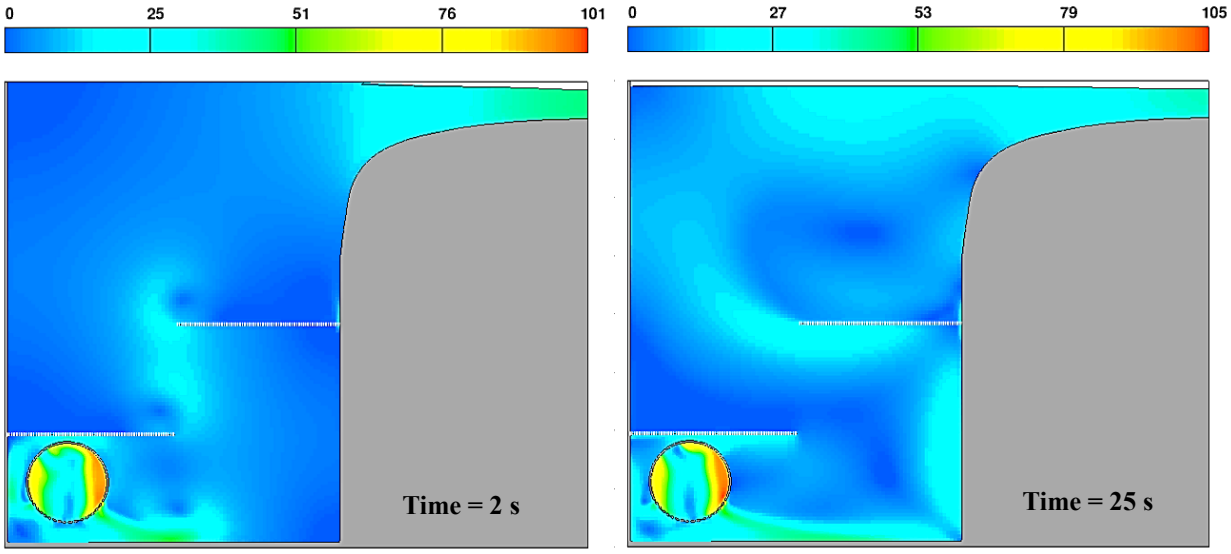

Figure 3-6. Velocity magnitude contours (cm/s) – two baffles simulation

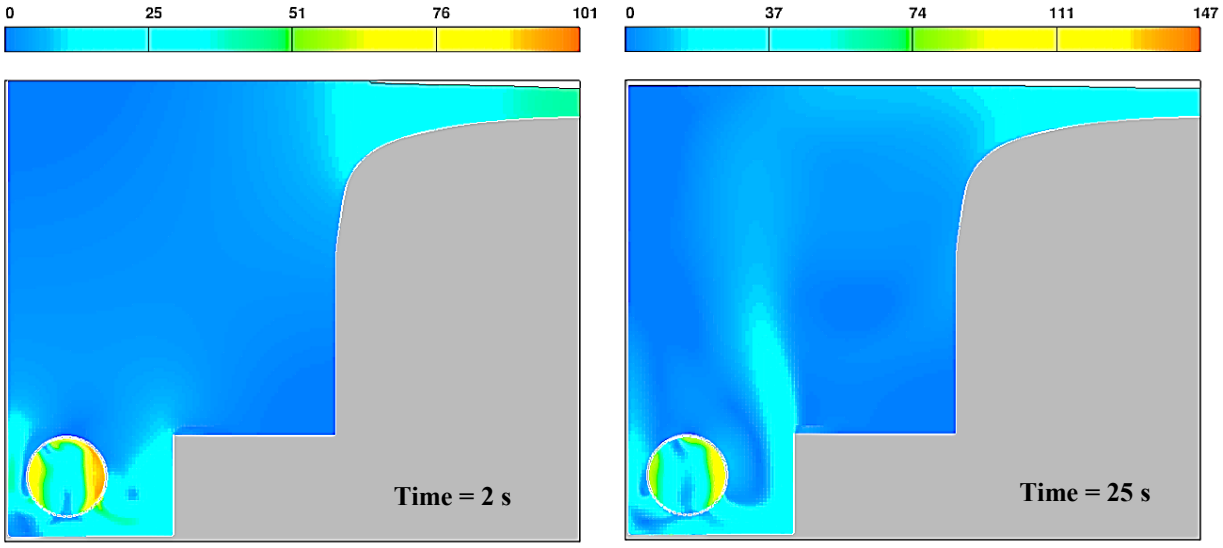

Figure 3-7. Velocity magnitude contours (cm/s) –block simulation

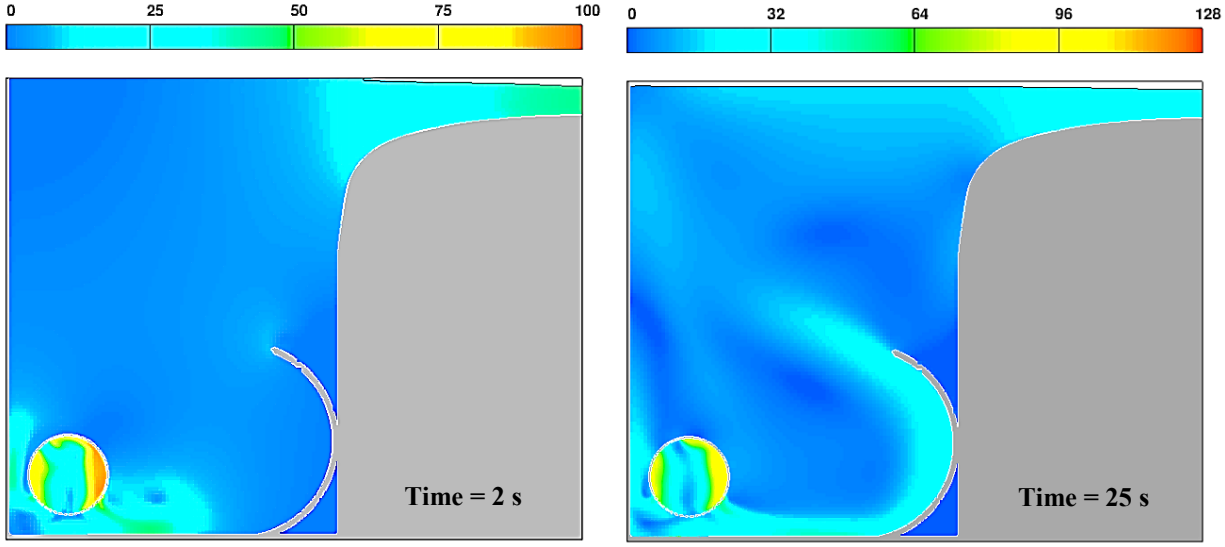

Figure 3-8. Velocity magnitude contours (cm/s) –deflector simulation

Even if the redesign and construction of a new diffuser and the construction of a physical barrier seemed to remove and/or control the existence of undesirable flow features (the appearance of two turbulent jets resulting in surface waves and preferential flow paths), a further assessment of the physical flow by measuring local velocities using an Acoustic Doppler Velocimeter was executed. Since the flow disturbances for the minimum flow rate in the flume (Q28.3% ~ 18.6 L/s, percentage denoting the capacity of the pump) were minor, it was proved that they could be mitigated using the practical, functional, and less expensive option of using Styrofoam sheets in combination with stainless-steel honeycombs (7.5 cm x 75 cm x 16 cm, with hexagonal shape and

walls of 0.5 cm) in the inlet reservoir. The Styrofoam sheets (a total of 2 sheets per stream, before and after the honeycomb) were located on top of the water surface at the inlet reservoir in combination with honeycombs, placed at the end of the transition curve, to remove surface waves and straighten the flow, respectively. The Styrofoam sheets on the water surface and the honeycombs at the end of the transition curve proved to be sufficient to remove surface waves and result in a horizontal flow at the end of the transition curve and an almost uniform velocity profile across the flume width (see **Figure 3-12** to **Figure 3-15**).

Acoustic Doppler Velocimetry (ADV) measurements were used to evaluate the simulation base case (i.e. with no deflectors installed) by measuring a transverse profile of streamwise velocity. The use of the Styrofoam sheets and/or honeycombs was also evaluated from a transverse velocity profile and the use of both the Styrofoam sheets and the honeycomb resulted in an almost uniform profile at the tip of the splitter plate. The Acoustic Doppler Velocimeter is a three-dimensional velocity sensor based on the Doppler shift effect that measures at a point (or small volume) (Lohrmann, Cabrera et al. 1994). A Vectrino (Nortek) sensor having a transmitter and four receivers, which are equally angled and symmetrically arranged around the transmitter (see **Figure 3-11**), was used. Measurements were made by locating the Vectrino sensor at 20 different locations across a transverse transect to measure the local streamwise velocity of the flow at 3 cm and 6 cm from the flume bed (see **Figure 3-9**). All measurements were made at the end of the splitter plate.

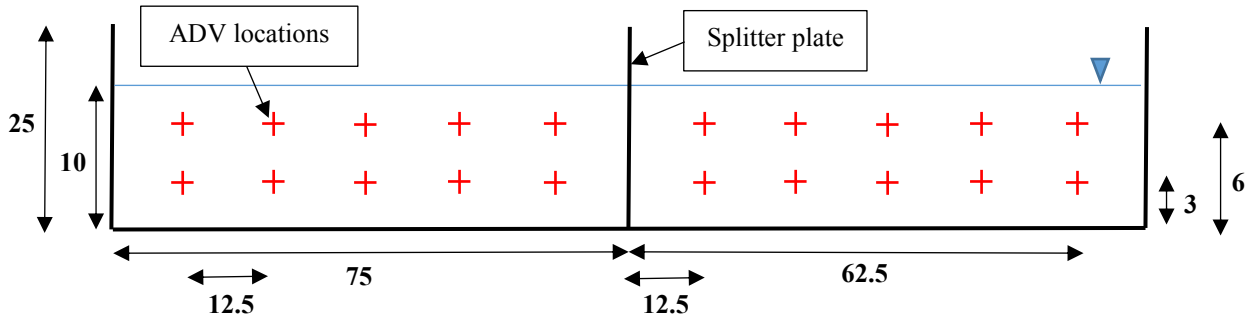

Figure 3-9. Spanwise ADV measurement locations at the end of the splitter plate (all dimensions in cm)

To measure at the specific points in **Figure 3-9**, a traversing system was built and placed above the flume. The traversing system used a stepper motor to move the sensor in the vertical and transverse directions with a position accuracy of one hundredth of a millimeter (see **Figure 3-10**).

Figure 3-10.ADV transversing system

As the Acoustic Doppler Velocimeter had a downlooking probe (**Figure 3-11**), measuring three-dimensional velocities close to the flume bed in shallow flow conditions (water depth of 10 cm) was subject to large errors, as the ultrasonic pulses produced and received by the sensor could not be distinguished from the bottom echo generated when the pulses hit the flume bed.

Figure 3-11. ADV downlooking probe
Figure taken from Nortek

To overcome this problem, the Vectrino sensor was placed facing the flow. The streamwise velocities were measured using the vertical component of the Vectrino sensor, as this component has a lower error than the other components (Khorsandi, Mydlarski et al. 2012). To ensure the ultrasonic pulse signal reflection, almost neutrally buoyant glass particles were used to seed the flow (Potters Industries Sphericel hollow glass spheres). The particles have a density of 1.10 g/cm^3 and a size distribution between 5 to 25 µm. To guarantee a Signal-to-Noise ratio (SNR) above 15 over all measurements, a total of 100 g of particles was used in the flume (volume of 8.4 m^3). Measurements were collected for 5 minutes, at a sampling rate of 25 Hz, and data was postprocessed to remove velocities with a SNR below 15 (Lohrmann, Cabrera et al. 1994). All data was collected with an accuracy of ± 1% of measured values and with four significant figures.

The water depth was maintained constant at 10 cm, value that differs from that used in the 3D-PTV measurements, but necessary to have a sufficient water column for the full submergence of the probe. **Table 3-1** summarizes information on the ADV use, the flow rates, the mean streamwise velocities and the standard deviation of the data for the flow rate used in this research, Q28.3% ~ 18.6 L/s (where Q28.3% is 28.3% of the maximum possible flow of the pump). This information, in addition to **Figure 3-12** to **Figure 3-15**, was used to assess the use of the Styrofoam sheets and honeycombs in improving flow uniformity. Appendix A contains the information on the ADV measurements for two different flow rates, Q40% ~ 25.5 L/s and Q50% ~ 32.5 L/s.

Table 3-1. Summary of ADV measurements Q28.3% ~ 18.6 L/s

FLOW RATES INFORMATION											
Pump capacity	Slow Stream (L/s)					Splitter plate	Fast Stream (L/s)				
28.30%	17.8 ± 0.1%						19.4 ± 0.1%				
ADV INFORMATION											
ADV	Vectrino from Nortek										
Sampling rate	25 Hz										
Sampling time	5 min										
Water depth	10 cm										
Sampling location	Tip of the splitter plate (see **Figure 3-1**)										
VELOCITY MEASUREMENTS FOR PUMP CAPACITY Q28.3% = 18.6 L/s											
Vert./Horiz. Position (cm)	-62.5	-50	-37.5	-25	-12.5	0	12.5	25	37.5	50	62.5
No Styrofoam nor honeycomb											
Streamwise velocity (m/s)											
6	0.2398	0.2446	0.2495	0.2482	0.2425		0.2672	0.2674	0.2731	0.2651	0.2652
3	0.2360	0.2335	0.2368	0.2381	0.2379		0.2674	0.2566	0.2629	0.2564	0.2633
AVERAGE	0.2407						0.2645				
Standard deviation (cm/s)											
6	0.40						0.33				
3	0.19						0.47				
AVERAGE	0.29						0.40				
Use of Styrofoam											
Streamwise velocity (m/s)											

Table 3-1. Summary of ADV measurements Q28.3% ~ 18.6 L/s

6			0.2632	0.2624	0.2680	0.2648	0.2637
3			0.2598	0.2512	0.2585	0.2574	0.2598
AVERAGE			0.26088				
Standard deviation (cm/s)							
6			0.22				
3			0.36				
AVERAGE			0.29				
Use of Honeycomb							
Streamwise velocity (m/s)							
6			0.2693	0.2638	0.2715	0.2686	0.2692
3			0.2543	0.2465	0.2556	0.2528	0.2510
AVERAGE			0.26026				
Standard deviation (cm/s)							
6			0.28				
3			0.35				
AVERAGE			0.32				
Use of Styrofoam and honeycomb							
Streamwise velocity (m/s)							
6			0.2689	0.2712	0.2684	0.2726	0.2675
3			0.2511	0.2465	0.2509	0.2493	0.255
AVERAGE			0.26014				
Standard deviation (cm/s)							
6			0.21				
3			0.31				
AVERAGE			0.26				

In **Figure 3-12** to **Figure 3-15** one can observe the mean local streamwise velocity profiles obtained with the Vectrino Acoustic Doppler Velocimeter and presented in **Table 3-1**. **Figure 3-12** presents the ADV measurements at both streams without the Styrofoam nor the honeycomb, and clearly shows that increasing the flowrate results in a loss of uniformity in the horizontal velocity profile. For **Figure 3-13** to **Figure 3-15**, measurements were made at only one side of the splitter plate, i.e. in a single stream, since it is clear from **Figure 3-12** that when operating the flume with fully opened inlet valves (no induced horizontal shearing) the velocity difference across the width of the flume is small. Furthermore, measurements were made only on the right-side stream for **Figure 3-13** to **Figure 3-15**, as this is the fast stream causing a higher non-uniformity in the velocity profile. In all figures, one can see that as the flowrate increases, the uniformity of the horizontal velocity profile decreases (the average flow rates of the two streams are Q28.3% ~ 18.6 L/s, Q40% ~ 26 L/s and Q50% ~ 32.6 L/s, where the percentage denotes the capacity of the pump). The best results in terms of uniformity of transverse profiles are achieved with the combination of Styrofoam and honeycomb. These results confirm visual observations of the inlet reservoir. The combination of these two flow correction methods allows the control of the undesirable flow features of surface waves and preferential flow paths, which allows for a more uniform streamwise velocity profile at the tip of the splitter plate. The quantification of the uniformity/non-uniformity of the profiles is shown in **Figure 3-13** to **Figure 3-15** and in **Table 3-1** and **Table 5-1**. For example, for a flowrate of Q28.3%, the mean standard deviation of the data without Styrofoam nor honeycomb is equal to 0.40 cm/s for the fast stream, dispersion that is decreased to 0.26 cm/s when using the Styrofoam sheets and the honeycombs. The use of Styrofoam sheets reduces surface waves, which is also important, and therefore, Styrofoam sheets were used in combination with the honeycombs when collection the velocity measurements using 3D-PTV.

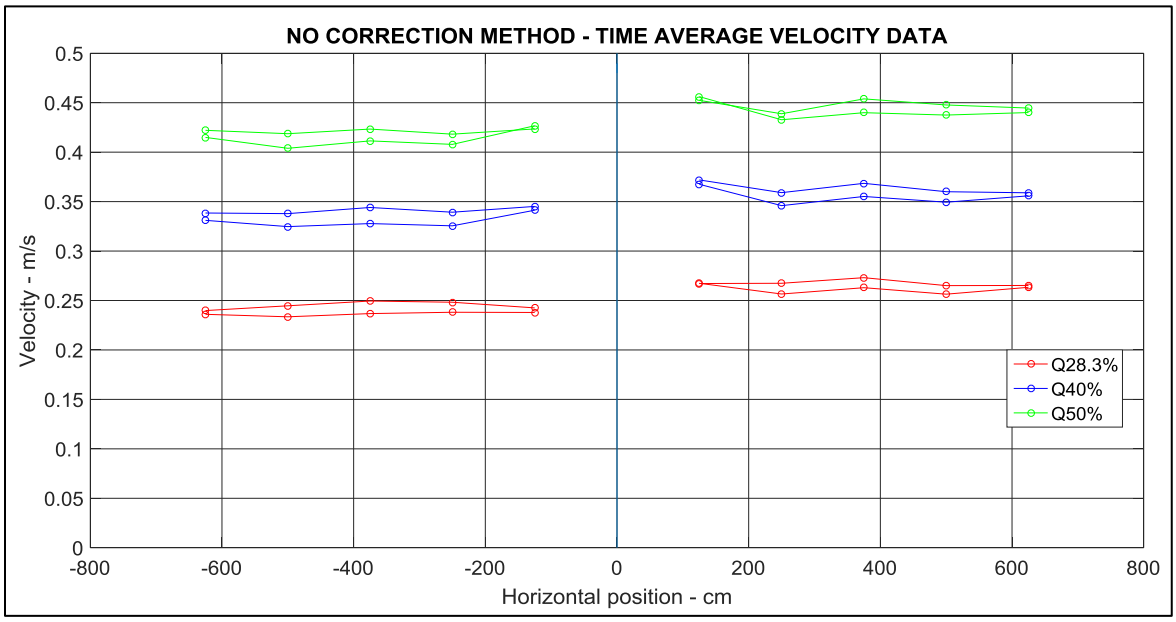

Figure 3-12. Streamwise velocity transverse profile with no correction method Above and below points measurements at 6 cm and 3 cm respectively

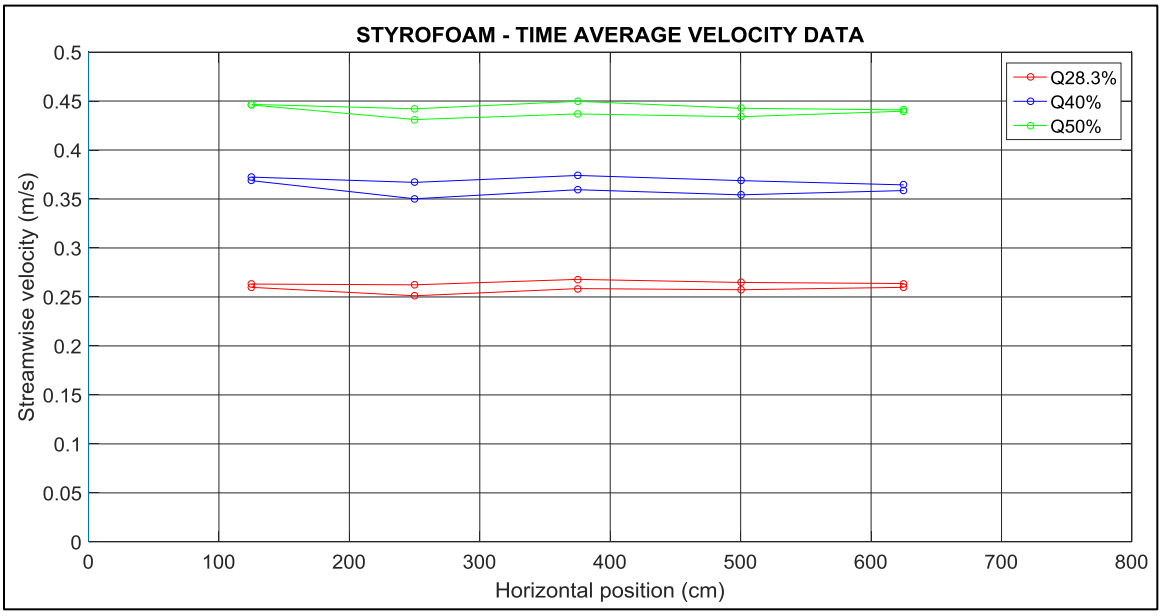

Figure 3-13. Streamwise velocity transverse profile with Styrofoam – right stream Above and below points measurements at 6 cm and 3 cm respectively

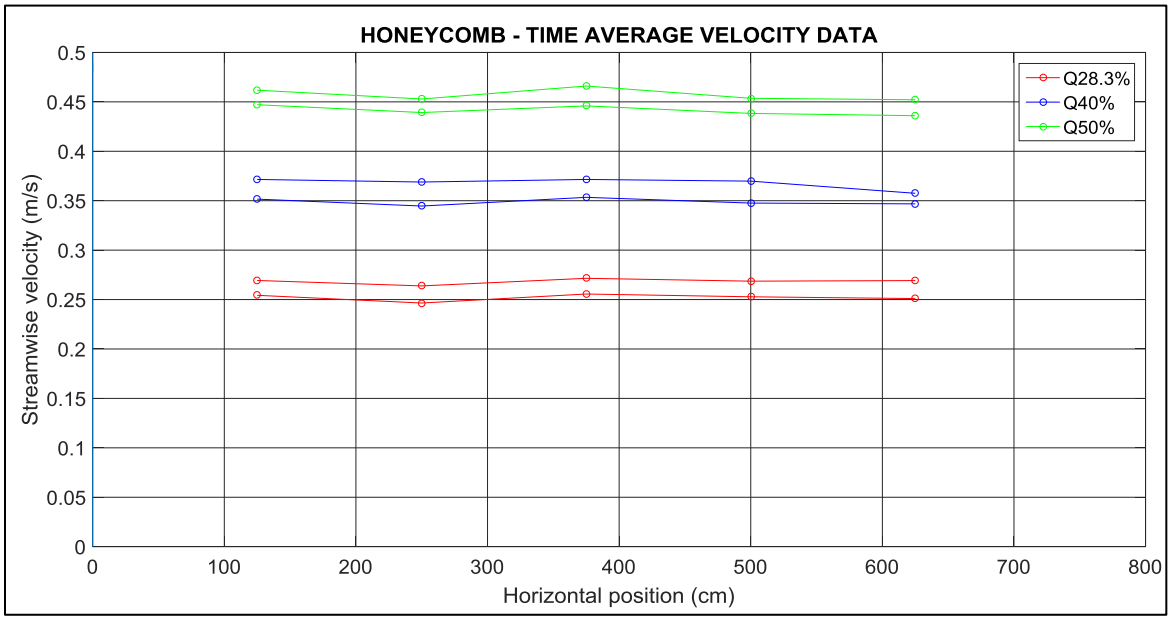

Figure 3-14. Streamwise velocity transverse profile with honeycomb – right stream Above and below points measurements at 6 cm and 3 cm respectively

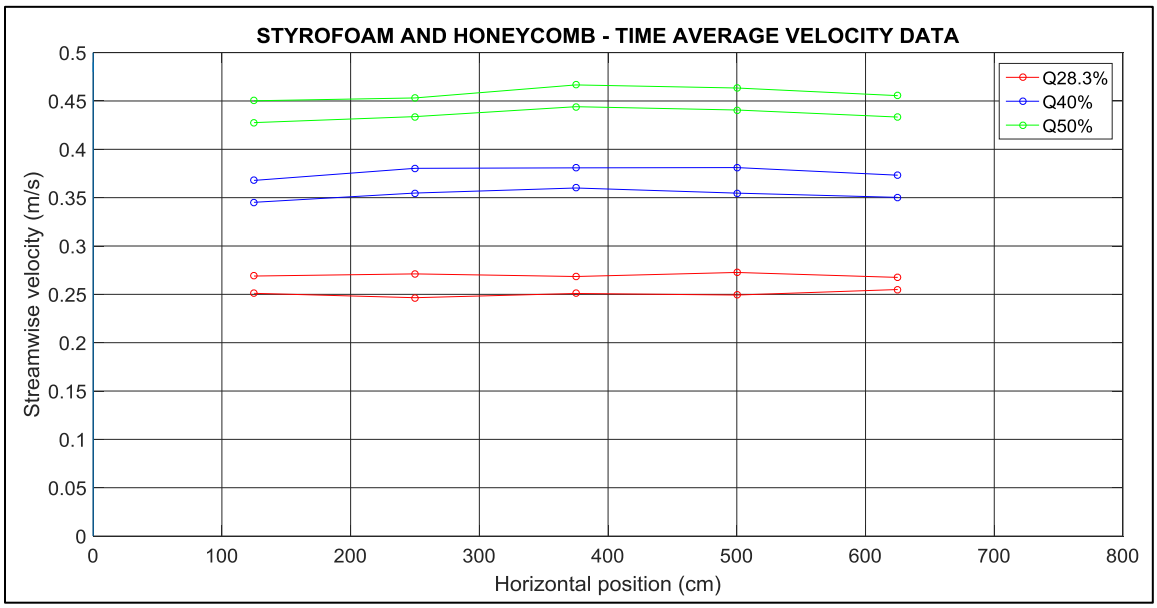

Figure 3-15. Streamwise velocity transverse profile Styrofoam & honeycomb – right stream Above and below points measurements at 6 cm and 3 cm respectively

The ADV streamwise velocity measurements were also used to verify the numerical simulations. The mean flow rate measured by the flow meter described in section 3.1.1 (see **Figure 3-3**), the flow rate computed using the mean cross-sectional velocity calculated from the ADV measurements, and the flow rate obtained from the numerical simulations were compared. **Table 3-2** presents the results obtained for the mean flow rate, and good agreement is obtained between the simulated and the measured results (a maximum difference of approximately 4.5% is obtained in the data), indicating the validity of the numerical simulations presented in **Figure 3-5** to **Figure 3-8**.

Table 3-2. Comparison of results between simulated and measured variables

VARIABLE	RESULTS		
	Measured Flow meter	**Measured ADV**	**Simulated Flow-3D**
Mean flow rate	20.50 L/s	19.83 L/s	20.75 L/s

3.2. Hydraulic conditions

A characteristic of shallow flows is their large width-to-depth ratio (a ratio of ten to a hundred), or the small magnitude of the vertical length scales as compared to the horizontal scales (typically 5% or less). This condition determines the shallowness of the flow defined by the characteristic of i) vertical confinement of the flow resulting in quasi two-dimensional flow features (large-scale turbulent motions), and ii) stabilization of the large-scale motions and streamwise velocities, and the appearance of three-dimensional small-scale turbulent motions (see section 2.1.1.). The flume design imposes constraints on the width-to-depth ratios possible. The minimum possible depth is 6.5 cm, giving a width-to-depth ratio of 23. With this flow depth, the experimental flume is run in a submerged flow condition (i.e. no free overfall into the outlet reservoir), reducing surface waves. In addition, it is the minimum possible depth for the minimum pump flow rate of Q28.3% ~18.6 L/s. It is important to note that the flow depth is flow-dependent, i.e. at higher flow rates, the minimum depth would be deeper, and at lower flow rates, shallower flow conditions could be achieved.

Other important parameters defining the hydraulic conditions are the Reynolds number (Re) and the Froude number (Fr). The Re is defined as the ratio between the inertial and viscous forces:

$$Re = \frac{UH}{\nu} \quad [6]$$

where U is the mean depth-averaged velocity, H is the water depth and ν is the kinematic viscosity of water. The Froude number is the ratio of inertial to gravitational forces:

$$Fr = \frac{U}{\sqrt{gH}} \quad [7]$$

where g is the acceleration of gravity. In natural rivers, the flow is always fully turbulent (Re > 2,000), with very small Froude numbers (except for mountain rivers) of the order of < 0.1. Previous experimental studies for shallow mixing layers have emphasized the importance of keeping the Fr below 0.5 to ensure that the flow is not affected by surface disturbances and is subcritical (Uijttewaal and Booij 2000, van Prooijen and Uijttewaal 2002). The hydraulic conditions presented in **Table 3-3**, were chosen for the experiments. The bed slope of the channel was set to zero as very small slopes are characteristic of low-land rivers. This provides an approximation to uniform flow as the bed resistance is very small, and it was verified by checking the flow depth to a tolerance of ± 1 mm. The flow is maintained by the energy slope provided by an increased depth at the inlet reservoir upstream.

Table 3-3. Experimental hydraulic conditions

Channel stream	Velocity (m/s)	Water depth - H (cm)	Re	Fr	Width-to-depth ratio
1	0.45	6.5	29,250	0.56	23
2	0.31		20,150	0.39	

3.3. 3D Particle Tracking Velocimetry (3D-PTV)

3D-PTV was used to study the shallow mixing layer flow dynamics as it is a nonintrusive velocimetry technique allowing for the determination of trajectories and velocities within a three-dimensional observation volume. In section 2.2, the main hardware components of 3D-PTV were described, i.e. a light source, flow markers or particles, high speed cameras and a calibration process. Once these hardware components are set up, 3D-PTV can be used to study laminar or turbulent flows. The following sections describe each hardware component used for this study.

Moreover, details are given regarding the use of OpenPTV for particle tracking, data acquisition and post-processing.

3.3.1. Flow tracer

An important component of 3D-PTV is the selection of the proper flow tracer in terms of its size, density, and seeding density. A tracer or marker, normally a particle, needs to be small enough to follow the flow motion and not so large that its inertia causes it to lag behind the motion of the flow. However, if too small, a particle will not be seen by the camera or will evoke peak-locking effects due to the particle being smaller than a pixel in the image (Weitbrecht, Kühn et al. 2002). Likewise, as explained in more detail below, particles need to have a suitable seeding density to avoid ambiguities in the tracking process and to resolve the flow field at a small enough scale.

The particle size requirement for imaging is that the minimum particle size is the pixel size, with particles sizes typically in the range of 50 – 100 μm for 3D-PTV experiments (Kim 2015). A study evaluating digital PIV proposed an optimum particle diameter larger than 1.5 pixels and in the range of 1.5 to 3 pixels (Raffel 2007). The pixel size is determined by the camera resolution and by the image size. If a camera views a region of 10 cm by 10 cm and has a pixel resolution of 1 Mp (1000 x 1000 pixels), the size of a single pixel is 0.1 mm. In the present study, an observation region of about 36 cm by 36 cm is captured by three cameras with resolution of 2016 x 2016 pixels, therefore, a pixel represents an area of about 0.18 mm x 0.18 mm. This information is used in the selection of the particle's size. In the current investigation, rice bran wax microspheres (Florabeads RBW) were used. The particles have a specific gravity ~ 1 at 25°C and a natural color that guarantees a good contrast with the black background for image recognition purposes. As Florabeads RBW particles come in a size range of 250 to 600 microns, a sieving process was implemented. Particles were sieved for 3 repetitions of 5 minutes using a stack of sieves of size 600, 425, 355, 300 and 250 microns. This allowed for separation of particles into the ranges of 250 to 355 microns, 355 to 425 microns and > 425 microns. For this study, it was proved from preliminary results that the most suitable range to work with is 355 to 425 microns (about 2 to 2.4 pixels in size).

Regarding the seeding density, it has been shown that particle identification and its position determination in space are only possible if the seeding density, i.e. the number of particles per unit

volume, $\rho_N = N/V$, where N is the number of particles in an observation volume V, is not too high (Malik, Dracos et al. 1993, Dracos 1996). If the number of particles is too high, more than one particle can be found in the analysis search volume increasing the ambiguities in the flow per imaging time step (e.g. overlapping of particles). Also it has been noted that when the number of particles per frame is too high, particle agglomeration can occur due to the cohesion between randomly collated particles rather than due to the effects of velocity field divergence (Nikora, Nokes et al. 2007). On the contrary, if the number of particles is too small, the flow features may not be properly resolved.

A parameter measuring the difficulty of tracking using PTV has been proposed, p, which relates the average particle spacing to the displacement due to the turbulent fluctuations (particle spacing displacement ratio) (Malik, Dracos et al. 1993).

$$p = \frac{\Delta_o}{u'\Delta t} \qquad [8]$$

where Δ_o is the average particle spacing, and $u'\Delta t$ is the mean distance moved by particles during one imaging time step Δt due to the u' rms turbulent velocity fluctuation. If $p \gg 1$, tracking is said to be relatively easy whereas if $p \ll 1$, tracking becomes virtually impossible. Malik et al. (1993) have reported a threshold value of $p > 10$ in order to obtain long particle trajectories as well as the instantaneous flow field structures (Malik, Dracos et al. 1993). One can further relate the number of particles per unit volume, ρ_N, to the average particle spacing, Δ_o,

$$\Delta_o = \frac{1}{{\rho_N}^{1/3}} \qquad [9]$$

from which a particle density can be inferred and hence the number of particles required for an experiment determined. To ensure easy tracking, p > 10, for a hydraulic condition with a mean streamwise velocity of 0.36 m/s, a mean streamwise fluctuations of 0.082 m/s and a frame rate of ~0.0017 s, the particle's displacement due to the velocity fluctuations is estimated to be equal to 0.13 mm, which requires a minimum seeding density of 455 particles/cm^3. Under the current experimental conditions, 400 g of particles were required to conduct an experiment resulting in a density of 1.5 particles/cm^3 (assuming the average particle size of 390 microns). This is confirmed by about 4,000 particles being recognized in each image sequence (see **Figure 3-16**), resulting in a density of the particles of approximately 1.0 particle/cm^3. It was found that a lower number of

particles resulted in portions of the flow being unresolved, while a higher number of particles resulted in particle agglomeration, increase in ambiguities and higher computational times with no significant variation in results.

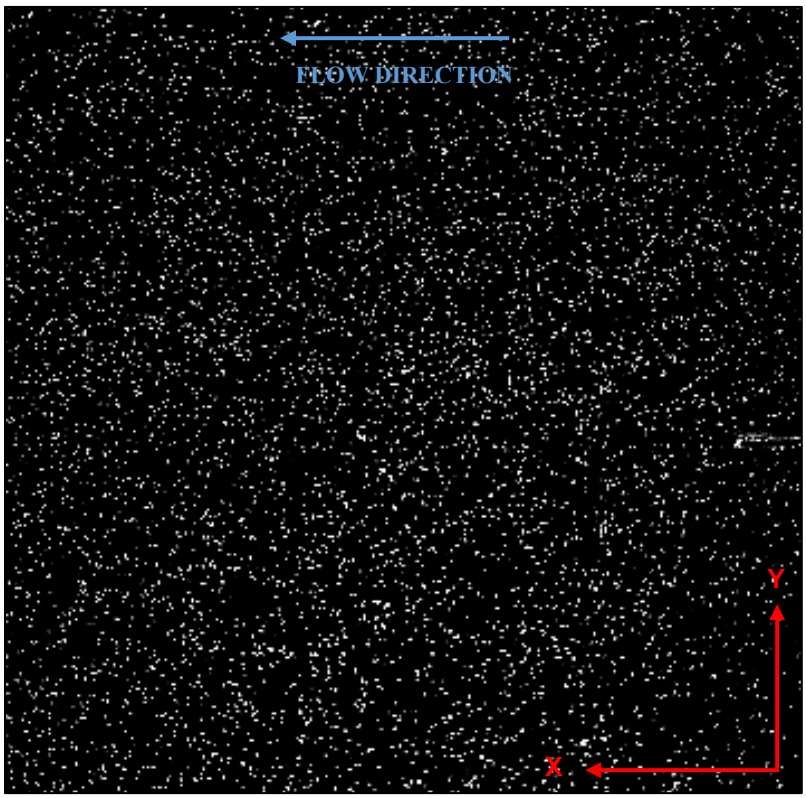

Figure 3-16. Test picture as seen by camera 1 (z-axis pointing out of the page)

When using tracer particles to track the flow movement, it is important to assess whether they follow the flow path. The dimensionless number that determines whether tracer particles follow the flow or not is the called Stokes Number (St), which relates the particles relaxation time or time scale (τ_p) to the Kolmogorov time scale (τ) - see section 3.4.

$$St = \frac{\tau_p}{\tau} \qquad [10]$$

where $\tau_p = \frac{\rho_p \, d^2}{18 \, \rho_f \, \nu}$, with ρ_p being the particle density, d the particle diameter, ρ_f the fluid density and ν the fluid kinematic viscosity. A uniform distribution in the particle size range was assumed and the mean size used to calculate the St.

It is being assumed that if Stokes number is much less than 1, then the particle motion accurately represents the motion of the flow. For the actual experimental conditions, and assuming

the particles specific gravity is 1, a Stokes number equal to 0.78 was obtained. It is therefore reasonable to assume that the current particles do follow the flow motion and therefore can be used as flow tracers. Note that the Stokes number is expected to decrease as the flow develops (as the mixing layer width eventually grows) with downstream distance, since the Stokes number is inversely proportional to the integral length scale of the flow (l) or the mixing layer width (δ), see section 3.4.

For the selection of appropriate particles, the following criteria were considered in addition to the considerations mentioned above: size range, density, price, sphericity, and contrast/color. A difficulty in applying 3D-PTV for the current experimental setup (see section 3.1.1) was the choice of a tracer, mainly due to the high number of particles required. More suitable particles could have been used in this study, for instance white Polyethylene Microspheres from Cospheric LLC. These microbeads are neutrally buoyant, with an almost perfect spherical distribution (> 90%) and a size range of 212 – 250 μm, however the cost is very high (100 USD per 10 g). In the current investigation, rice bran wax microspheres (Florabeads RBW) were used, with specific gravity ~ 1 at 25°C, natural color, and a size range of 355 to 425 μm. In the current setup, a filter was built to recover particles and it had an average efficiency of 70%, implying that 30% of the particles used per experiment are lost. **Table 3-4** presents a non-exhaustive list of potential flow tracers considered and some remarks on why these were not used in the current study.

Table 3-4. Considered potential flow tracers

COMPANY	PARTICLES	REMARKS
Cospheric LLC	White Polyethylene Microspheres	Their price is too high (100 USD per 10 g) for the required number of particles per experiment (> 400 g).
Eastechem Inc	Cenosphere CS50	Color not uniform so good contrast not obtained. Also, particles are positively buoyant.
Polysciences	Polysciences 200 – 300 μm Polybeads 90 μm	Prices too high (180 USD per gram) and diameters too small for particle recognition.
Zeeospheres	Ceramic Microspheres	Particles range too small and negatively buoyant.
Novum Glass LLC	Microspheres T-Series	Good uniformity and roundness, however the specific gravity is 2.5.

Table 3-4. Considered potential flow tracers

COMPANY	PARTICLES	REMARKS
Microtek laboratories Inc.	-	Mean particle size around 85 μm, too small, and specific gravity too small (~0.9).
Spherotec	Polystyrene Particles, Crosslinked, Research Grade, 5% w/v, 225 μm, 10 mL	Their price is too high (4,000 USD per 100 g) for the required number of particles per experiment (> 400 g).
Akzonobel	Microsphere in NA 80 μm	Size and density too small (15 kg/m^3 or 30 kg/m^3).
Polymicrospheres	Microspheres in different ranges: 100 - 260 μm 125 – 210 μm 210 – 250 μm 250 – 300 μm	Even if almost neutrally buoyant particles, density around 1.03 to 1.05 g/cm^3, their price is too high (on average 100 USD per gram). Good size distribution.
Sphereone	Extendospheres HBG	Good size distribution but positively buoyant (density of 0.70 g/cm^3).

3.3.2. Cameras set-up and illumination

In the current study, three cameras were used to reduce the number of ambiguities that can arise in the use of 3D-PTV. As shown by Mass et al. (1993), a two-camera system is unable to resolve the correspondence problem because more than one particle may be on the epipolar line for the particle identified in the first image (reduction of ambiguities)[1], thus a three-camera system is chosen to reduce ambiguities in the particle detection process. The three cameras were positioned in such way that an approximate equilateral triangle distribution was achieved, an arrangement that further reduces the ambiguity problem in particle detection (Maas, Gruen et al. 1993).

High-resolution (2016 x 2016 pixels) CCD cameras were used to capture the image sequence in the observation volume. The cameras are pco.dimax CMOS high-speed cameras with an approximate memory capacity of 3.7 GB (limiting the number of images recorded), which were wired together in a daisy chain connection with one camera being the master and the other two

[1] For example, with 2,000 particles detected in an observation volume of depth 40 mm and with a tolerance width of the epipolar line equal to 10 microns, the number of ambiguities for a two-camera system is 1605 whereas a three-camera system in a perfect equilateral triangle is 140, more than a tenth-fold difference.

being the slaves. The cameras parameters used a frame rate of 600 Hz and a sensor size or Region of Interest (ROI) of 2016 x 2016, allowing for the recording of 6,298 images in a recording time of 10.5 seconds.

A set of halogen lamps (8 light balls, 4 of 500 W and 4 of 300 W) were used to illuminate the flow from the side of the flume. To increase the image quality (by increasing the contrast between the particles and the flow) of the recorded observation volume and to assure that light could only come through designated regions, a black plastic sheet was used to cover the top of the observation volume and black adhesive paper covered the flume sides (light was forced to enter just above the water surface – see **Figure 3-17**).

Figure 3-17. Side illumination

Likewise, to ensure that the light intensity was controlled along the length of the flume and that no ambient particles (dust) interfered with the tests, black tarpaulins were used to cover the top and sides of the flume along its entire length.

3.3.3. Calibration process

Calibration is a crucial step for 3D-PTV. By means of the calibration, the camera's view is correlated to the real space coordinates that are being imaged and the different camera parameters required to run OpenPTV are defined. The quality of the calibration determines the accuracy with which the particles position is observed. Normally the calibration object is a three-dimensional target-block or block, in which points with known coordinates are located over the range of x, y and z positions of the imaging volume. These points' coordinates are then used in the 3D-PTV

analysis to reconstruct the 3D positions of the detected particles in each recorded frame or in each imaging time step (Lüthi 2002, Kim 2015, Akutina 2016).

The calibration object designed, built, and used in this investigation is shown in **Figure 3-18**. The dimensions of the target object are 300 mm x 300 mm x 70 mm in the x, y, and z axes, respectively. The diameter of the target points is 0.5 mm, and the distances between points are 12.5 mm x 15 mm x 10 mm in the x, y, and z directions, respectively, except for the top-edge steps that have a distance to their adjacent points of 9.4 mm x 15 mm x 15 mm in the x, y, and z directions, respectively. The calibration object was designed to cover the observation volume (x, y and z directions); therefore, a stepped object was designed. The calibration object was machined from black Delrin with 5 mm deep holes (475 in total) that were filled with white silicone after drilling (5 dots were left without silicone – see section 4.1).

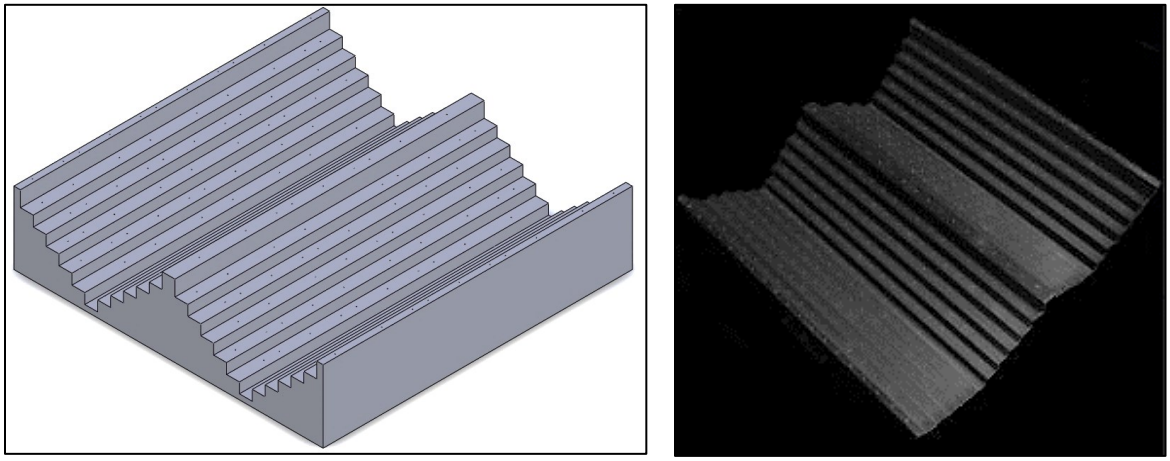

Figure 3-18. Calibration object (left design; right machined)

Once built, the calibration object was placed inside the region of interest where the shallow mixing layer develops and photographed by each of the three cameras. The flume was filled with stagnant water to a depth of 6.5 cm. In the calibration process, the different camera parameters were defined and then later applied to the tracking procedure using OpenPTV.

The calibration object was built with a tolerance of 0.0002”. As the Delrin tends to bend when cut and drilled (due to tension and compression effects), a straightener mechanism was used to ensure the precision of the location of the 475 holes. The mean bias between the designed and real coordinates in the horizontal plane and in the vertical plane is approximately 0.3 mm. To

ensure precise placement of the calibration object exactly at the midplane of the flume at the end of the splitter plate, a small location guide with a 3 mm slot was used.

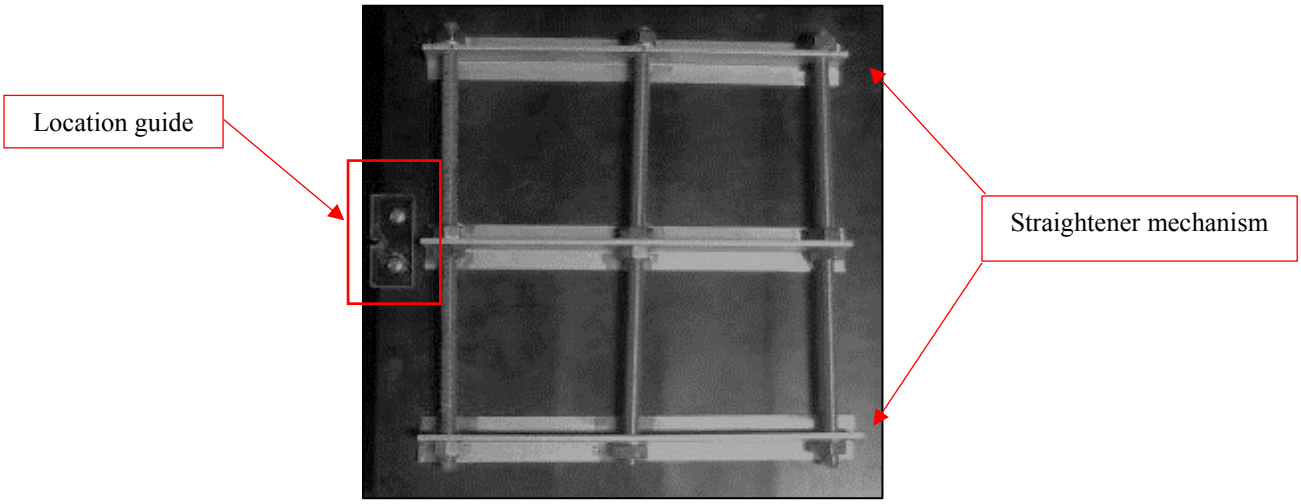

Figure 3-19. Straightener mechanism and location guide

3.3.4. Data acquisition

To acquire the image sequences necessary for 3D-PTV measurements, high-speed cameras (pco.dimax, section 3.3.2) were used. At the specified frame rate, 600 Hz, a maximum of 6,298 images were recorded and stored in the camera's memory, the number being limited by the camera's storage capacity (~ 3.7 GB). Once the images were recorded, they were locally saved to the computers operating the camera's software, CamWare, and then transferred to an external drive for analysis using OpenPTV.

3.3.5. OpenPTV

In this thesis, the 3D-PTV analysis of the image sequences is accomplished using OpenPTV, a free and open-source software released to the public in 2012. This software is based on the core algorithms developed at ETH Zurich and has been further developed by the TU/e group of Turbulence and Vortex Dynamics and by the Turbulence Structure Laboratory at Tel Aviv University (Consortium 2014).

By using OpenPTV, first the particles' coordinates in each image sequence, by detecting the center of the particles with sub-pixel accuracy, were calculated. The coordinates of the particles in three-dimensions were then determined from the correspondences, using the method of epipolar

lines, between particle positions (the calculated coordinates) seen from the three cameras having different viewing angles. Lastly, particle trajectories are obtained by tracking in the whole domain for the full image sequence making use of the bundle model mentioned in section 2.2.

3.3.6. Experimental set-up

Figure 3-20 depicts the experimental setup used to study shallow mixing layers by means of 3D-PTV. Three high-speed cameras were located under the recirculating flume capturing the observation volume from different angles. A rail system was built to position the cameras along the flume locating them under the desired observation volume, which allows for viewing along the length of the flume. Illumination was achieved from the side of the flume, and a black sheet was used to cover the top of the observation volume and to increase the image quality (contrast).

3.3.7. Data post-processing

OpenPTV can detect and track particles in different imaging frames giving spatial information on the particle's position. To compute the three-dimensional velocity field information, the code written by Lüthi was employed (Consortium 2015). This code fits a trajectory to the particles position using a moving cubic polynomial. From the fitting procedure, filtered positions (filtered using a low-pass filter to improve the accuracy of velocities determination) and velocities are assigned to each particle being tracked (Luthi, Tsinober et al. 2005).

Filtered positions, $\widehat{x_i}(t)$ along each trajectory can be low-pass filtered to derive filtered first and second order derivatives, $\widehat{u_i}(t)$ and $\widehat{a_i}(t)$ (Luthi, Tsinober et al. 2005). The filter implemented is a moving cubic spline,

$$\widehat{x_i}(t) = c_{i,o} + c_{i,1}t + c_{i,2}t^2 + c_{i,3}t^3 \quad [11]$$

From the filtered position, filtered velocities and accelerations are defined as,

$$\widehat{u_i}(t) = c_{i,1} + 2c_{i,2}t + 3c_{i,3}t^2 \quad [12]$$

and

$$\widehat{a_i}(t) = 2c_{i,2} + 6c_{i,3}t \quad [13]$$

From the filtered velocities, $\widehat{u_\iota}(t)$, spatial and temporal velocities can be interpolated for every particle trajectory point assuming that the velocity field around a position x_o behaves linearly (Luthi, Tsinober et al. 2005). The estimated solution for the velocity field becomes (for $i = 1,2,3$),

$$\widehat{u_\iota}(x_o) = c_{i,o} + c_{i,1}x_1 + c_{i,2}x_2 + c_{i,3}x_3 \quad [14]$$

with

$$c_{i,1} = \frac{\partial u_i}{\partial x_1}, \quad c_{i,2} = \frac{\partial u_i}{\partial x_2}, \quad c_{i,3} = \frac{\partial u_i}{\partial x_3} \quad [15]$$

At least four points (n) with information are required. Furthermore, given that all points remain close enough, a higher number of points gives a higher accuracy in the form of $\sim n^{-1/2}$. Similarly, temporal velocity derivatives are obtained as follows (Luthi, Tsinober et al. 2005),

$$\widehat{u_\iota}(x_o) = c_{i,o} + c_{i,1}x_1 + c_{i,2}x_2 + c_{i,3}x_3 + c_{i,4}t \quad [16]$$

Once the information from OpenPTV was acquired and the code by Lüthi used to calculate the three-dimensional velocity field information, all data were analyzed using Matlab to produce the results presented in Chapter 0.

3.4. Flow scales

Turbulent flows exhibit turbulent motions over a broad range of scales. The largest scales in the flow are referred to as the time scale and the integral length scale, the latter being defined by the physical dimensions of the flow (normally the pipe diameter or the flow depth). These scales characterize the largest eddies of the flow. The smallest scales in turbulent flows haven been referred as Kolmogorov microscales, scales at which viscous effects are important and dissipation takes place (Shen 2002). Eddies in the range of the integral length scale lose energy at a rate equal to,

$$\varepsilon \propto \frac{\tilde{u}^3}{l} \quad [17]$$

where l is the integral length scale and $\tilde{u}$ is the flow u_{rms}.

Combining the dissipation rate and the flow kinematic viscosity, the Kolmogorov microscale (η) and the time scale of the smallest eddies (τ) can be defined,

$$\eta \propto \left(\frac{\nu^3}{\varepsilon}\right)^{1/4} \quad [18]$$

$$\tau \propto \left(\frac{\nu}{\varepsilon}\right)^{1/2} \quad [19]$$

where ν is the kinematic viscosity.

In the current research, the average u_{rms} is equal to 0.082 m/s, for a water depth of 0.065 m, which gives a dissipation rate of 0.0085 m^2/s^3, at which eddies of the size of the mixing layer width lose their energy to the smallest eddies. These experimental conditions indicate that the smallest scales of the flow of 0.11 mm and 0.011 s are fairly resolved by the current experimental conditions (particles average displacement due to the streamwise velocity fluctuations equal to 0.13 mm and acquisition frame rate ~0.0017 s).

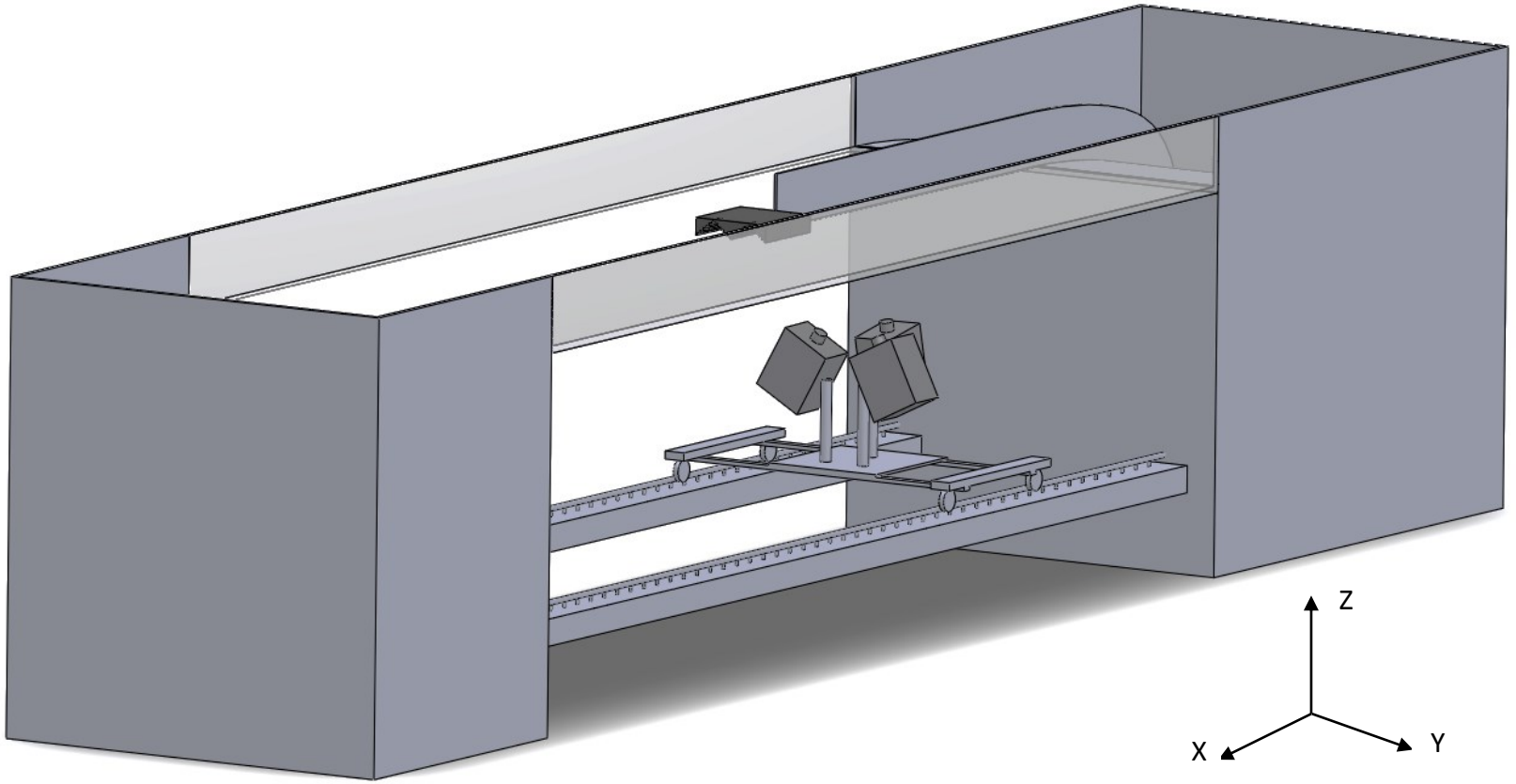

Figure 3-20. 3D schematic representation of the flume setup

4. RESULTS AND DISCUSSION

This chapter presents the findings of this research using 3D-PTV to study the near-field of a shallow mixing layer between parallel coflowing streams. The quality of the calibration, which is the main criteria used to evaluate the particles detection accuracy, is discussed. The result of applying 3D-PTV to generate flow trajectories is presented. The flow is analyzed and validated using velocity time-series and transverse profiles for mean streamwise velocity and turbulent intensity. The effect of the splitter plate used to produce the confluence is examined and explained. Furthermore, the shear layer width is analyzed, and attention is given to the displacement exhibited by the shear layer centerline. Lastly, instantaneous velocity contour plots for the y-z plane are generated to identify how mixing occurs in the near-field of the mixing layer at different downstream positions.

4.1. Calibration

As mentioned in the previous chapter, 3D-PTV calibration was achieved by means of a solid calibration object (see section 2.2 and section 3.3.3). As a check on the calibration object recognition, 5 out of 475 dots were removed to clearly identify the orientation of the object. **Figure 4-1** depicts the location of 470 dots in a calibration image taken almost perpendicularly to the x-y plane of the object from below the flume, while **Figure 4-2** shows the detection of the dots on the calibration object with their corresponding ID.

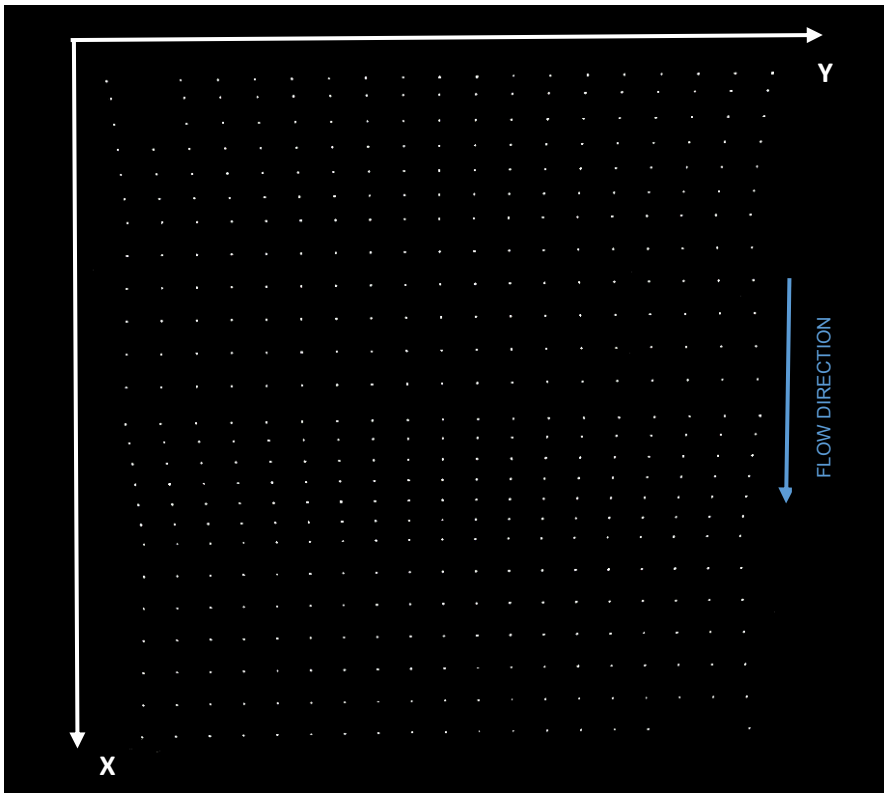

Figure 4-1. Calibration picture as seen by camera 2 (z-axis pointing out of the page)

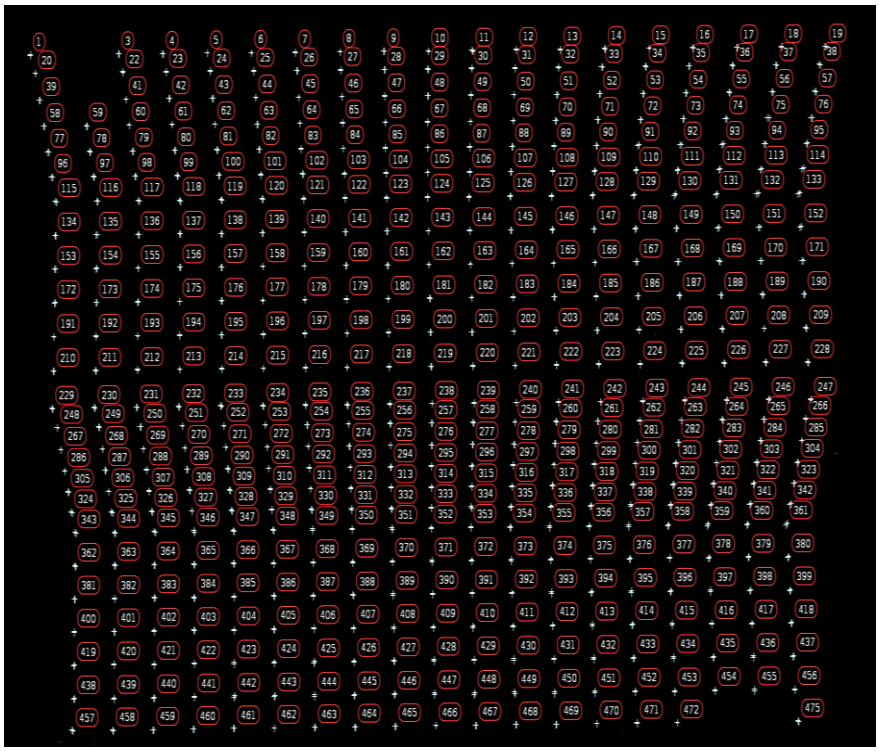

Figure 4-2. Calibration picture with dots ID assigned in stagnant water

An estimation of the calibration error was obtained from an experiment in stagnant water, in which calibration pictures were taken and the positions of all dots calculated using 3D-PTV. **Figure 4-3** shows a graphical comparison of the calibration results, in which the position matches between the true values and the calculated values are good, with a root mean squared error of 0.17 mm, 0.14 mm and 0.33 mm in the x, y, and z axes respectively. This shows that the current 3D-PTV system can resolve flow scales close to the Kolmogorov length scale estimated to be 0.11 mm due to subpixel accuracy (possible by using particles greater than 1 pixel in size), indicating the space for improvements in the current velocimetry technique.

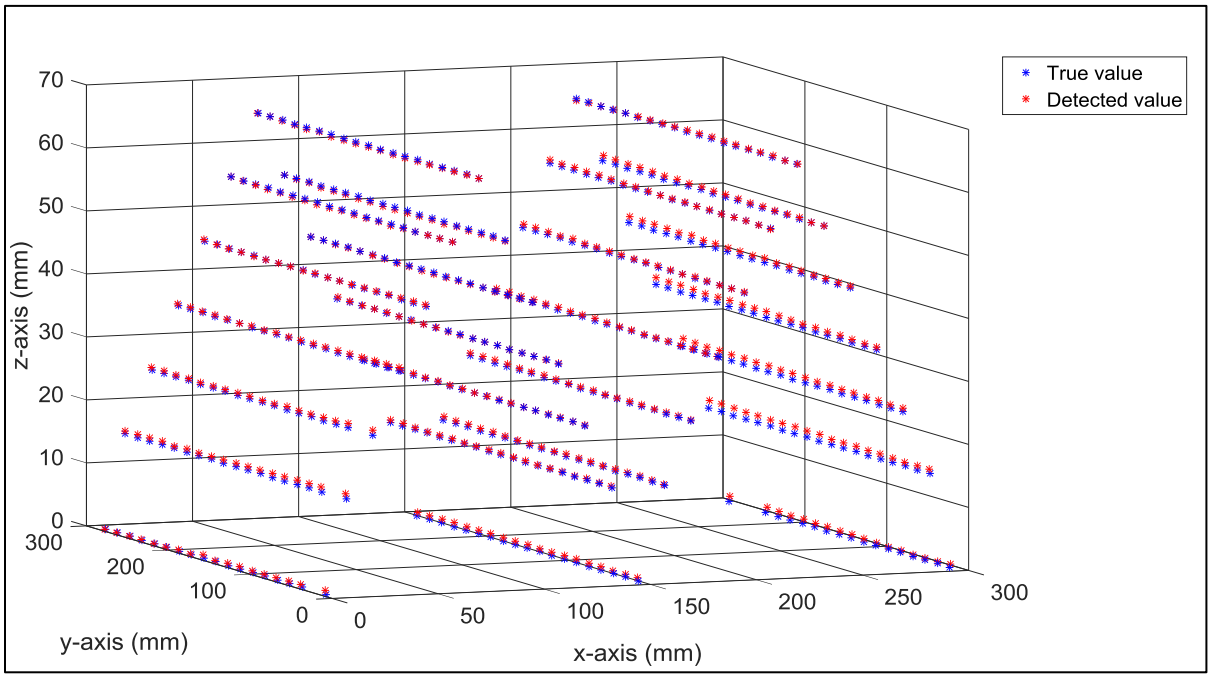

Figure 4-3. Isometric view of calibration results

A bias error was calculated by comparing the true to the calculated positions of the dots. Probability histograms for the bias error were plotted to obtain the probability distribution of the error in each spatial dimension. **Figure 4-4** shows that the error distribution in all planes behaves similarly, with the highest error probability near the zero bias.

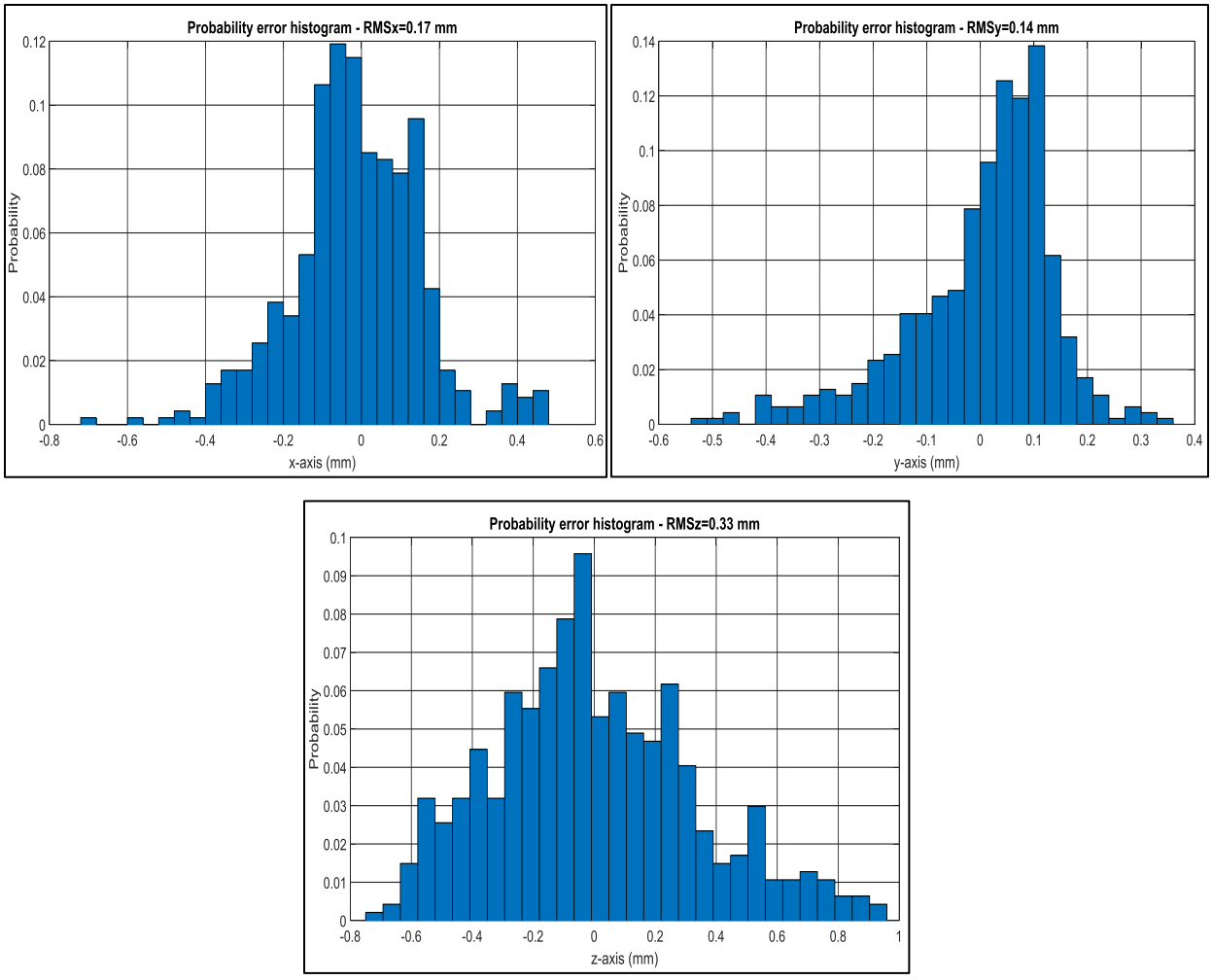

Figure 4-4. Probability error histograms

4.2. Trajectories

All trajectories and 1000 of the trajectories identified (over 10.5 s) in the observation volume (30 x 30 x 6.5 cm) downstream of the splitter plate are presented in **Figure 4-5** and **Figure 4-6**, respectively. The isometric views depict the main qualitative result and advantage of applying 3D-PTV as compared to other velocimetry techniques like hot-film anemometry or ADV, i.e. the acquisition of trajectories or Lagrangian information. In **Figure 4-5** and **Figure 4-6** some characteristics of turbulent flows can be identified (Tennekes and Lumley 1972). Irregular motion of particles in 3-D space (randomness of the flow), with particles moving over a wide range of length scales. The particles' movement helps visualize the diffusivity of turbulent flows, which causes rapid mixing and increased rates of momentum and mass transfer. Overall, it can be said that the flow is fluctuating, agitated and disordered, corresponding to a turbulent flow (LI 2017).

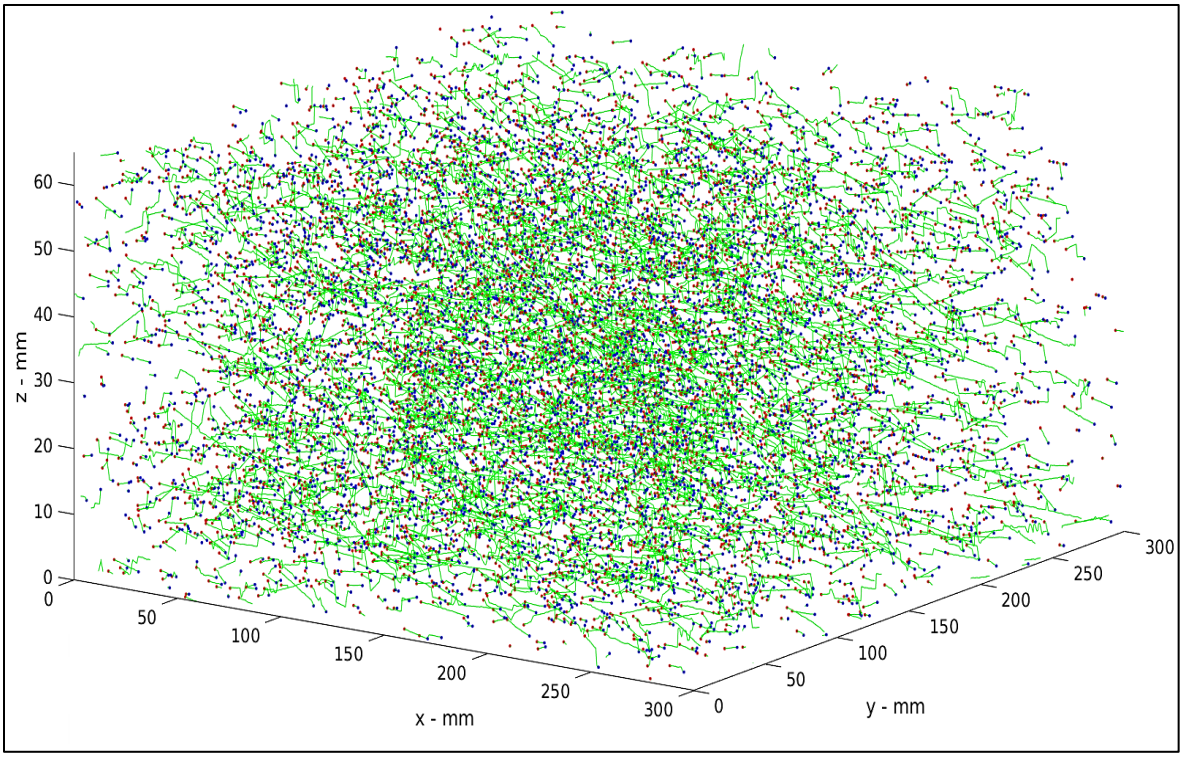

Figure 4-5. Isometric view of all trajectories segments (1'450,000) identified (red dots starting point; blue dots ending point)

Each trajectory can be followed for up to 197 image sequences and on average for 13 images, with a standard deviation of the trajectory length of 11 images, which roughly represents a maximum displacement per trajectory of 3 cm, considering the particles average displacement due to the velocity fluctuations. Particle trajectories are not followed over the full 6,298 images due to difficulty in tracking the particles from one image to the next one. This can be due to ambiguity (i.e. more than one particle on the epipolar lines in the next image) or changing light conditions (intensity) during experiments resulting in particles not being identified. In **Figure 4-6** a total of 1,000 trajectories are displayed to better observe individual trajectories. For the current experimental conditions, around 4,000 particles are being identified in each image sequence, from which about 3,000 links are being established in 3D space per each frame pair (particles correspondences), and the corresponded particles can then be tracked resulting in approximately 1'450,000 trajectories for the 6,298 images being analyzed (see **Figure 4-5**).

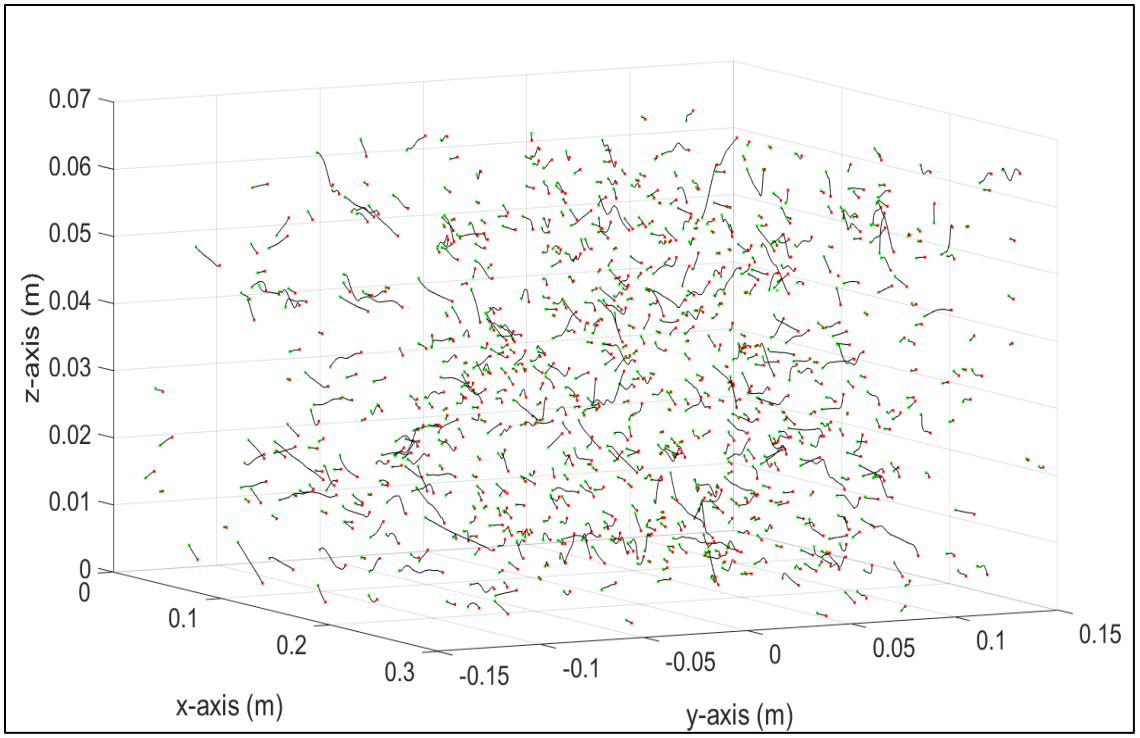

Figure 4-6. Isometric view of a fraction of trajectory segments been identified (green dots starting point; red dots ending point)

4.3. Flow validation

The velocity measurements were validated first by checking for overall consistency and convergence of the data with time by analyzing the average velocity of the whole domain (30 x 30 x 6.5 cm), and secondly by checking for convergence of the data at specific domain locations representative of the analysis (depth-averaged velocity from a point on a transverse profile and a depth-averaged turbulent intensity from a point on a transverse profile).

The following reference frame is used in the analysis of the data presented below and in the following sections (see **Figure 4-7**).

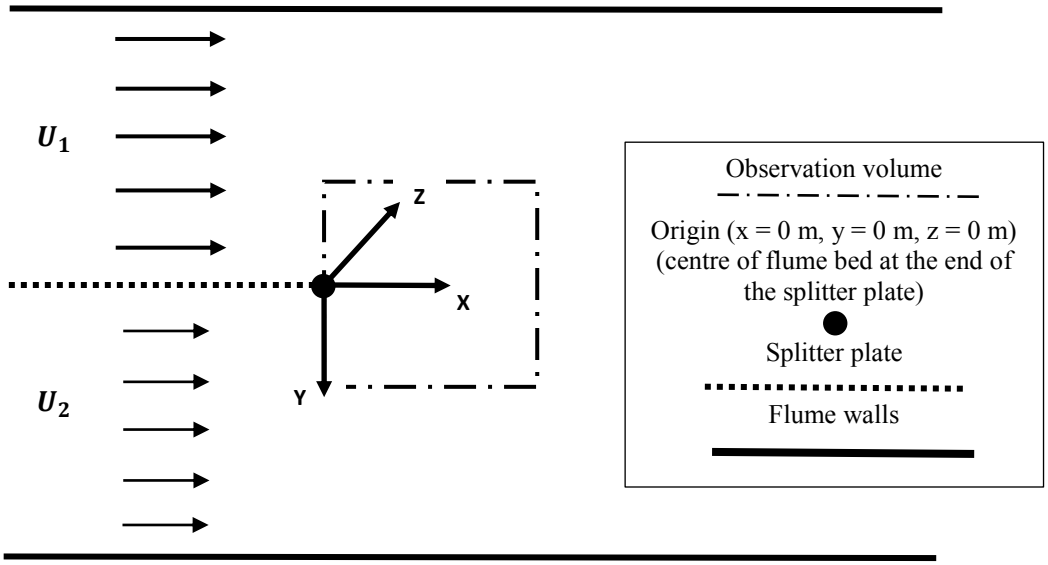

Figure 4-7. Reference frame

The overall consistency of the velocity data was verified using time series plots where the velocity fluctuations can be observed for the domain averaged u, v, and w velocity components, and by calculating a cumulative root mean square deviation for the domain average velocity component time-series. **Figure 4-8** depicts the time-series of the domain averaged velocity components. The time average (of the 10.5 s of data) of the domain averaged velocity components u, v, and z are 0.36 m/s ,0.0016 m/s, 0 m/s, respectively, with fluctuations around the mean of O(0.01 m/s). (Note that v and z are essentially 0 m/s as expected).

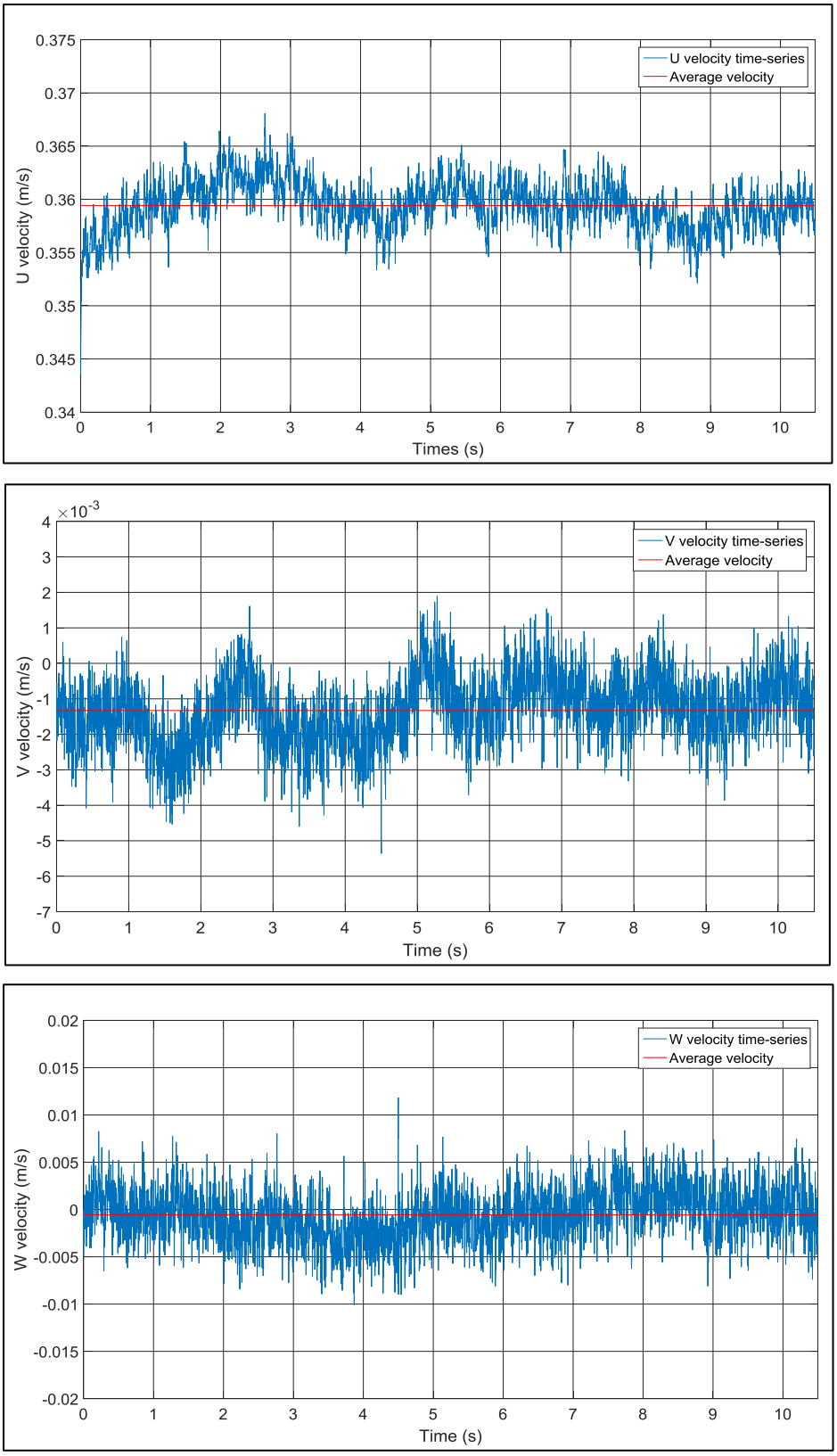

Figure 4-8. Time-series plots for u, v, and w domain averaged velocity components

Convergence of the domain averaged velocity components was checked by assessing whether their cumulative root mean square deviation ($RMSD$) approaches zero, with $RMSD$ being defined as,

$$RMSD_j = \sqrt{\frac{\sum_{i=1}^{n}(x_i - \bar{x})^2}{n-1}} \quad [20]$$

where n is the window size, j is the current window, x_i is the ith value of the window, $\bar{x}$ is the mean value in the current window, and x represents the u, v, and w velocity components.

The RMSD of the domain average velocity components are shown in **Figure 4-9**, showing that as the time-series approaches convergence the root mean square deviation value approaches zero, with data being captured at 600 Hz. The RMSD approaches a constant value of O(10^{-5} m/s) for the u, v and w components, which is equivalent to about 0.3% of the u component, after 6 s.

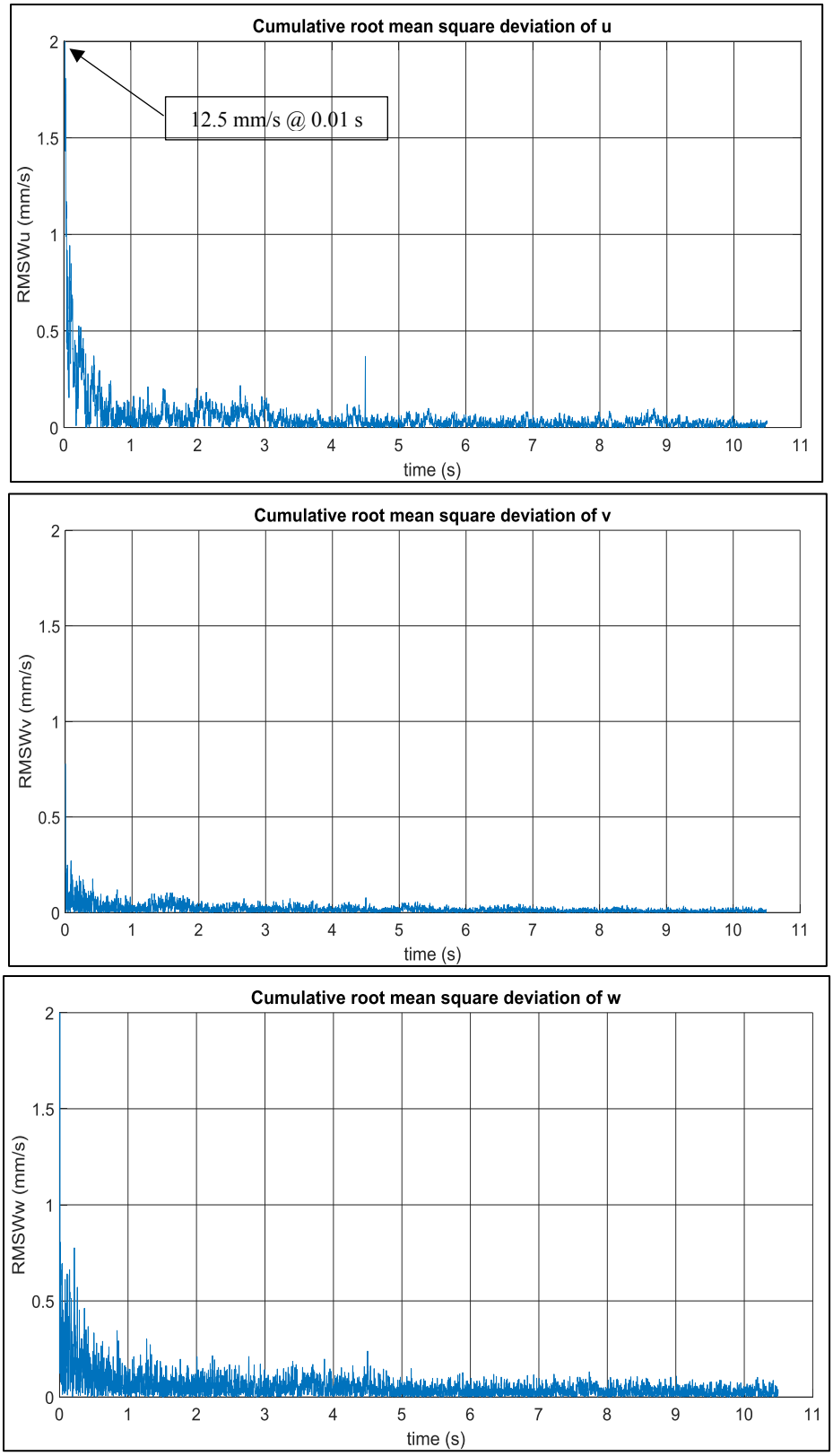

Figure 4-9. Convergence of the domain averaged velocity components u, v and w shown by using RMSD

As mentioned, convergence of the data at specific domain locations representative of the analysis (depth-averaged velocity from a point on a transverse profile and a depth-averaged turbulent intensity from a point on a transverse profile) were analyzed. In **Figure 4-10** the location of the measurements for data convergence analysis is presented, where the mixing layer center and the fast and the slow free-stream velocity are defined.

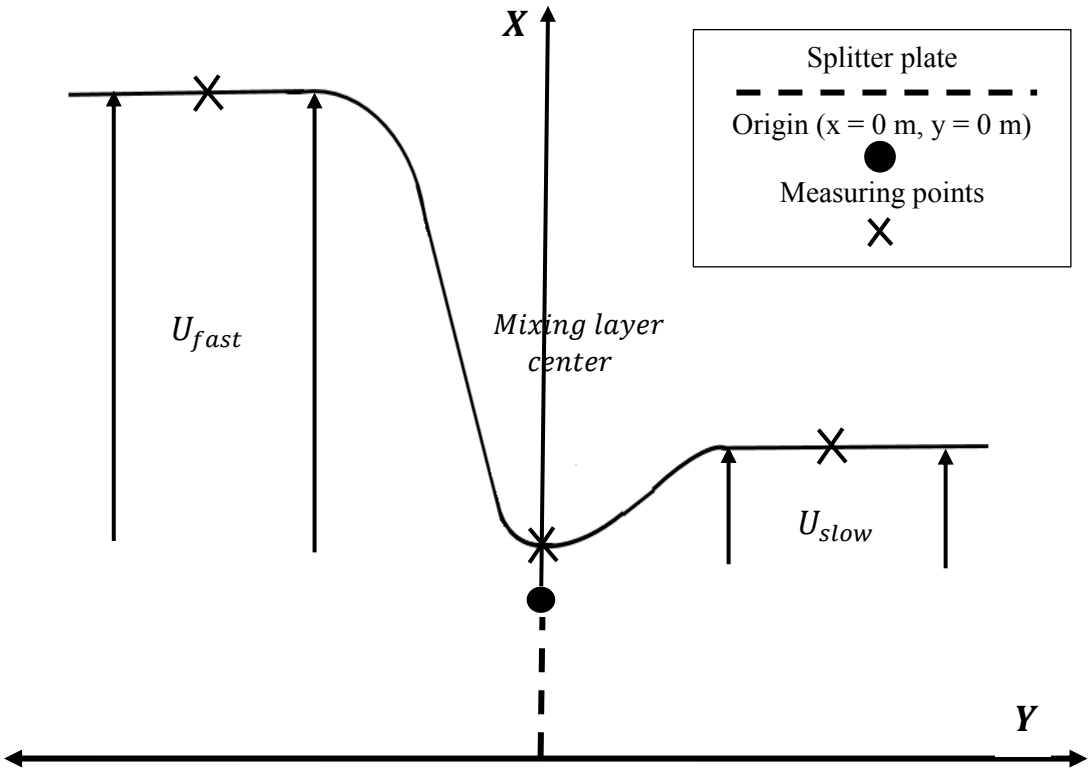

Figure 4-10. Convergence measurement locations

The depth-averaged velocity for the u component at a downstream location of x = 0.15 m at three points in the transverse direction of y = -0.10 m, 0 m and 0.10 m corresponding to the fast velocity free-stream, the center of the mixing layer and the slow velocity free-stream, respectively, were used to further assess the data convergence. Plots for the cumulative averaged values of the u velocity component are presented in **Figure 4-11**, where all data start to attain a less fluctuating behavior past 3 s of data collection at 600 Hz, to attain a stable value past 6 s, although they drift by up to 1%.

The convergence of the turbulent intensity data was checked at one downstream location of x = 0.15 m for three points in the transverse direction of y = -0.10 m , 0 m and 0.10 m, which correspond to the turbulent intensity for the fast velocity free-stream, the center of the mixing layer

and the slow velocity free-stream, respectively. Plots for the cumulative turbulent intensity averaged values are shown in **Figure 4-12**. From these plots it can be inferred that the turbulent intensity in all cases becomes stable after 3 s of data collection, with higher fluctuations from 0 to 1.5 s reducing by 1.5 s and approaching to a plateau at a stable value.

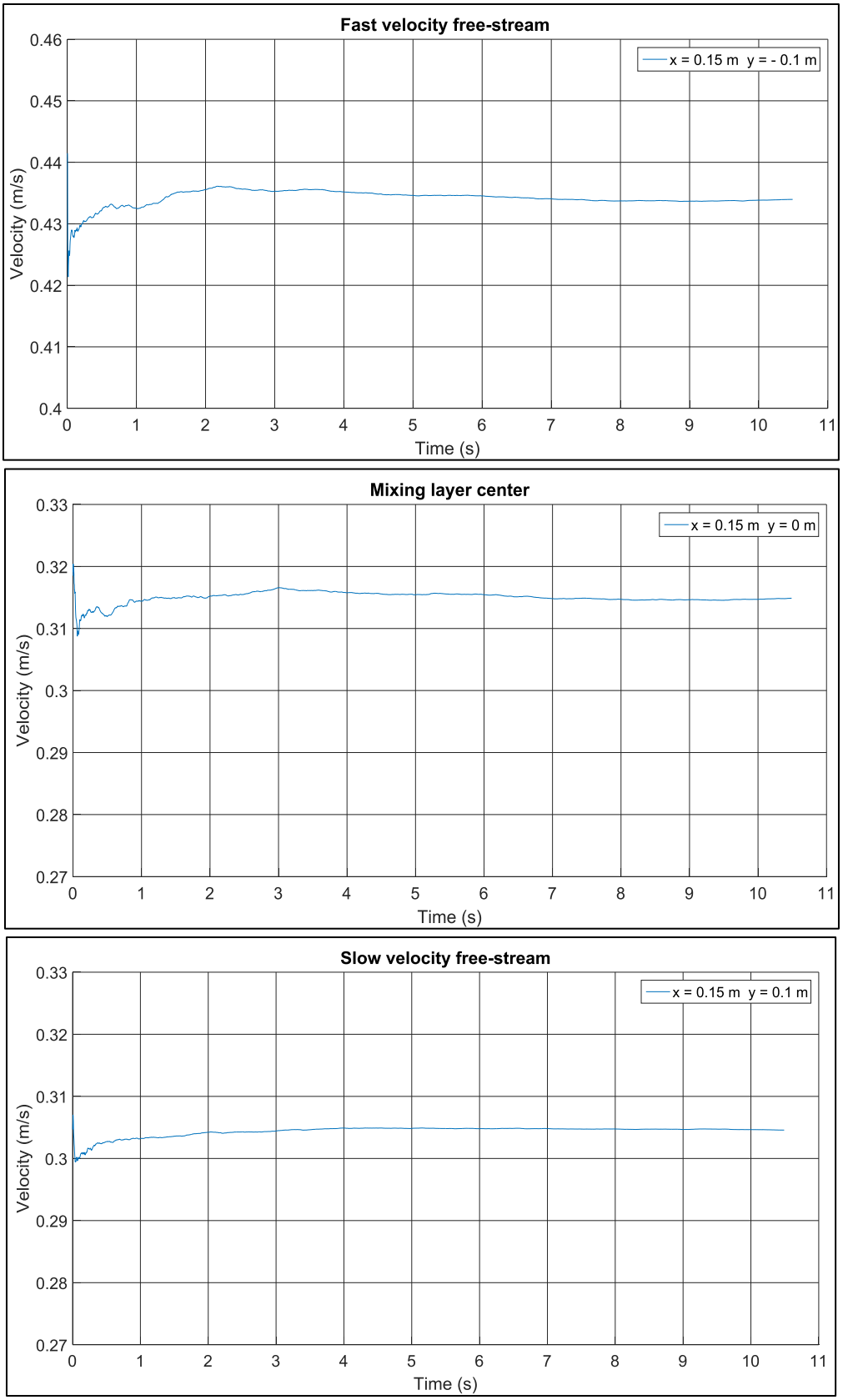

Figure 4-11. Convergence of the depth-averaged u velocity for a transverse profile

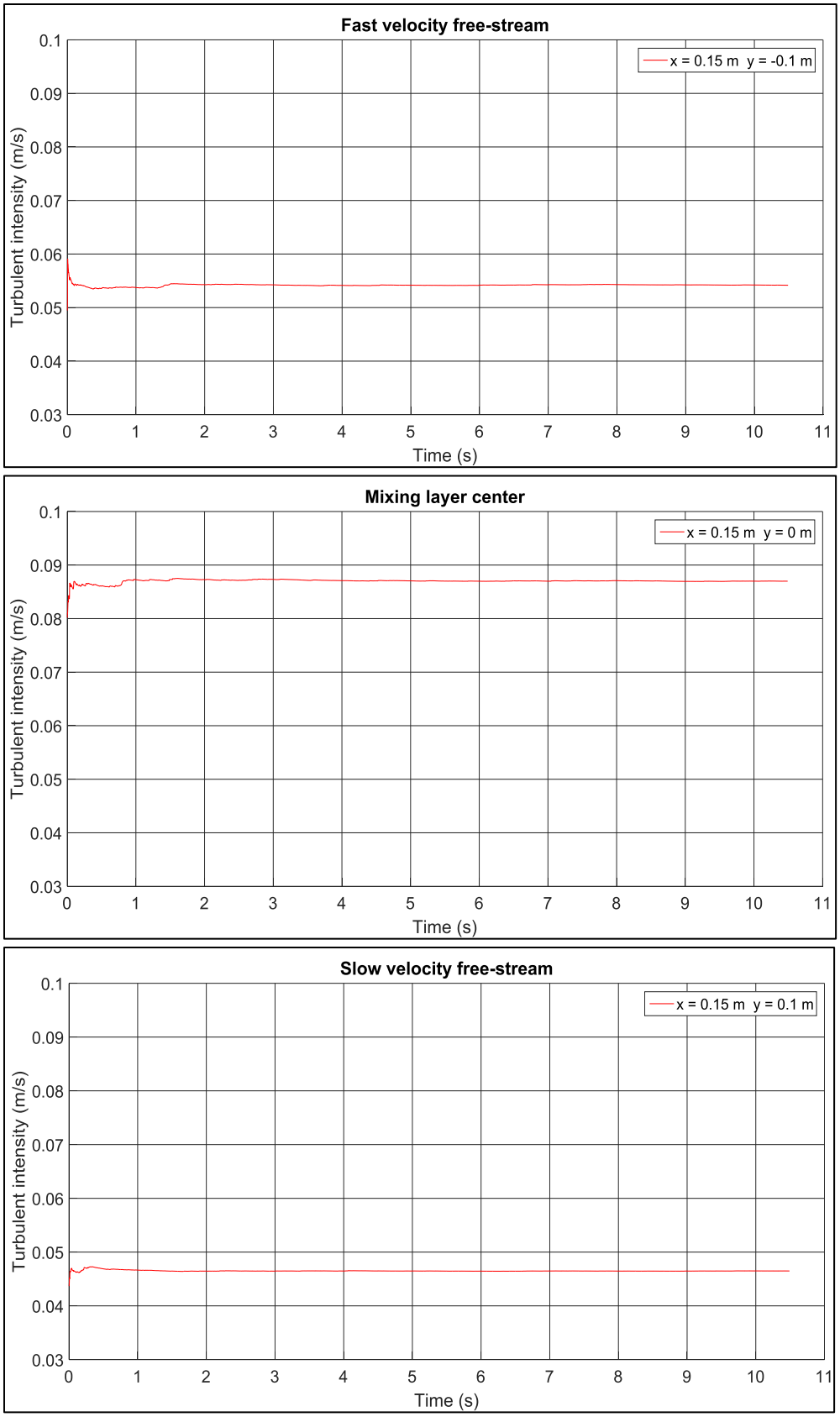

Figure 4-12. Convergence of the depth-averaged turbulent intensity for a transverse profile

4.4. Hydrodynamics of the shear layer

The shallow mixing layer hydrodynamics were analyzed using transverse streamwise velocity profiles and turbulent intensity profiles to assess the evolution of the mixing layer, in terms of the transverse profiles shapes of the streamwise depth-averaged velocity and of the streamwise depth-averaged turbulent intensity. These profiles enable the analysis of the mixing layer in terms of the evolution of its width, its turbulent intensity, and its lateral shift towards the faster moving stream. Also, instantaneous velocity contour plots in spanwise direction were generated, which help to recognize how mixing occurs within the mixing layer from a three-dimensional perspective.

4.4.1. Transverse depth-averaged profiles across the mixing layer

The hydrodynamic behavior of the mixing layer can be observed by analyzing the transverse profiles of the depth-averaged streamwise velocity and turbulence intensity. The shape and magnitude of the values along the profiles allows for the identification of the mixing layer and its evolution in the downstream direction (within the experimental range of 0 to 30 cm).

4.4.1.1. Streamwise depth-averaged velocity profiles and flow deficit

The flow originates in the inlet reservoir of the flume which is divided by a splitter plate forming two parallel channels. The flow in each channel flows from the inlet reservoir over the transition curve into the channels for a distance of 175 cm down the channels, at which point the splitter plate ends and there is a confluence of the two streams. Transverse profiles of the depth-averaged streamwise velocity were determined from the trajectory segment velocities over the 10.5 s image sequence length at downstream distances of 1, 10, 20 and 29 cm from the end of the splitter plate/start of the merged stream, as shown in **Figure 4-13**. The profiles show, from left to right, the fast stream with an average velocity of approximately 0.45 m/s and the slow stream with an average velocity of approximately 0.31 m/s, which are separated by a velocity deficit/mixing layer. The velocity deficit is due to the development of a wake structure that forms from the development of boundary layers along each side of the splitter plate, which form one side wall for the flow in each of the two channels. The evolution of this wake structure into the classic mixing layer between the parallel coflowing streams is analyzed and discussed below.

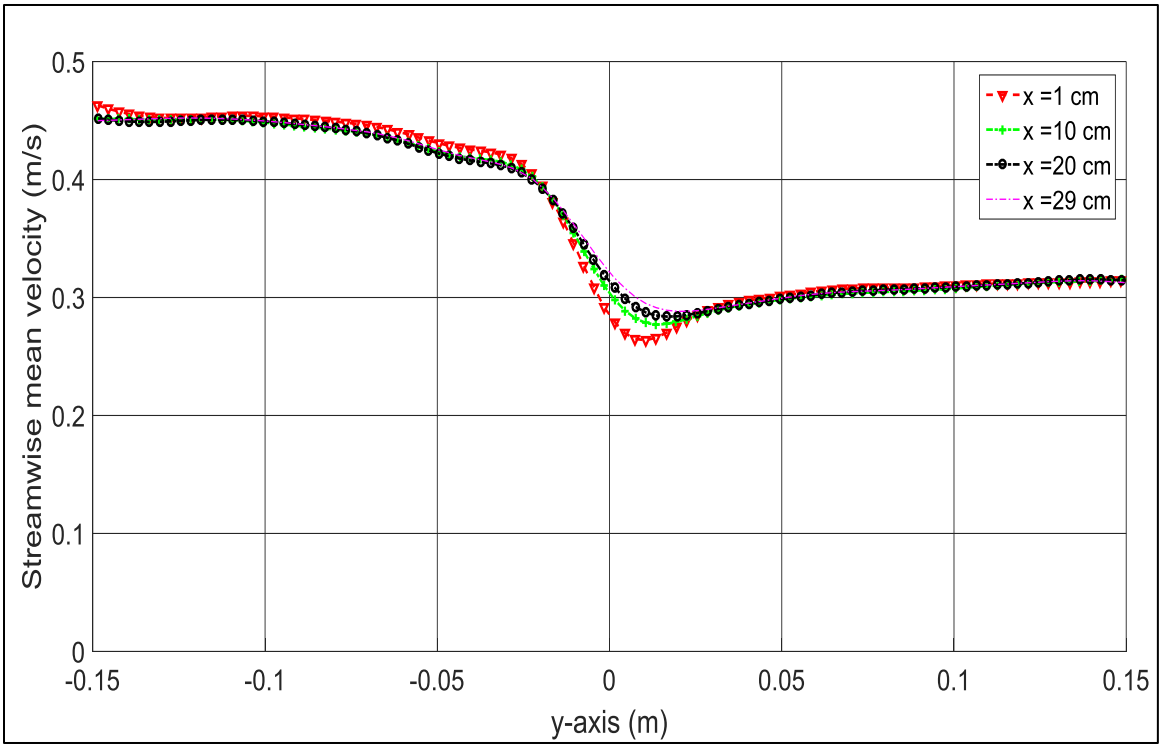

Figure 4-13. Mean streamwise (depth-averaged) velocity profiles
Left side fast stream and right side slow stream

A closer look at the central region of **Figure 4-13** (y = - 0.05 m to 0.05 m) helps to observe the flow deficit in greater detail, as shown in **Figure 4-14**. The magnitude of the velocity deficit decreases in the downstream direction, so that by x = 29 cm it has almost disappeared, and the flow profile is closer to that of a classic mixing layer.

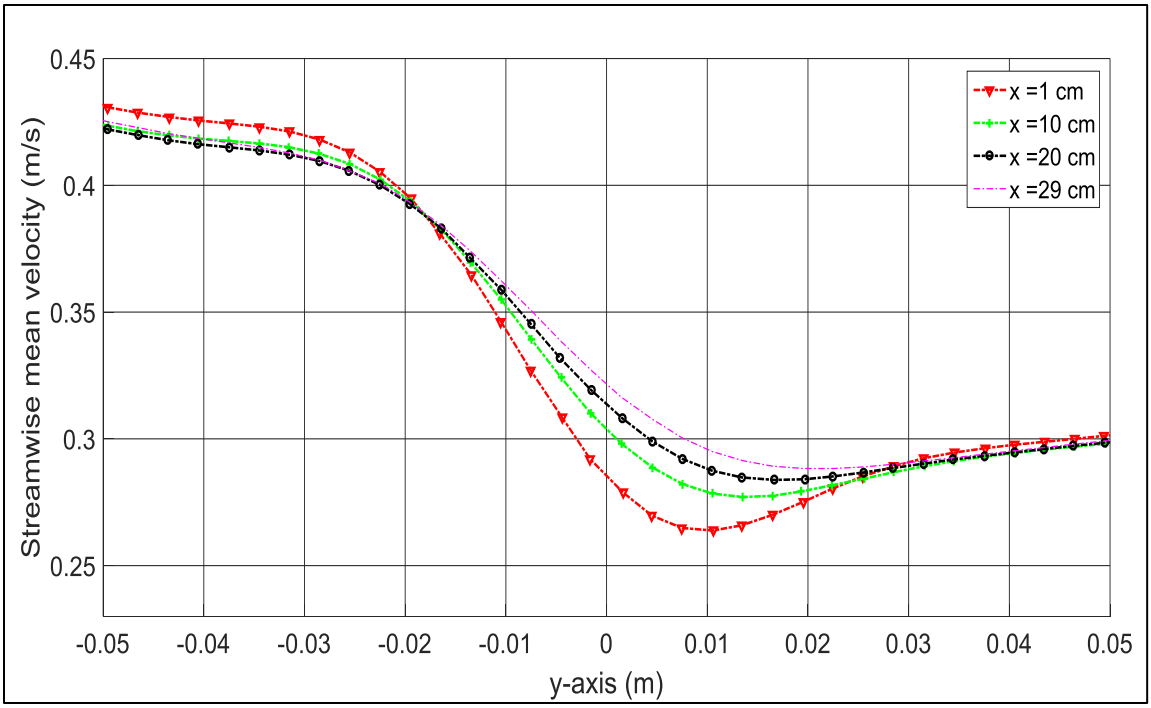

Figure 4-14. Zoom on the mean streamwise (depth-averaged) velocity profiles Left side fast stream and right side slow stream

When the flow enters the channel after the transition curve (see **Figure 3-1**), a boundary layer (Schlichting and Gersten 2000) develops not only at the bed but also on the side walls, one of which is the splitter plate wall. A boundary layer develops (increases in thickness), as momentum is lost due to drag, along the boundary, resulting in a layer of fluid with reduced velocity. The velocity deficit in the boundary layer follows a logarithmic profile from the boundary. The internal structure of the boundary layer arises due to the following: the fluid decelerated near the wall is periodically lifted away, in a sweeping motion of the eddy formed due to the high velocity gradient at the boundary, towards the outer layer of the boundary layer, while high-speed fluid rushes in to replace it (LI 2017). In the experiment, a boundary layer develops along each side of the splitter plate and these boundary layers meet at the end of the splitter plate at the streams confluence, resulting in a velocity deficit or wake structure. A schematic of the wake type flow due to the two boundary layers of similar magnitude meeting, having a logarithmic velocity profile, is shown in **Figure 4-15.**

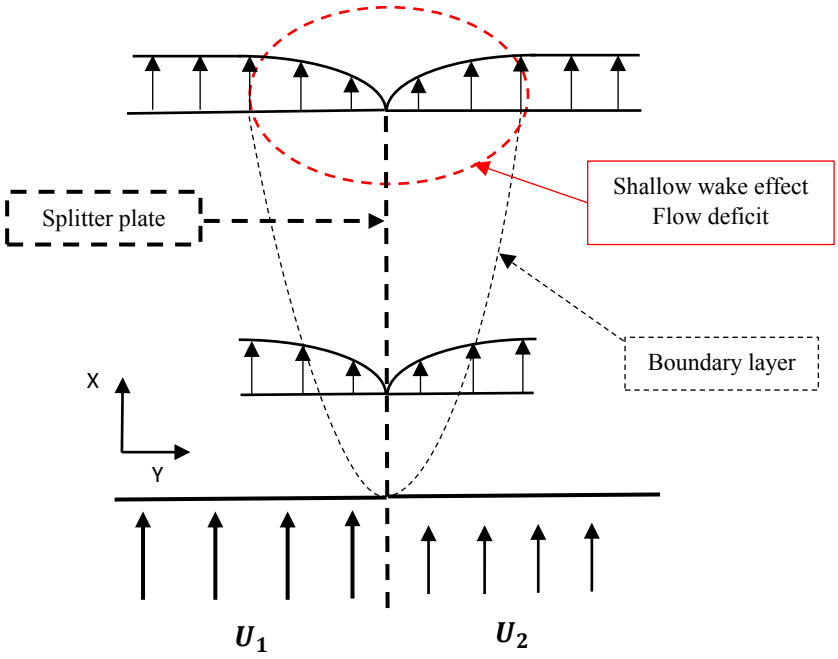

Figure 4-15. Schematic representation of boundary layers formation along the splitter plate

While studying confinement and bed friction effects on a shallow mixing layer in a similar laboratory setup of coflowing parallel streams, Chu and Babarutsi (1988) observed a flow deficit comparable to the one observed in **Figure 4-13** and **Figure 4-14**. The velocity deficit was observable up to 50 cm downstream of the confluence, beyond which the flow exhibited the characteristics of a pure shallow mixing layer. A similar investigation also studied a shallow mixing layer between coflowing parallel streams (Uijttewaal and Tukker 1998), and a wake feature was observed in the mean streamwise velocity profiles up to 45 cm downstream of the confluence. Numerical simulations of a river confluence have found the existence of a small stagnation zone at the confluence apex (Constantinescu, Miyawaki et al. 2011), as encountered in field studies (Rhoads and Sukhodolov 2001, Rhoads and Sukhodolov 2008), that resembles the flow deficit seen in **Figure 4-13** and **Figure 4-14**. As explained in Rhoads and Sukhodolov, 2001, this deficit is associated with a flow stagnation caused by the geometry of the confluence, defined as a wake effect near the flow junction.

Previous experimental studies for coflowing parallel streams have shown that the in-flow conditions and the confluence geometry play an important role in the flow dynamics, as claimed by Rhoads and Sukhodolov (2008). By comparing the study conducted by Chu and Babarutsi (1988) with those performed by Uijttewaal and Tukker (1998) and Uijttewaal and Booij (1999), the effect of the confluence and the boundary layers formed in the splitter plate can be further

explained. When the inlet section is shorter, and a flow contraction extends up to the end of the splitter plate, the initial growth rate of the shallow mixing layer width is larger as the flow is accelerated. Moreover, it has been shown that due to the boundary layers developing along both sides of the splitter plate, the origin of the shallow mixing layer or its virtual origin is displaced further downstream (by about 15 to 25 cm for the study conducted by Uijttewaal and Booij, 1999).

From the observations of the profiles in **Figure 4-13** and **Figure 4-14**, it is expected that the initial wake structure from the splitter evolves in the downstream direction into a pure shallow mixing layer as has been observed in previous experimental studies (Chu and Babarutsi 1988, Uijttewaal and Tukker 1998, Uijttewaal and Booij 2000). A schematic of the downstream evolution of the shear layer is presented in **Figure 4-16**, where it can be seen how the confluence initially results in a velocity deficit (like a wake velocity profile) that decreases in the streamwise direction until it has evolved into a shear layer with the velocity profile of a shallow mixing layer.

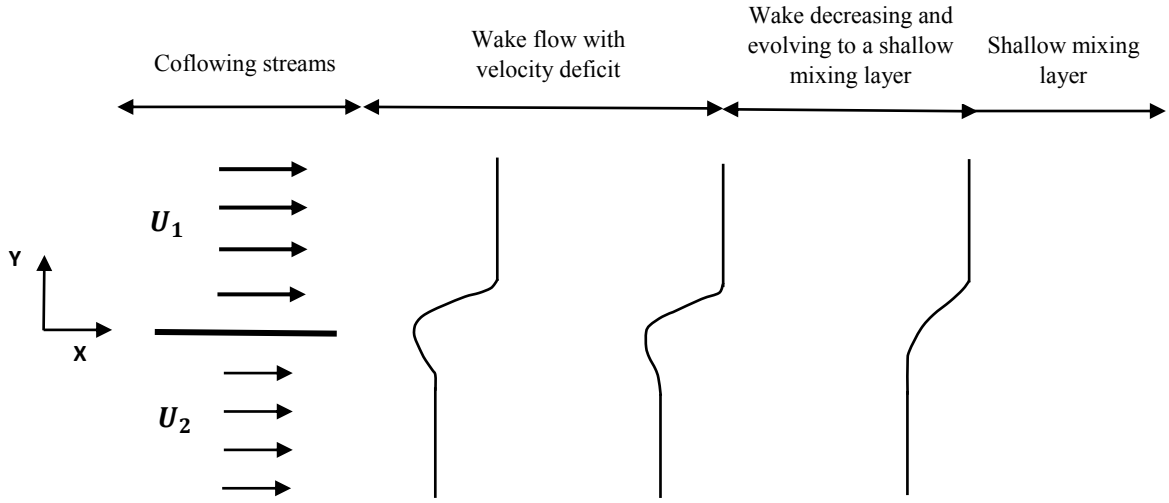

Figure 4-16. Schematic representation of the downstream evolution of the shear layer

Using equation [4], a theoretical profile of a shallow mixing layer can be calculated to compare it with the measured spanwise mean streamwise velocity profiles. From **Figure 4-17** it can be seen how, as the shear layer evolves with downstream distance, the flow deficit reduces, and it can be hypothesized that it will approach the classic profile of a pure shallow mixing layer at a point further downstream.

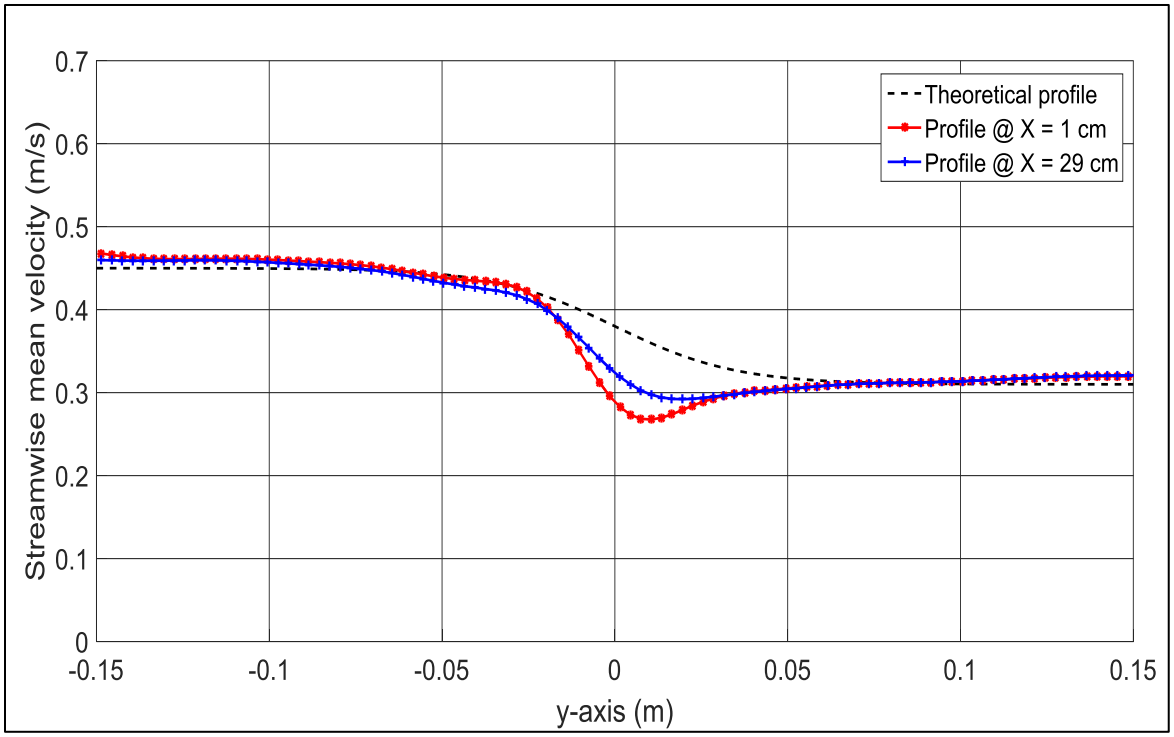

Figure 4-17. Velocity deficit comparison to a classic shear layer velocity profile

The estimation of the decrease in magnitude of the velocity deficit with downstream distance is shown in **Table 4-1**, and plotted in **Figure 4-18** (including the extrapolated data). The velocity deficit is calculated as the difference between the midpoint of the classic mixing layer profile, as given by equation [4] and plotted in **Figure 4-17**, and the minimum velocity of each profile. The reduction rate of the velocity deficit can be determined as 0.09 m/s-m. This data can be extrapolated to indicate that the velocity deficit should disappear approximately 90 cm after the confluence. The virtual origin of the pure shallow mixing layer can be determined once the width growth of the mixing layer from this point is known and can then be extrapolated in the upstream direction to the point of zero width of the mixing layer.

Table 4-1. Velocity deficit with downstream distance

Downstream distance (cm) *	Minimum velocity (cm/s) **	Velocity deficit (cm/s)
1	26.7	8.3
5	27.3	7.7
10	27.9	7.1
15	28.5	6.5
20	28.7	6.3
25	29.0	6.0

Table 4-1. Velocity deficit with downstream distance

Downstream distance (cm) *	Minimum velocity (cm/s) **	Velocity deficit (cm/s)
29	29.2	5.8

* Downstream distance measured from the end of the splitter.

** Minimum velocity value from the velocity profiles in **Figure 4-13**.

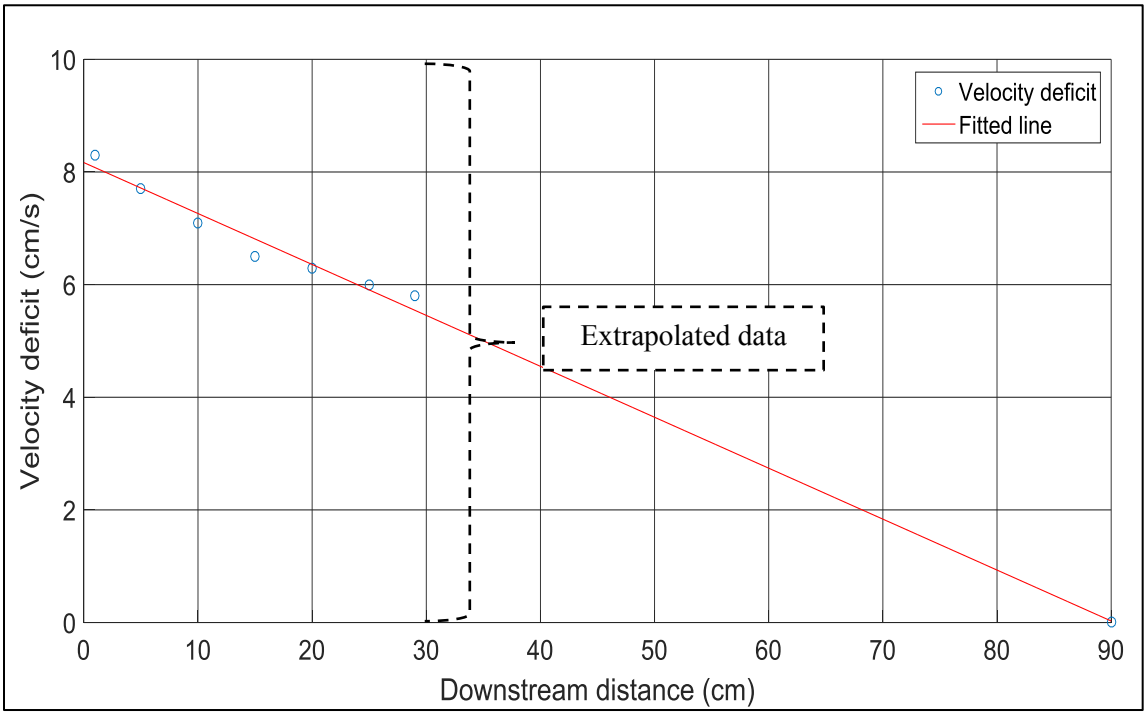

Figure 4-18. Decrease of velocity deficit with downstream distance

The central region of the mean depth-averaged streamwise velocity profiles (from y = -0.08 m to y = 0.08 m in spanwise direction) that were shown in **Figure 4-13**, are presented again in **Figure 4-19** as the average of the lower half of the flow (from z = 0 m to z = 0.0325 m) and the average of the upper half of the flow (from z = 0.0325 m to 0.065 m), to examine the effect of the bottom friction. It can be seen from **Figure 4-19** that the wake deficit is larger near the bottom, where the flow is being decelerated due to viscous effects. Also, it can be discerned that the flow deficit changes slightly more slowly for the bottom half of the mixing layer, whereas a faster reduction of the velocity deficit with downstream distance occurs for the top half of the flow.

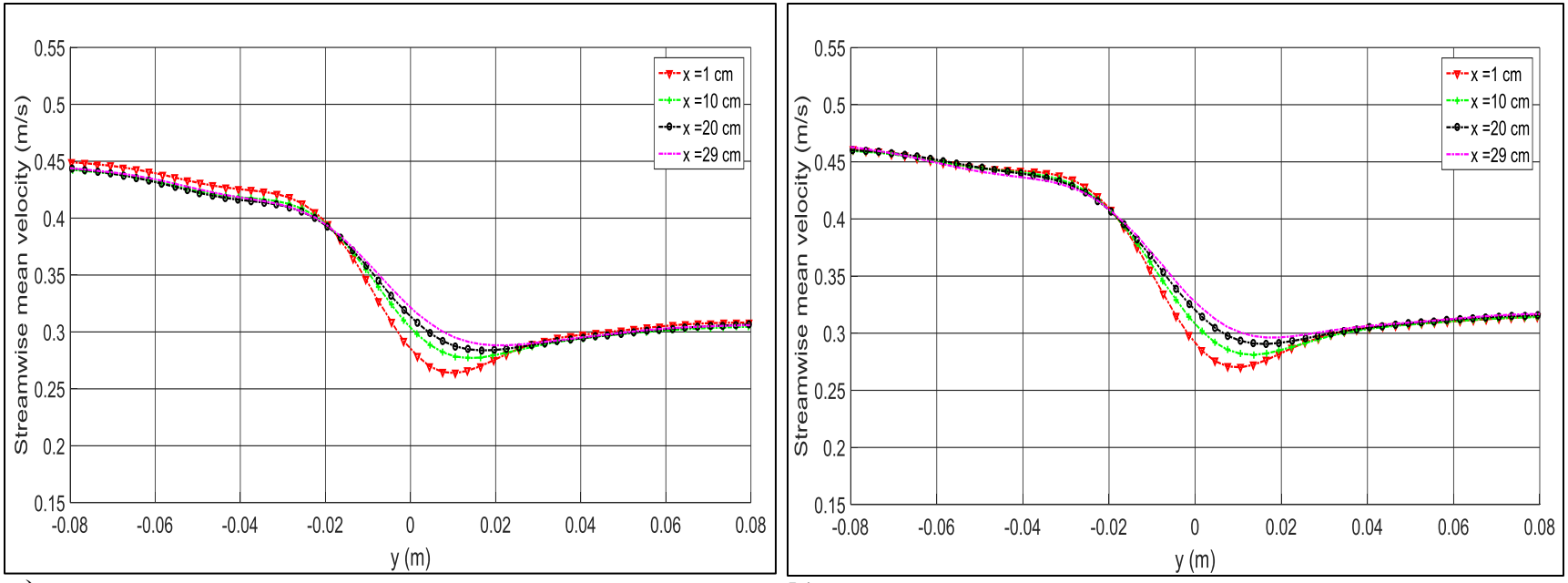

a) b)

Figure 4-19. Comparison of depth-averaged mean streamwise velocities profiles. a) Lower half of flow depth from 0 cm to 3.25 cm and b) Upper half of flow depth from 3.25 cm to 6.5 cm

4.4.1.2. Profiles of the depth-averaged turbulent intensity of the streamwise velocity

To further study and understand the flow hydrodynamics, transverse profiles of the depth-averaged turbulent intensity of the streamwise velocity are plotted in **Figure 4-20**, where the turbulent intensity ($\widetilde{u_\iota}$) is calculated as follows (Shen 2002),

$$\widetilde{u_\iota} = \sqrt{\frac{1}{N}\sum_{i=1}^{N}(u_i - \bar{u})^2} \qquad [21]$$

Where u_i is the velocity at a given time t, $\bar{u}$ is the time-averaged velocity and $i = 1,2,3$.

High levels of turbulent intensity are found in the shear layer between the two parallel flows with a maximum at the midpoint of the shear layer (velocity deficit/mixing layer) as shown in **Figure 4-20**. In addition, the turbulent intensity is slightly higher in the faster than the slower stream as expected as it is a function of the magnitude of the mean velocity. At y ~ 0 m the turbulent intensity is higher since the lateral velocity difference across the coflowing streams, due in part to the velocity deficit, causes lateral shearing, in addition to the contribution from the bottom friction (which is the level of turbulence in the two streams away from the midplane). Moreover, from **Figure 4-20** it can be observed that the center of the region of high turbulent intensity (the wake deficit which evolves into the mixing layer referred to as the shear layer) shifts towards the slow stream. Further information on the shifting of the shear layer center line is presented in section 4.4.2.

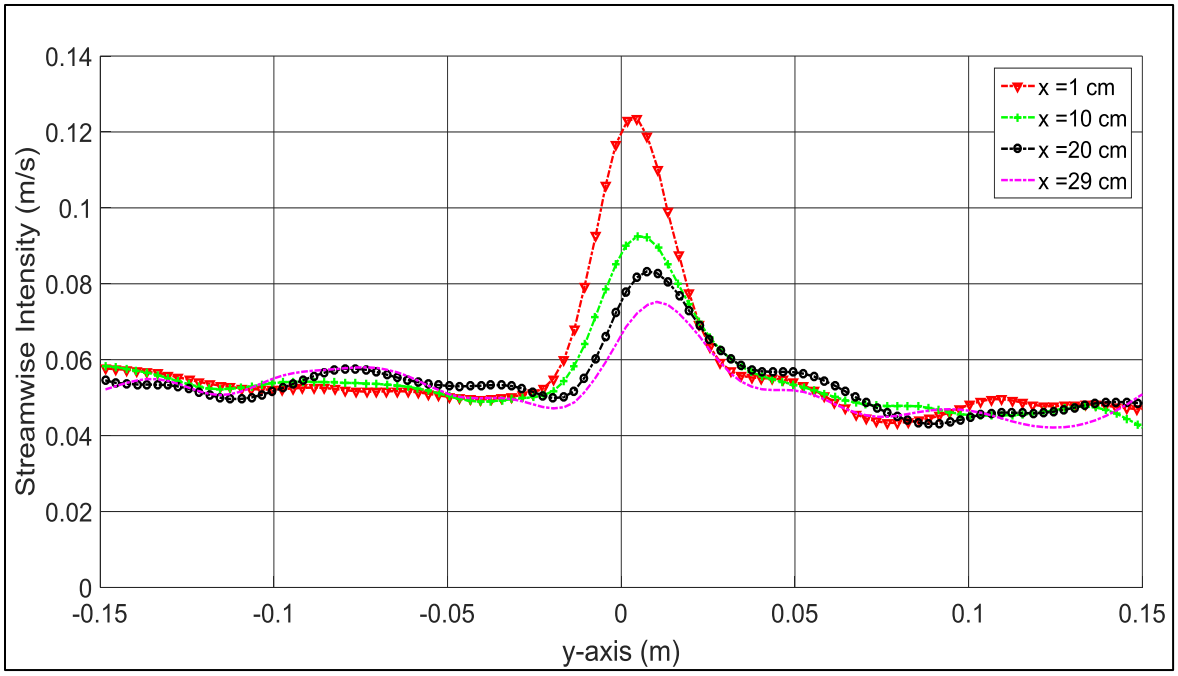

Figure 4-20. Mean streamwise turbulent intensity (depth-averaged)

Another characteristic of the mean flow shown in **Figure 4-13** is that as the shear layer evolves in the downstream direction, the effect of the bottom friction or drag effect acts on the streamwise velocities, removing energy from the flow and having an increasing cumulative effect as seen in the decreasing rate of change in the peak magnitude of turbulent intensity as shown in **Figure 4-20** to **Figure 4-22**. Although the wake region preceding the mixing layer has been identified in previous works (Chu and Babarutsi 1988, Uijttewaal and Booij 2000, Prooijen 2004, Sukhodolov, Schnauder et al. 2010), its behavior has not been characterized.

It is suggested that the decrease in the turbulent intensity of the shear layer in the downstream direction is due to the stabilizing effect of the bottom friction as the flow loses energy due to viscous effects as found and discussed in previous studies (Chu and Babarutsi 1988, Uijttewaal and Booij 2000, Prooijen 2004). Experimental data on a shallow wake, formed from a sudden expansion, shows that as the flow evolves with downstream distance its turbulent intensity is reduced due to the bottom friction stabilizing effect (Ganoulis, Babarutsi et al. 1989), similarly to that seen in **Figure 4-20**. The rate at which the flow losses energy to viscous effects is shown in **Figure 4-21**, in which the decay in turbulence intensity with downstream distance is plotted. These values can be compared to the levels of turbulence in the free-streams, which are also plotted in **Figure 4-21**.

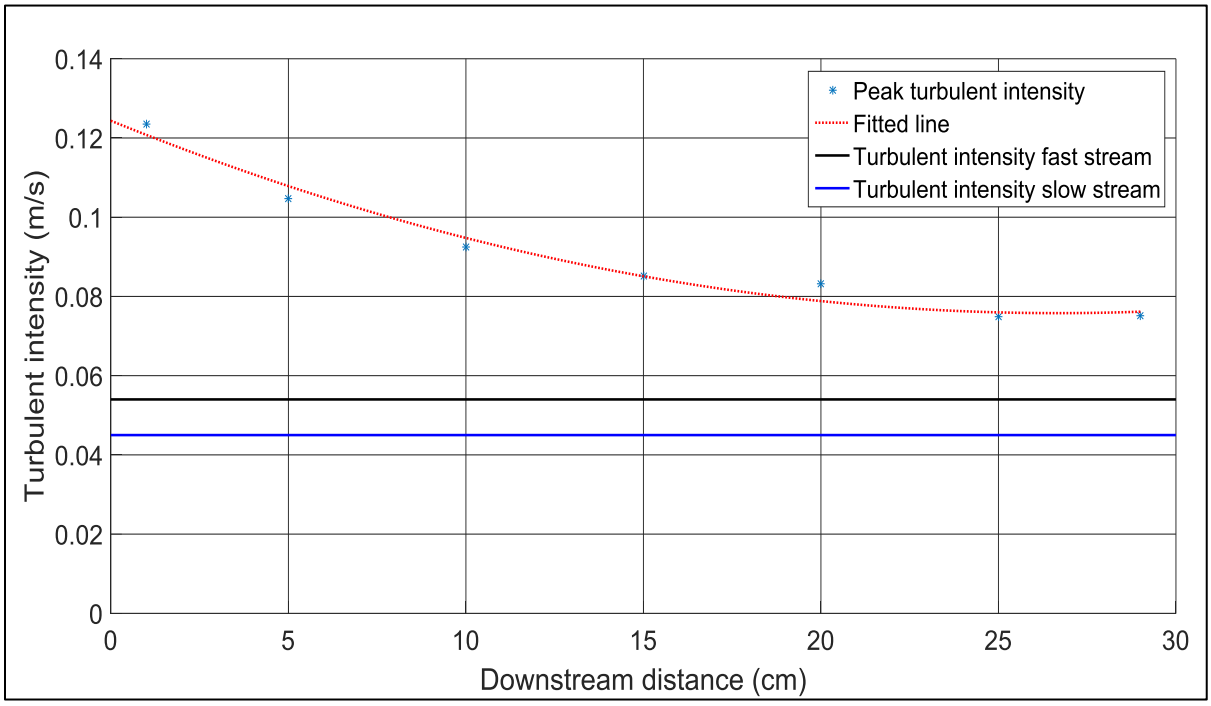

Figure 4-21. Downstream evolution of peak turbulence intensity

The variation with depth of the turbulent intensity in the central region of the flow (y = -0.08 m to y 0.08 m) is examined by comparing the turbulent intensity averaged over the bottom half of the water depth (z = 0 m to y 0.0.325 m) to that averaged over the top half of the water depth (z = 0.0325 to 0.065 m). From **Figure 4-22**, higher levels of turbulent intensity occur in the shear layer near the bed of the flume. This is due to the bottom friction causing vertical shearing adding to the lateral shearing. Also shown in **Figure 4-22**, there is a slightly greater decay (by 10%) of the peak turbulent intensity as viscous effects are more important near the flume bed causing higher flow deceleration.

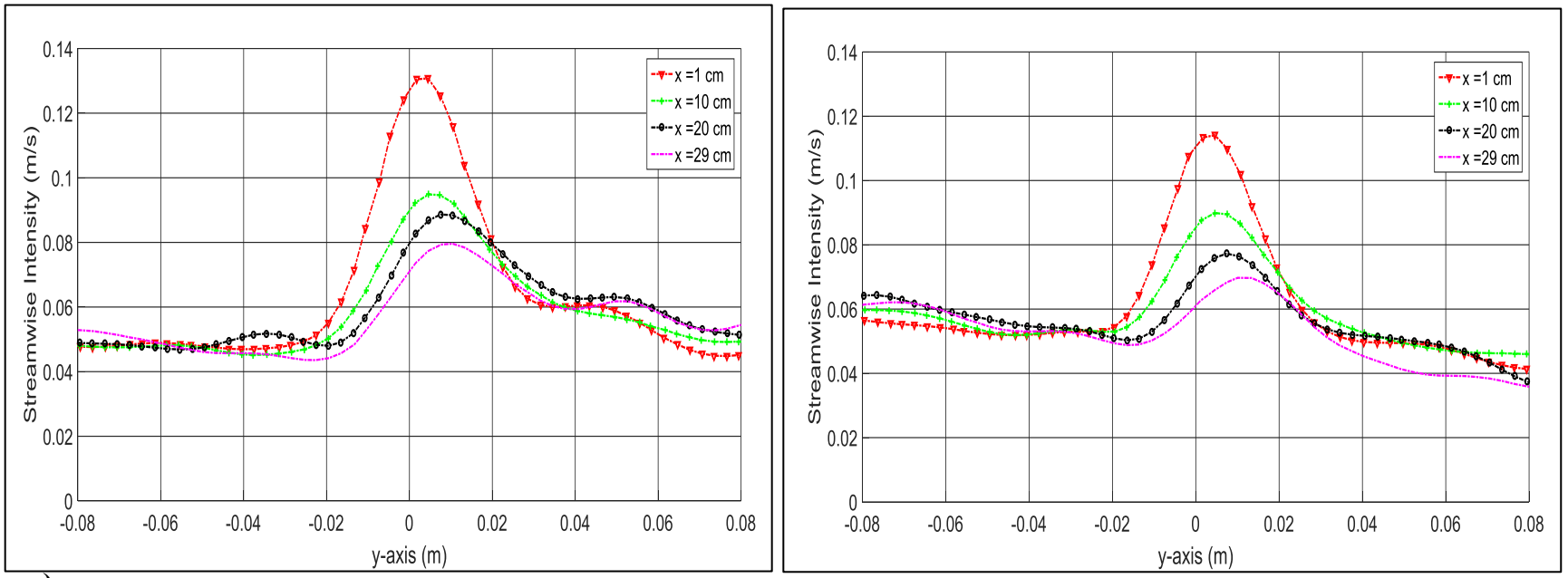

a) b)

Figure 4-22. Comparison of depth-averaged mean turbulent intensity profiles. a) Lower half of flow depth from 0 cm to 3.25 cm and b) Upper half of flow depth from 3.25 cm to 6.5 cm

4.4.2. Lateral shift of shear layer center

As mixing evolves with downstream distance, the midplane or center of the shear flow (lowest velocity value in each profile) is deflected towards the slow stream a tendency found for the mixing layer and discussed by Uijttewaal and Booij (2000). In **Figure 4-23** the displacement of the shear layer midplane, identified by finding the location of minimum velocity, is depicted at downstream distances of 1, 5, 10, 15, 20, 25 and 29 cm from the end of the splitter plate. This shift in the shear layer center, at a rate of approximately 0.030 mm/mm towards the slower moving stream, can be explained by the transfer of momentum. It has been proposed that this shift is in response to an asymmetrical momentum exchange across the mixing layer, in which the higher velocity region grows faster causing the mixing layer center to deflect toward the slower moving stream (Socolofsky and Jirka 2004). These observations on the mixing layer displacement are in good agreement with a field study where a high-velocity core in a river confluence shifts laterally toward the slow-flow side of the channel (Sukhodolov, Schnauder et al. 2010).

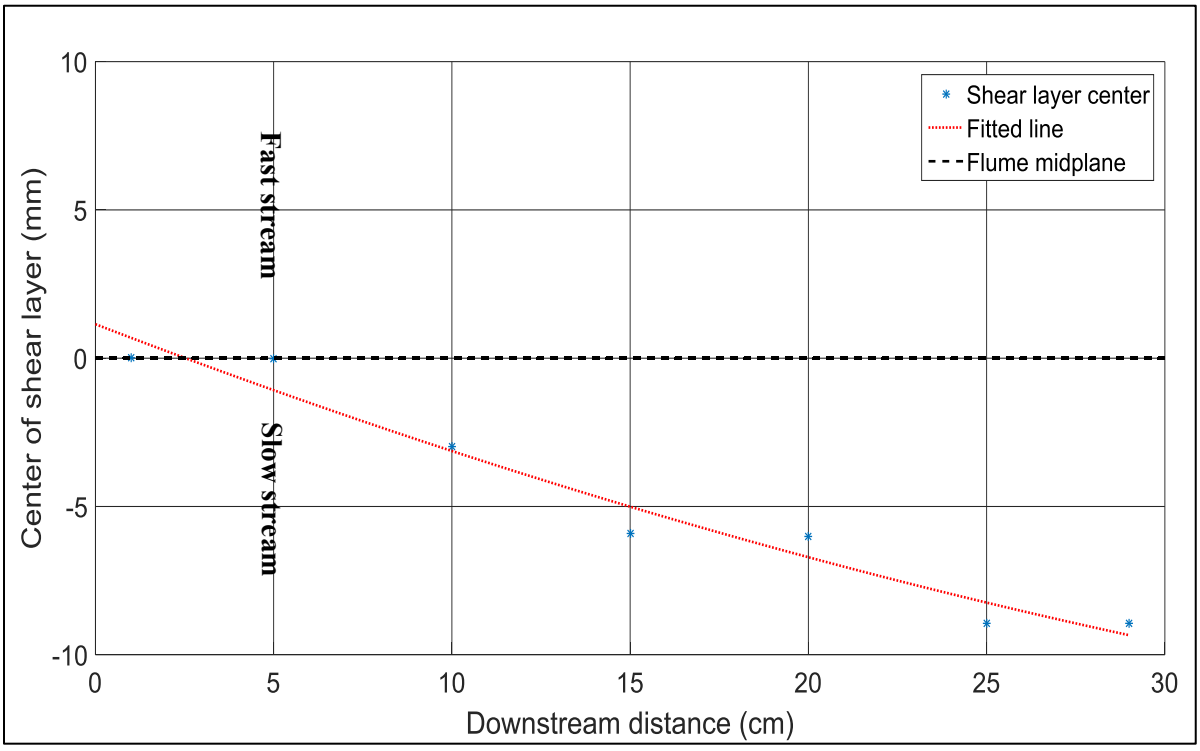

Figure 4-23. Lateral shift of the center of the shear layer

4.4.3. Downstream evolution of the shear layer width

Assuming a fully developed mixing layer, previous experimental studies (Chu and Babarutsi 1988, Uijttewaal and Booij 2000) have proposed estimating the mixing layer width

(from the geometry of the profile) as the ratio of the free-stream velocity difference to the maximum slope of the mixing layer profile using equation [2], $\delta = (U_1 - U_2) \,/\, (\partial u \,/\, \partial y)_{max}$, where U_i is the free-stream velocity in horizontal direction (outside the mixing layer width), $(\partial u \,/\, \partial y)_{max}$ is the maximum velocity gradient in spanwise direction, and $i = 1{,}2$ (see **Figure 4-24**). However, in the development region (just downstream of the splitter plate) where the effect of the boundary layers appearing along the splitter plate results in a velocity deficit in the transverse velocity profile shape, this equation will underestimate the velocity by more than a factor of 2 as shown in **Figure 4-24**. Equation [2] assumes a fully developed mixing layer, i.e. $x = {}^{y}/_{m}$ or in the context of this research $\delta = U_1 - U_2 \,/\, (\partial u \,/\, \partial y)max$, and therefore does not account for the velocity deficit in the near-field. For the current experimental conditions if the shear layer width (in which the velocity deficit is present) is calculated using equation [2], it would incorrectly determine that the width evolves with downstream distance in two stages: first a linear growth that expands until 5 cm after the splitter plate, and then the shear layer width approaches asymptotically the water depth of 6.5 cm, to attain a width of 6 cm after 30 cm downstream from the confluence.

As equation [2] underestimates the width of the shear layer in the development region just downstream of the splitter plate where the velocity deficit is present, a visual inspection of the transverse profile of the streamwise velocity as shown in **Figure 4-25** gives an estimate of the width of the shear layer. This width is calculated as the spanwise distance between the inflection points in the mean streamwise velocity profiles, where it can be observed that the width of the shear layer in fact remains constant at 5.5 cm for the first 30 cm in the streamwise direction (see **Figure 4-25**). The visual inspection approach to estimate the shear layer width would give a similar width in the fully developed mixing layer region as the definition of a shallow mixing layer width presented by Prooijen and Uijttewaal (2005) and plotted in **Figure 4-24** for the classic mixing layer profile.

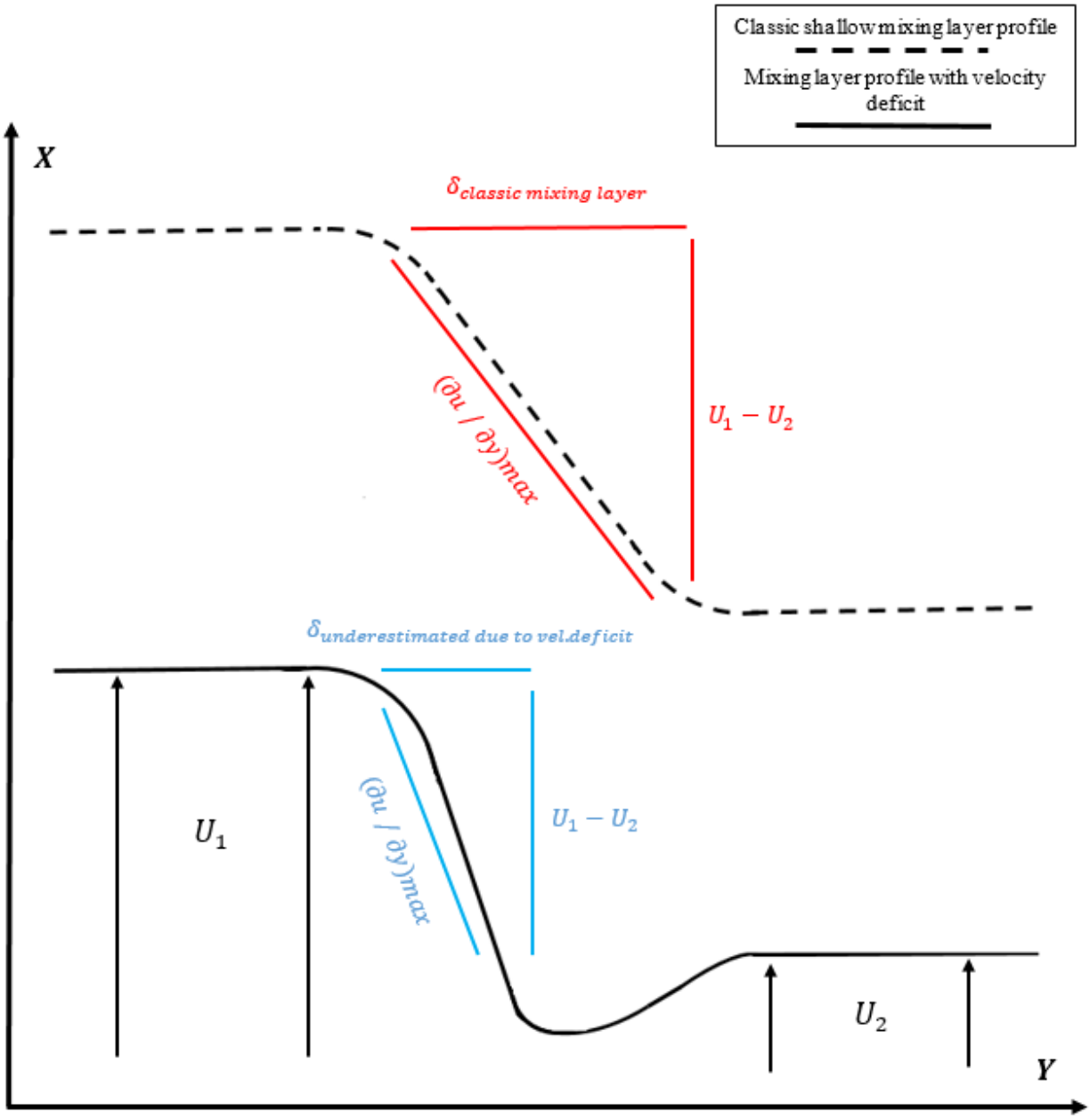

Figure 4-24. Definition of the mixing layer width and free-stream velocity with and without velocity deficit

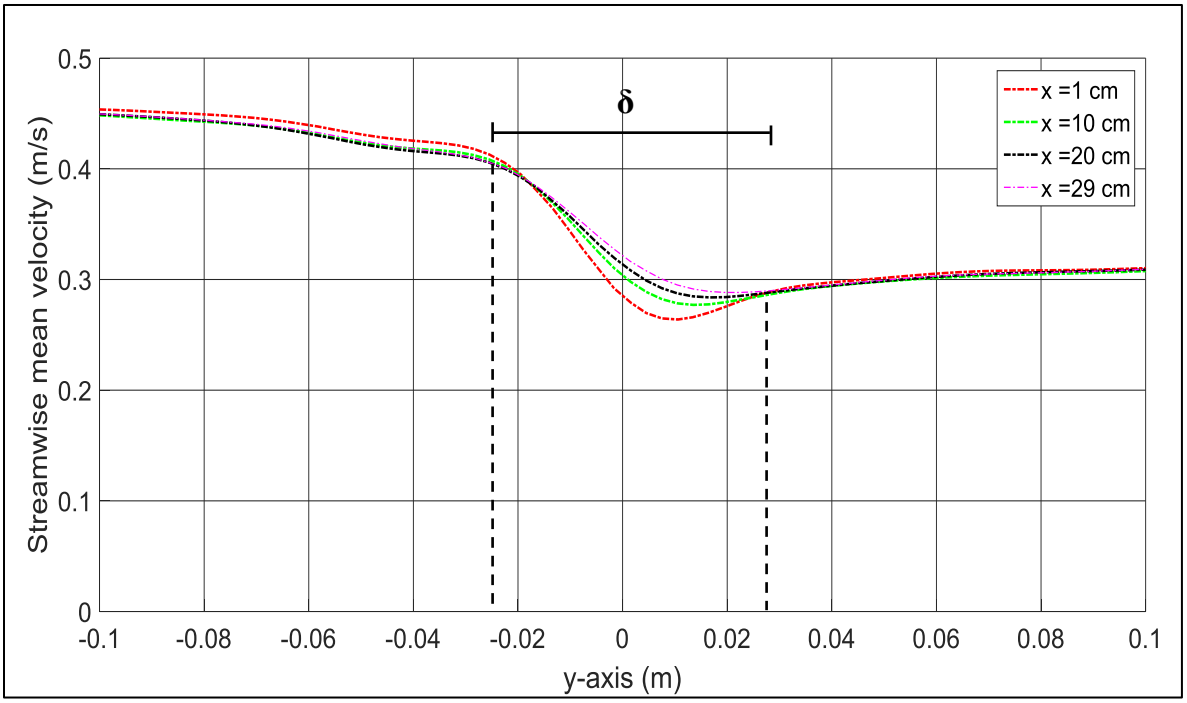

Figure 4-25. Proposed shear layer width estimated by visual inspection

4.4.4. Instantaneous velocity contour plots

The evolution of the mixing process with distance is examined using a contour plot of the flow front view (y-z plane) at different downstream positions. **Figure 4-26** depicts three instantaneous velocity contour plots in the vertical plane, at x = 0.03 m, 0.08 m, and 0.29 m. At the end of the splitter plate, at the point of confluence, there is little mixing and both currents flow side by side separated by a velocity deficit, which weakens with downstream distance. The velocity deficit observed in **Figure 4-26** reduces more quickly at the surface than at the bed, due to the bottom friction slowing down change near the bed. This could in turn result in a secondary flow forming and forcing mixing to occur at the top of the flow from the fast to the slow stream and at the bottom of the flow from slow to the fast stream. Note that a longer times series of the data is needed to confirm the secondary circulation, which cannot be collected using the current experimental setup.

The secondary circulation could be explained by a mechanism proposed by Uijttewaal and Booij (2000) in which a small lateral pressure gradient is present in the flow due to the slightly different water surface elevations in the two streams. This explanation agrees to that presented by Sukhodolov, Shnauder and Uijttewaal (2010), who claim that the presence of high pressure

gradients in a river flow cause the lateral fluxes of momentum and the formation of recirculating flows in spanwise direction.

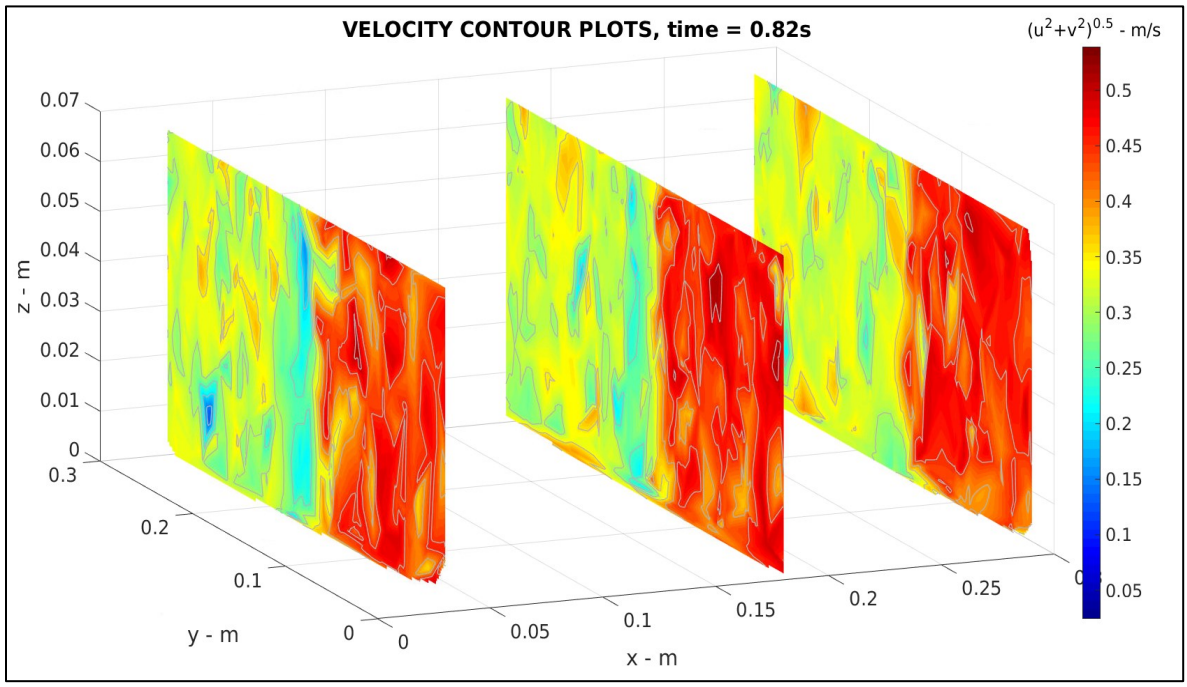

Figure 4-26. Instantaneous contour plot for $\sqrt{u^2 + v^2}$ in the y-z plane (front view)

5. CONCLUSIONS AND RECOMMENDATIONS

Shallow mixing layers are important as they can be found in different hydro-environments such as at the confluence of two rivers, at the interface of a main channel and a flood plain, and in groynes fields. They affect the lateral and longitudinal transport of mass (contaminants, nutrients, and sediments), and thus also the resistance of a river flow due to erosion or deposition on the bed and changes to the suspended load of a river and thus the river morphology. Understanding the hydrodynamics of a shallow mixing layer is required to better predict their effect on the behavior of shallow flows and the resulting pollutant/nutrient transport, sediment transport and erosion.

To gain a better understanding of a shallow mixing layer occurring in parallel coflowing streams, 3D Particle Tracking Velocimetry (3D-PTV) was chosen as an experimental method as it provides Lagrangian information on the flow hydrodynamics in three dimensions. 3D-PTV obtains Lagrangian data as trajectory segments of particles from a series of sequential images. This information can be analyzed to provide data in an Eulerian reference frame (by analysis of the trajectory data at specific locations) in addition to using the Lagrangian data to study coherent structures in the flow. This research is the initial stage of a study of shallow mixing layers using 3D-PTV, in which the flow behavior for the near-field (or developing region) at the confluence of two coflowing parallel streams is presented. The 3D-PTV data was analyzed to provide information on the velocity field in the zone of strong lateral shearing downstream of the confluence (near-field). Transverse profiles of depth-averaged streamwise velocity show a velocity deficit due the development of boundary layers along the splitter plate separating the two parallel flows. This results in a wake originating at the end of the splitter plate that decays with distance to the extent that it is small by the end of the measurement region at x = 30 cm. The velocity deficit results in a velocity gradient between the wake and the free-stream velocity of each stream causing lateral shearing and hence a zone of high turbulence in the midplane region of the channel flow between the two streams. The turbulent intensity of this shear layer decays with downstream distance as the wake structure decays and the flow loses energy due to viscous effects from the resistance at the bed. This zone of high turbulence shifts slightly from the fast-motion stream towards the slow-motion stream. The width of the shear layer (due to the wake and defined by the velocity deficit), defined as the region between the constant velocity regions of the two free-streams, remains constant in the developing region (observation range of 0 cm to 30 cm). Lastly,

the analysis of instantaneous velocity contour plots helps visualize the flow in three-dimensions, suggesting transverse mixing to occur at the top of the flow from the fast to the slow stream and at the bottom of the flow from the slow to the fast stream.

To date the study of shallow mixing layers has been from an Eulerian reference frame, and observations of the flow 2D coherent structures has used planar measurements. Using 3D-PTV provides an opportunity to further study, analyze, and expand the knowledge about shallow mixing layers in coflowing streams, by directly measuring the occurrence of 3D mixing processes in a Lagrangian reference frame. With the advantage of this new setup, the following aspects could be studied in the future: i) Extend the observation volume in the downstream direction to the end of the development region, which can be defined as the decay of the wake and the beginning of the classic mixing layer. ii) Study the wake decay in more detail using coflowing streams with the same velocity. iii) Investigate the evolution of coherent structures identified from the trajectory data (this requires an improvement in the data as the length of the trajectory segments observed will need to be longer). iv) Study the flow with different velocities (higher or lower levels of lateral shearing and turbulence) and different slopes, to quantify the effect of these relevant parameters on the hydrodynamic behavior of the shallow mixing layer. v) Expand the velocity measurements to obtain ADV data, and use it to validate the 3D-PTV results. vi) Finally, replicate previous experimental work in shallow mixing layers having different flow configurations, such as the interface of a main channel and a flood plain, and study them by applying 3D-PTV. This could reveal new findings as previous results were obtained mainly using planar and point measurement velocimetry techniques.

APPENDICES

Appendix A – Summary of ADV measurements for Q40% and Q50%

Table 5-1. Summary of ADV measurements Q40% ~ 25.5 L/s and Q50% ~ 32.5 L/s

FLOW RATES INFORMATION											
Pump capacity	Slow Stream (L/s)					Splitter plate	Fast Stream (L/s)				
40%	24.0 ± 0.1%						27.0 ± 0.1%				
50%	31.6 ± 0.1%						33.5 ± 0.1%				
ADV INFORMATION											
ADV	Vectrino from Nortek										
Sampling rate	25 Hz										
Sampling time	5 min										
Water depth	10 cm										
Sampling location	Tip of the splitter plate (see **Figure 3-1**)										
VELOCITY MEASUREMENTS FOR PUMP CAPACITY Q40% = 25.5 L/s											
Vert./Horiz. Position (cm)	-62.5	-50	-37.5	-25	-12.5	0	12.5	25	37.5	50	62.5
No Styrofoam nor honeycomb											
Streamwise velocity (m/s)											
6	0.3385	0.3378	0.3441	0.3393	0.3451		0.3719	0.3591	0.3685	0.36	0.3589
3	0.331	0.3247	0.3278	0.3255	0.3413		0.3675	0.3459	0.3552	0.3494	0.3558
AVERAGE	0.3355						0.3592				

Table 5-1. Summary of ADV measurements Q40% ~ 25.5 L/s and Q50% ~ 32.5 L/s

Standard deviation (cm/s)							
6	0.34		0.61				
3	0.67		0.82				
AVERAGE	0.51		0.72				
Use of Styrofoam							
Streamwise velocity (m/s)							
6			0.3723	0.3669	0.374	0.3687	0.3644
3			0.3687	0.3502	0.3595	0.3542	0.3586
AVERAGE			0.3638				
Standard deviation (cm/s)							
6			0.39				
3			0.69				
AVERAGE			0.54				
Use of Honeycomb							
Streamwise velocity (m/s)							
6			0.3715	0.3689	0.3715	0.3698	0.3575
3			0.3516	0.3446	0.3534	0.3476	0.3468
AVERAGE			0.3583				
Standard deviation (cm/s)							
6			0.59				
3			0.36				
AVERAGE			0.47				
Use of Styrofoam and honeycomb							
Streamwise velocity (m/s)							
6			0.3679	0.3803	0.3808	0.3811	0.3732

Table 5-1. Summary of ADV measurements Q40% ~ 25.5 L/s and Q50% ~ 32.5 L/s

3							0.3452	0.3548	0.36	0.3547	0.3503
AVERAGE							0.3648				
Standard deviation (cm/s)											
6							0.59				
3							0.56				
AVERAGE							0.57				
VELOCITY MEASUREMENTS FOR PUMP CAPACITY Q50% = 32.5 L/s											
Vert./Horiz. Position (cm)	-62.5	-50	-37.5	-25	-12.5	0	12.5	25	37.5	50	62.5
No Styrofoam nor honeycomb											
Streamwise velocity (m/s)											
6	0.4221	0.4187	0.4233	0.4182	0.4235		0.4524	0.4388	0.4539	0.4477	0.4446
3	0.4149	0.4039	0.4114	0.4079	0.4267		0.4561	0.4328	0.4399	0.4375	0.4400
AVERAGE	0.4171						0.4444				
Standard deviation (cm/s)											
6	0.25						0.61				
3	0.87						0.88				
AVERAGE	0.56						0.74				
Use of Styrofoam											
Streamwise velocity (m/s)											
6							0.4466	0.4421	0.4497	0.4426	0.441
3							0.446	0.4311	0.4368	0.434	0.4396
AVERAGE							0.4410				
Standard deviation (cm/s)											
6							0.36				

Table 5-1. Summary of ADV measurements Q40% ~ 25.5 L/s and Q50% ~ 32.5 L/s

3			0.57				
AVERAGE			0.47				
Use of Honeycomb							
Streamwise velocity (m/s)							
6			0.4618	0.4529	0.466	0.4536	0.4521
3			0.4471	0.4392	0.4459	0.4383	0.436
AVERAGE			0.4493				
Standard deviation (cm/s)							
6			0.62				
3			0.49				
AVERAGE			0.56				
Use of Styrofoam and honeycomb							
Streamwise velocity (m/s)							
6			0.4502	0.4531	0.4666	0.4634	0.4555
3			0.4276	0.4338	0.4441	0.4407	0.4334
AVERAGE			0.4468				
Standard deviation (cm/s)							
6			0.70				
3			0.65				
AVERAGE			0.67				

Appendix B – Transition Curve

The x and y coordinates of the transition curve are presented in **Table 5-2** and plotted in **Figure 5-1**. The transition curve location in the flume can be verified in **Figure 3-1**.

Table 5-2. Coordinates of transition curve

x coordinate (mm)	y coordinate (mm)
0	0
0	10
10	113
25	217
40	281
60	321
80	348
100	368
120	383
140	397
160	406
180	415
200	423
220	431
240	437
260	442
320	455
400	471
500	484
600	492
700	498
800	500

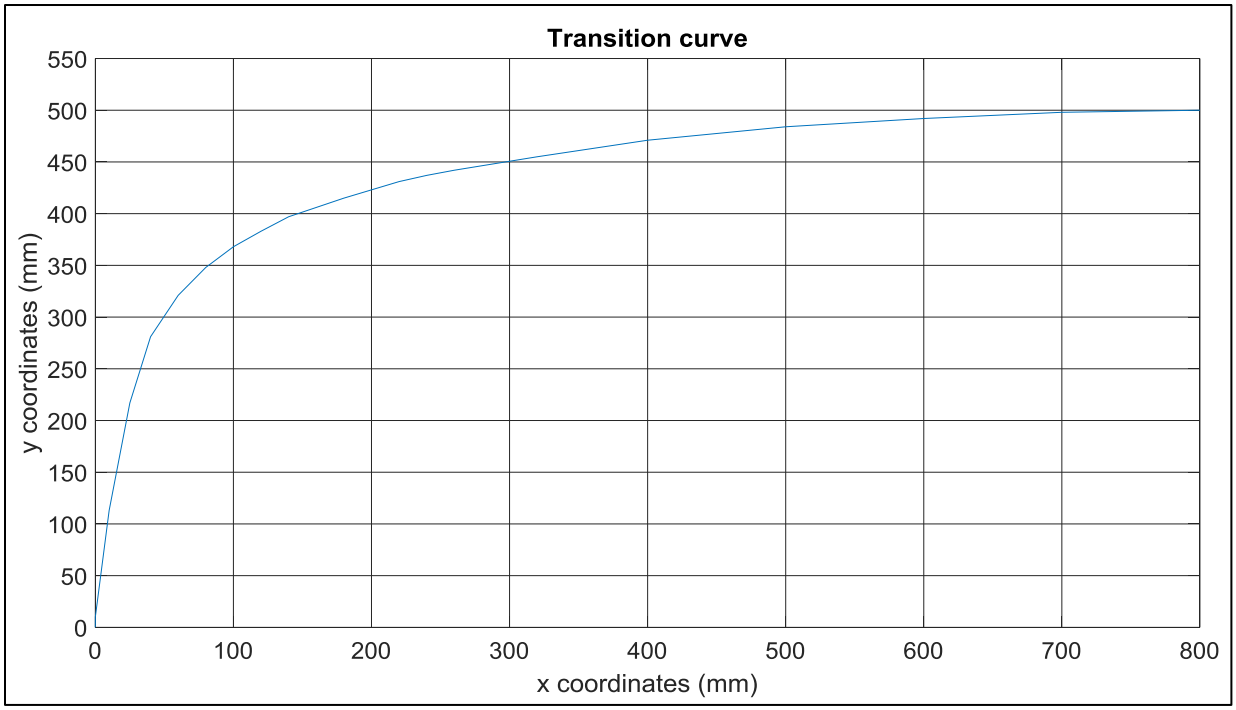

Figure 5-1. Transition curve

REFERENCES

Akutina, Y. (2016). Experimental investigation of flow structures in a shallow embayment using 3D-PTV. Doctor of Philosophy, McGill University.

Babarutsi, S. and V. H. Chu (1998). "Modeling Transverse Mixing Layer in Shallow Open-Channel Flows." Journal of Hydraulic Engineering **124**(7): 718-727.

Booij, R. and J. Tukker (2001). "Integral model of shallow mixing layers." Journal of Hydraulic Research **39**(2): 169-179.

Brown, G. L. and A. Roshko (2006). "On density effects and large structure in turbulent mixing layers." Journal of Fluid Mechanics **64**(4): 775-816.

Chu, V. H. and S. Babarutsi (1988). "Confinement and Bed Friction Effects in Shallow Turbulent Mixing Layers." Journal of Hydraulic Engineering **114**(10): 1257-1274.

Chu, V. H., F. Liu and W. Altai (2004). "Friction and confinement effects on a shallow recirculating flow." Journal of Environmental Engineering and Science **3**(5): 463-475.

Consortium, O. Original Manual**:** 12.

Consortium, O. (2014). "OpenPTV - Open Source Particle Tracking Velocimetry." Retrieved September, 2016, from http://www.openptv.net/.

Consortium, O. (2015 09/04/17). "3DPTV-Post-Process." Retrieved 01/01/17, 2017, from https://github.com/3dptv/3d-ptv-post-process.

Constantinescu, G., S. Miyawaki, B. Rhoads, A. Sukhodolov and G. Kirkil (2011). "Structure of turbulent flow at a river confluence with momentum and velocity ratios close to 1: Insight provided by an eddy-resolving numerical simulation." WRCR Water Resources Research **47**(5): 1 - 16.

Daoyi, C. and G. H. Jirka (1998). "Linear stability analysis of turbulent mixing layers and jets in shallow water layers." Journal of Hydraulic Research **36**(5): 815-830.

Dracos, T. A. (1996). "Three-dimensional velocity and vorticity measuring and image analysis techniques : lecture notes from the short course held in Zurich, Switzerland, 3-6 September 1996."

Drazin, P. G. and W. H. Reid (2004). Hydrodynamic stability. Norwood Mass.

Ganoulis, J., S. Babarutsi and V. H. Chu (1989). "Experimental Investigation of Shallow Recirculating Flows." Journal of Hydraulic Engineering **115**(7): 906-924.

Gaudet, J. M. and A. G. Roy (1995). "Effect of bed morphology on flow mixing length at river confluences." Nature **373**(6510): 138-139.

IfU, E. Z.-D.-B.-. (2016, April 24, 2013). "Particle Tracking Velocimetry Software." Retrieved September, 2016, from https://www1.ethz.ch/ifu/publications/software/ptv/index_EN.

Jirka, G. H. (2001). "Large scale flow structures and mixing processes in shallow flows." Journal of Hydraulic Research **39**(6): 567-573.

Jirka, G. H. and W. S. Uijttewaal (2004). "Shallow flows: a definition." Shallow flows: 3-11.

Khorsandi, B., L. Mydlarski and S. Gaskin (2012). "Noise in Turbulence Measurements Using Acoustic Doppler Velocimetry." Journal of Hydraulic Engineering **138**(10): 829-838.

Kim, J. T. (2015). Three-dimensional particle tracking velocimetry for turbulence applications, University of Illinois Urbana-Champaign.

Klebanoff, P. S., K. D. Tidstrom and L. M. Sargent (1962). "The three-dimensional nature of boundary-layer instability." Journal of Fluid Mechanics **12**(01).

LI, D. J. (2017). "3A1 Incompressible Flow - Boundary Layer Theory." Retrieved 20/07/17, 2017 from http://www3.eng.cam.ac.uk/~jl305/.

Liggett, J. A. (1994). Fluid mechanics. New York, McGraw-Hill.

Lohrmann, A., R. Cabrera and N. C. Kraus (1994). Acoustic-doppler velocimeter (ADV) for laboratory use. Proceedings of the Symposium on Fundamentals and Advancements in Hydraulic Measurements and Experimentation, August 1, 1994 - August 5, 1994, Buffalo, NY, USA, Publ by ASCE.

Lüthi, B. (2002). Some aspects of strain, vorticity, and material element dynamics as measured with 3D particle tracking velocimetry in a turbulent flow. Doctor of Technical Sciences, Swiss Federal Institute of Technology Zurich.

Luthi, B., A. Tsinober and W. Kinzelbach (2005). "Lagrangian measurement of vorticity dynamics in turbulent flow." Journal of Fluid Mechanics **528**(1): 87-118.

Maas, H. G., A. Gruen and D. Papantoniou (1993). "Particle tracking velocimetry in three-dimensional flows." Experiments in Fluids **15**(2): 133-146.

Malik, N. A., T. Dracos and D. A. Papantoniou (1993). "Particle tracking velocimetry in three-dimensional flows." Experiments in Fluids **15**(4): 279-294.

Mollo-Christensen, E., A. Pesetsky, A. Morochink, M. Chalufour, C. Education Development, F. National Committee for Fluid Mechanics and C. Encyclopaedia Britannica Educational "Flow instabilities."

Moody, J. A. (1995). Observations of Mixing Processes Downstream from the Confluence of the Mississippi and St. Croix Rivers. Double-Diffusive Convection, American Geophysical Union**:** 275-286.

Nikora, V., R. Nokes, W. Veale, M. Davidson and G. H. Jirka (2007). "Large-scale turbulent structure of uniform shallow free-surface flows." Environmental Fluid Mechanics **7**(2): 159-172.

Prooijen, B. v. (2004). Shallow Mixing Layers. Doctoral thesis, TU Delft.

Raffel, M. (2007). Particle image velocimetry : a practical guide. Heidelberg; New York, Springer.

Rhoads, B. L. and A. N. Sukhodolov (2001). "Field investigation of three-dimensional flow structure at stream confluences: 1. Thermal mixing and time-averaged velocities." WRCR Water Resources Research **37**(9): 2393-2410.

Rhoads, B. L. and A. N. Sukhodolov (2008). "Lateral momentum flux and the spatial evolution of flow within a confluence mixing interface." Water Resources Research **44**(8): n/a-n/a.

Schlichting, H. and K. Gersten (2000). Boundary-layer theory. Berlin; New York, Springer.

Shen, H. H. (2002). Environmental fluid mechanics : theories and applications. Reston, Va., American Society of Civil Engineers.

Socolofsky, S. A. and G. H. Jirka (2004). "Large-scale flow structures and stability in shallow flows." Journal of Environmental Engineering and Science **3**(5): 451-462.

Sukhodolov, A. N., I. Schnauder and W. S. J. Uijttewaal (2010). "Dynamics of shallow lateral shear layers: Experimental study in a river with a sandy bed." WRCR Water Resources Research **46**(11): 1 - 18.

Talstra, H., W. S. Uijttewaal and G. S. Stelling (2006). Emergence of large-scale coherent structures in a shallow separating flow. Proc. Int. Conf. Fluvial Hydraulics (River Flow), Taylor and Francis, UK.

Tennekes, H. and J. L. Lumley (1972). A first course in turbulence. Cambridge, Mass., MIT Press.
Uijttewaal, W. (2009). "Coherent Flow Structures in Shallow Mixing Layers." ERCOFTAC Bulletin March 2009 78: 54.

Uijttewaal, W. and R. Booij (2000). "Effects of shallowness on the development of free-surface mixing layers." Physics of Fluids (1994-present) **12**(2): 392-402.

Uijttewaal, W. S. J. (2014). "Hydrodynamics of shallow flows: application to rivers." Journal of Hydraulic Research **52**(2): 157-172.

Uijttewaal, W. S. J. and R. Booij (1999). Influence of shallowness on growth and structures of a mixing layer A2 - Rodi, W. Engineering Turbulence Modelling and Experiments 4. D. Laurence. Oxford, Elsevier Science Ltd**:** 415-422.

Uijttewaal, W. S. J. and J. Tukker (1998). "Development of quasi two-dimensional structures in a shallow free-surface mixing layer." Experiments in Fluids: Experimental Methods and their Applications to Fluid Flow **24**(3): 192-200.

van Prooijen, B., R. Booij and W. Uijttewaal (2000). Measurement and analysis methods of large scale horizontal coherent structures in a wide shallow channel. 10th international symposium on applications of laser techniques to fluid mechanics. Calouste Gulbenkian Foundation, Lisbon.

van Prooijen, B., M. De Nijs and W. S. J. Uijttewaal (2004). Perturbing the inflow condition in shallow mixing layer experiments. Shallow Flows, Taylor & Francis**:** 95-102.

van Prooijen, B. C. and W. S. J. Uijttewaal (2002). "A linear approach for the evolution of coherent structures in shallow mixing layers." Physics of Fluids **14**(12): 4105.

van Prooijen, B. C. and W. S. J. Uijttewaal (2005). Horizontal Mixing in Shallow Flows. Water Quality Hazards and Dispersion of Pollutants. W. Czernuszenko and P. M. Rowiński. Boston, MA, Springer US**:** 55-68.

Virant, M. and T. Dracos (1997). "3D PTV and its application on Lagrangian motion." Measurement Science and Technology **8**(12): 1539-1552.

Weitbrecht, V., G. Kühn and G. H. Jirka (2002). "Large scale PIV-measurements at the surface of shallow water flows." Journal Flow Measurement and Instrumentation **13**(5): 237-245.